An evaluation of the use of high-resolution RGB and multispectral imaging as a potential tool for drill-core logging of the rocks of the Bushveld Complex.

by

Nomonde Shantel Tshiwela Mabogo

24/10/2025

Submitted in fulfilment of the requirements in respect of the Master of Science degree in the Department of Geology

Faculty of Natural and Agricultural Sciences at the

University of the Free State.

Supervisor: Prof. Frederick Roelofse

Co-supervisor: Dr. Martin Clark

Department of Geology, University of the Free State

DECLARATION

Master's Student

I, Nomonde Shantel Tshiwela Mabogo declare that the master's degree research dissertation or interrelated, publishable manuscripts/published articles, or coursework master's degree mini dissertation that I herewith submit for the master's degree qualification in Geology at the University of the Free State is my independent work, and that I have not previously submitted it for a qualification at another institution of higher education",

Student's Signature

24/10/2025

Date

Geology Department

Name of Department

ABSTRACT

Core recovery drilling remains a fundamental component of mineral exploration in the Bushveld Complex of South Africa, which hosts the world's largest platinum-group element reserves within the world's largest layered intrusion, the mafic to ultramafic Rustenburg Layered Suite. Manual logging of extensive drill-core intervals is time-consuming and inherently subjective, often limiting the precision of lithological and mineralogical interpretations. This study assesses spectroscopic drill-core logging techniques, such as RGB-to-grayscale and visible to near-infrared (VNIR) multispectral imaging (400-842 nm), applied to the Rustenburg Layered Suite drill-core as potential tools for cost-effective drill-core logging of the major lithologies and minerals of the Rustenburg Layered Suite.

High-resolution RGB images were converted to grayscale using the luminosity method, and grayscale digital number (0-255) statistics, median and skewness were analysed for lithological classification. The grayscale approach distinguishes chromitite and anorthosite through contrasting histogram skewness, with median-based validation correctly classifying 3% of anorthosite samples and 0% of chromitite, the latter is due to limited representation in the training dataset and that training and validation chromitite samples differ in the proportion of dark and lighter crystals. In contrast, gabbronorite and pyroxenite proved more challenging to differentiate, reflecting their broad compositional ranges and overlapping plagioclase-pyroxene assemblages, with 19% gabbronorite validation sites and 44% pyroxenite validation sites being either a gabbronorite or pyroxenite. Additionally, the weighting of the green channel in the luminosity-based grayscale conversion can shift darker pixels toward higher grayscale values, potentially leading to the misclassification of dark lithologies as lighter-coloured lithologies. Thus, this approach proved less effective for reliable lithological classification across the dataset.

VNIR multispectral imaging (475-842 nm) enables classification of major minerals such as pyroxene, plagioclase, and chromite, with spectral library correlations improving accuracy by identifying minerals prone to misclassification. The results show that 40% of pyroxenite samples contained over 90% pyroxene, 12% of anorthosite samples contained over 90% plagioclase, 71-75% of gabbronorite samples exhibited mixed plagioclase-pyroxene proportions within the 10-90% compositional range, and all chromitite samples contained more than 45% chromite. Results also reflect expected mineralogical trends, with mafic rocks showing higher mafic mineral content and anorthositic rocks dominated by felsic minerals.

Consequently, VNIR multispectral imaging may emerge as a cost-effective and time-efficient assistive tool to traditional manual logging for the Rustenburg Layered Suite lithologies, especially in large-scale exploration programs involving the drilling of thousands of metres of drill-core, and when integrated with automated analytical workflows. Therefore, the applicability of these imaging techniques in mining operations is influenced by project scale and operational priorities.

Keywords: Multispectral imaging, spectroscopy, mineral classification, Bushveld Complex, drill-core logging

ACKNOWLEDGEMENTS

I would like to thank the Mandela Mining Precinct and its stakeholders for funding this project under the SAMERDI Research Centre and for providing learning opportunities to support this project.

I would like to thank my fellow students and project leader, Prof. John Carranza under the SAMERDI Research Centre, for their support and guidance in various subject matters of geology. A special thanks to Miss Martha Amwaama under the SAMERDI Research Centre for accompanying and driving me to the core shed and assisting with sample preparation. This project involved me with the MAGIC Lab under the Geology Department, and the team contributed to various aspects of this project, such as guidance on software and techniques used and words of encouragement during this journey.

The results of the analysis of the drill-core were conducted in the Geology Department at the University of the Free State. Many thanks to Dr. Megan Purchase and Mr. Johannes Malebati for assisting me with the analysis and taking the time to explain the analytical techniques in this project. I believe almost everyone in the Geology Department contributed to the completion of this project through words of encouragement and guidance in other aspects of life.

A special thanks to my supervisors, Prof. Frederick Roelofse and Dr. Martin Clark, for their constant support. I deeply value the guidance and knowledge they have imparted to me. Their endless support from working in the core shed together, through consultations and meetings, sparked ideas and a better understanding of concepts. I appreciate the valuable questions, discussions, and feedback received through corridor interactions and other forms of communication during the completion of this work.

Finally, thanks to the Almighty God for life and health, my family, relatives, and friends for their continuous support and patience during this journey.

TABLE OF CONTENTS

LIST OF TABLES

LIST OF FIGURES

LIST OF ABBREVIATIONS

An: Anorthite

ASTER: Advanced Spaceborne Thermal Emission and Reflection Radiometer

BC: Bushveld Complex

BH: Borehole

Chr: Chromite

CIPW: Cross, Iddings, Pirsson, Washington

CPX: Clinopyroxene

CRP: Calibrated Reflectance Panel

CZ: Critical Zone

DN: Digital Number

En: Enstatite

ENVI: Environment for Visualising Images

GMA: Giant Mottled Anorthosite

IUGS: International Union of Geological Sciences

LCZ: Lower Critical Zone

LG 1-7: Lower Group 1-7

LIBS: Laser-Induced Breakdown Spectroscopy

LWIR: Longwave- Infrared

LZ: Lower Zone

MF: Matched Filtering

MG 1-4: Middle Group 1-4

MG: Middle Group

MNF: Minimum Noise Fraction

MP: Megapixels

MR: Merensky Reef

MTMF: Mixture Tuned Matched Filtering

MZ: Main Zone

NIR: Near-infrared

nm: nanometer

Ol: Olivine

OPX: Orthopyroxene

Or: Orthoclase

PCA: Principal Component Analysis

PGE: Platinum Group Elements

PLAG: Plagioclase

PPI: Pure Pixel Index

ppm: parts per million

Px: Pyroxene

QAPF: Quartz-Alkali Feldspar-Plagioclase-Feldspathoids

QTZ: Quartz

RE: Red-Edge

RGB: Red, Green, Blue

RLS: Rustenburg Layered Suite

ROI: Region of Interest

SAM: Spectral Angle Mapper

SD: Standard Deviation

SEM: Scanning Electron Microscopy

SHW: Spectral Hourglass Workflow

Sr: Strontium

SWIR: Shortwave-Infrared

TIR: Thermal Infrared

UCZ: Upper Critical Zone

UG 1-2: Upper Group 1-2

USGS: United States Geological Survey

UZ: Upper Zone

VNIR: Visible to Near-Infrared

XRD: X-Ray Diffraction

XRF: X-Ray Fluorescence Spectrometry

1 Introduction

The Paleoproterozoic (~2.06 Ga) Bushveld Complex (BC) intruded into the Transvaal Supergroup of northeast South Africa (Charlier and Zellmer, 2000; Coertze *et al.*, 1978; Scoates *et al.*, 2021; Walraven *et al.*, 1990). The BC is host to the world's largest resource of platinum group elements (PGEs), of which South Africa historically produced ~75% of the global output (Barnes and Maier, 2002). The PGEs occur within the layered mafic to ultramafic Rustenburg Layered Suite (RLS) of the BC, which is exposed at the surface in 4 geographically defined "limbs", which are, the Northern Limb, Eastern Limb, Western Limb, and the Far Western Limb (Roelofse and Ashwal, 2012). The Western and Eastern limbs are about 7-9 km thick and stratigraphically similar, whereas the Northern Limb is thinner (between 3-5 km) (Barnes and Maier, 2002; Eales and Cawthorn, 1996). The Lebowa Granite Suite and the Rashoop Granophyre Suite collectively constitute the BC along with the RLS.

For over a century, mafic to ultramafic layered intrusions have intrigued geologists as records of crystal accumulation and magmatic processes, providing key insights into the origin of mafic and ultramafic igneous rocks (Grove and Brown, 2018; Scoates and Wall, 2015; Wager, 1952). Crystal accumulation and different crystallisation processes produce different rocks, including the BC rocks, such as gabbros, pyroxenites, dunites, chromitites (Wager *et al.*, 1960) The RLS igneous rocks formed from broadly basaltic magmas, and are of particular interest due to their distinct layering forming sill-like bodies (Irvine, 1982). The economically important RLS has been informally divided into 5 stratigraphic zones, from the base upwards, being the Marginal Zone, the Lower Zone (LZ), the Critical Zone (CZ), the Main Zone (MZ), and the Upper Zone (UZ) (Eales and Cawthorn, 1996; Smith *et al.*, 2023). These stratigraphic zones vary in thickness, with the LZ and CZ thinner in the Northern Limb and thicker in the Eastern and Western limbs (Barnes and Maier, 2002; Grobler *et al.*, 2019; Maier *et al.*, 2023).

The basal unit of the RLS is the Marginal Zone, which consists of noritic rocks, and above this unit is the LZ, dominated by dunite, harzburgite, and orthopyroxenite (Barnes and Maier, 2002; Scoates *et al.*, 2021). The overlying CZ is divided into the Lower Critical Zone (LCZ) and Upper Critical Zone (UCZ) (Barnes and Maier, 2002; Grobler *et al.*, 2019; Li *et al.*, 2005). The major PGE-mineralised zones are contained within the CZ and include the Merensky Reef, the Upper Group 2 (UG2) chromitite, and the Flatreef / Platreef, the latter occurring in the Northern Limb of the complex. The Flatreef / Platreef of the Northern Limb is correlatable with the upper reaches of the UCZ, including the Merensky and Bastard Reefs, of the Eastern and Western

limbs (Keet *et al.*, 2024; Maier *et al.*, 2023; McDonald *et al.*, 2005; Scoates and Wall, 2015; Smith *et al.*, 2023). The other chromitite layers within the CZ are referred to as the Lower Group (LG) 1-7, Middle Group (MG) 1-4, and Upper Group (UG) 1-3 chromitite seams (Barnes and Maier, 2002).

The LCZ is dominated by ultramafic rocks such as harzburgite, orthopyroxenite, and dunite (Barnes and Maier, 2002.; Grobler *et al.*, 2019). The LCZ hosts the LG1 to LG7, the MG1 and the MG2 chromitite layers (Barnes and Maier, 2002; Grobler *et al.*, 2019). From a PGE perspective, the UCZ contains the main economically mined layers, including the Merensky Reef, which is a relatively thin but laterally extensive sulfide-rich pyroxenite layer that carries high concentrations of PGEs. Plagioclase attains cumulus status in the UCZ, which contains orthopyroxenite, norite, anorthosite and the MG3-4 and UG1-3 chromitite layers (Barnes and Maier, 2002.; Grobler *et al.*, 2019). The MZ, which is the thickest zone of the RLS, has a dominantly noritic to gabbronoritic composition (Barnes and Maier, 2002). The rocks of the UZ are characterised by the presence of magnetite layers, diorites, gabbroic, and anorthosites (Barnes and Maier, 2002; Li *et al.*, 2005).

The dominant rock-forming minerals within the RLS are plagioclase, orthopyroxene, clinopyroxene, and olivine, with chromite being an important additional constituent in the CZ (Li *et al.*, 2005). Magnetite also occurs concentrated within the magnetitite layers of the UZ (Barnes and Maier, 2002; Scoates *et al.*, 2021). The compositional variability between the rock forming minerals of the RLS, is reflected in their chemical and optical properties, facilitating their identification and description. The rock-forming minerals of the RLS provide an ideal sample set for evaluating the use of multispectral imaging as a potential tool for drill-core logging, despite the limited range and number of spectral bands that are collected. Mineral spectral variability among RLS lithologies demonstrate the potential of this approach to be explored and refined.

In the mining industry, rocks are traditionally manually logged, which is time-consuming, labour-intensive, and expensive (Fu *et al.*, 2022, 2024). Decision-making, whether at a drill site or operational mine, is reliant on the logging outcome that may only be available in hours, days, or weeks, meaning decision-makers often rely on assumptions based on rock properties manually logged by geologists. Drill-core logging observation and interpretation may vary depending on the logger's experience and focus (Alzubaidi *et al.*, 2022; Fu *et al.*, 2024). This can lead to spatial inconsistencies, inaccuracies in quantifying mineral constituents in the

logged drill-cores, and potentially incorrect identification of the encountered lithologies. Geologists must rely on visual inspection when logging the core, meaning features indistinguishable to the naked eye will not be recorded. The emergence of digitisation, along with the continuous advancement of existing technologies, presents opportunities to optimise processes in PGE mineral exploration (Goetz and Rowan, 1981; Zumsprekel and Prinz, 2000). These developments reduce reliance on time-consuming and subjective manual methods, providing optimized, robust alternatives that improve decision-making capabilities and overall exploration efficiency (Minerals Council South Africa, 2023).

Reflectance spectroscopy has emerged as an increasingly valuable technological tool for digital mineral identification, lithological mapping, and determining mineral composition. However, its adoption in mining workflows is often constrained by factors such as cost, operational capability, and ease of deployment. In geological mapping, longwave-infrared (LWIR) imagery enabled by hyperspectral sensors has been widely utilised in geology due to its ability to detect silicate-rich rocks (Ninomiya *et al.*, 2005; Ninomiya and Fu, 2019). However, the high cost of hyperspectral imaging presents a barrier, particularly for platinum operations seeking cost-effective solutions that maximise profit. Multispectral imaging, while offering fewer spectral bands, could provide a more affordable alternative and can be explored as a viable tool for drill-core logging. Despite the limited spectral information, a detailed analysis of the available wavelengths may reveal distinct absorption features that are useful for distinguishing lithologies and enhancing the efficiency of drill-core logging.

The majority of rocks of the RLS display colours that can be described as various shades of gray, as classified using the Munsell colour system, with colours ranging from black (Munsell N1) to white (Munsell N9). White and gray, which are the most common colours of plagioclase (Nesse, 2009) suggest that the use of grayscale imagery derived from red, green, blue (RGB) images with sufficient spatial resolution may potentially be used to recognise various minerals, thereby classifying the rocks of the RLS. The RGB bands, which are visible to the human eye, along with additional spectral bands such as the red-edge (RE) and near-infrared (NIR) bands, which are not visible to the human eye, may enhance the ability to distinguish the RLS rocks when using multispectral imagery. Pyroxenes, which are common in intrusive mafic and ultramafic igneous rocks such as gabbro, pyroxenite, anorthosite, and norite, lithologies characteristic of the RLS, exhibit diagnostic absorption features within the visible to near-infrared (VNIR) spectral region (Mandende *et al.*, 2023; Nesse, 2009). This presents an

opportunity to integrate visible, RE, and NIR bands in multispectral imagery for effective mineral classification of the RLS rocks and also serves as a valuable tool for logging mafic to ultramafic lithologies of the RLS drill-core.

1.1 Objectives of the study

This study sets out to:

1. Evaluate the use of high-resolution RGB to grayscale imagery and multispectral imagery within the VNIR (400 - 842 nm) to classify the major minerals of the RLS in drill-core, as a potential tool for drill-core logging.
2. Assess the reliability of multispectral imagery (400 - 842 nm) for mineral classification and a high-resolution RGB to grayscale imagery approach in classifying the lithologies of the RLS drill-core as an assistive or alternative to traditional core logging using petrography and whole-rock geochemistry as validation tools.

2 Literature review

2.1 Traditional core logging

Mining companies and prospectors drill thousands of metres of drill-core during the exploration and operation stages of mining to gain a better understanding of the geological formations being explored or mined (Mandende *et al.*, 2023). Collecting as much data as possible during the exploration stage is essential, as it guides the development of the mine and decision-making stages. Once drill-cores are arranged in core boxes in traditional core logging, geologists visually inspect the core; identifying and recording key geological features such as lithology, mineralisation, alteration, veining, structures, and texture of the core (Acosta *et al.*, 2019; Fu *et al.*, 2024). Observations are recorded by hand or entered into printed or digital log sheets, which serve as standardised templates to consistently capture information, including depth intervals, rock types, mineral percentages, colour, core recovery, crystal size, rock-quality designation, and other notable features (Fu *et al.*, 2022, 2024; Mandende *et al.*, 2023; Tappert *et al.*, 2011).

Traditional manual core logging presents several challenges, including human error and bias, inconsistent data quality, limited resolution in detecting subtle geological features, and the time-consuming, labour-intensive nature of the process (Galdames *et al.*, 2019; Mandende *et al.*, 2023; Shukla and Kot, 2016). These limitations not only increase operational costs but hinder the integration of core logging data with modern digital datasets, potentially impacting the accuracy of geological models and decision-making in exploration and mining operations. Distinguishing different minerals quickly whilst minimising human error is an important step in lithological core logging. Mining companies use lithological and mineralogical information as an important part of the exploration process, but also in the process of mine and process design. Optimising the extraction of information necessary for lithological classification through the digitisation of drill-core logging can lead to increased efficiencies at any stage of the mining value chain (Acosta *et al.*, 2019; Kirsch *et al.*, 2023).

Core logging is sometimes completed in the field where environmental conditions might affect how the geologist describes the rock. Hence, core logging might be subjective to geologists leading to variations in logging results. For example, the colour recorded by the geologist varies if wet or not, such that when it is rainy or sunny, different colours might be observed because of the different light conditions affecting the material's reflectance. While standardised frameworks like the Munsell Colour Chart can assist consistent colour identification across

various disciplines, including geology, soil science, and environmental studies, they are not widely adopted as standard practice (Nederbragt *et al.*, 2006). Even though usage of the Munsell Colour Chart can be standardized across exploration and mining companies, the colour recorded is still based on visual observations (Dorador and Rodríguez-Tovar, 2016), therefore serving only as an aid in minimizing the subjectiveness of observations.

Colour is one of the important physical properties recorded when describing rocks and is often also useful for rock identification. Accurate colour identification is crucial as it can indicate mineral composition, weathering, alteration zones, and oxidation (Nederbragt *et al.*, 2006; Ollila, 1986). For instance, reddish hues may suggest the presence of hematite or oxidised zones, while greenish hues may indicate the presence of chlorite or other alteration minerals (Clark, 1999). However, minor colour variations may be indistinguishable to the eye, leading to the inaccurate recording of information during manual core logging. Thus, in the future, digitisation of drill-core logging will likely become a standard practice (Galdames *et al.*, 2019).

2.2 Imaging of drill-cores

Historically, core photography was employed to create visual reference records of drill-cores. Over time, photography became a widely adopted practice in core logging, providing a permanent, consistent visual dataset that supports geological interpretation and review (Fu *et al.*, 2024; Tappert *et al.*, 2011). The use of high-resolution RGB images provides the level of detail required for accurate core logging, enabling geologists to revisit sections remotely, verify observations, and share data across teams without direct physical access to the core itself. Advancements in digital imaging technologies have transformed core photography from basic visual documentation to the integration of multi- and hyperspectral imaging, enabling the extraction of detailed mineralogical and geochemical information from core samples to modernise drill-core logging (Mandende *et al.*, 2023; Tappert *et al.*, 2011). Furthermore, digital datasets enhance the accuracy, repeatability, and analytical capabilities of core logging and enable integration with geochemical and machine learning processes (Adão *et al.*, 2017; Asadzadeh and De Souza Filho, 2016). As a result, imaging has become a critical tool in reducing subjectivity and improving efficiency in exploration and mining operations.

Grayscale images represent variations in light intensity at each pixel using a single spectral band, assigning one intensity value per pixel (Biswas *et al.*, 2011; Jyothi *et al.*, 2015). The single band representation captures light intensity information without colour, making it suitable for analysing brightness and contrast features in an image. In geological workflows,

grayscale images are typically integrated into true or false colour composites to enhance feature extraction and emphasise subtle tonal or textural differences that may not be readily visible in standard RGB images (Van der Meer *et al.*, 2012). Grayscale images are often converted to 8-bit binary format, where each pixel is assigned an intensity value ranging from 0 to 255. The 8- bit format provides a good balance between image quality and storage efficiency, keeping file sizes manageable (Jyothi *et al.*, 2015).

The luminosity method is a method to convert an RGB image to a grayscale image by applying weighted values to each colour channel, 0.2989 for red, 0.587 for green, and 0.114 for blue (Jyothi *et al.*, 2015). It is commonly preferred among the various methods for converting RGB images to grayscale, such as the lightness and average methods (Biswas *et al.*, 2011). This is due to its computational efficiency and its use of a weighted average that reflects human sensitivity to different RGB channels (Biswas *et al.*, 2011). However, converting to grayscale significantly reduces image information, leading to the loss of critical data required for detailed lithological interpretation of rocks with complex mineralogical and textural variations. As a result, the standalone use of grayscale images in geological analysis remains limited because they are limited in their ability to represent complex visual data (Jyothi *et al.*, 2015). Nonetheless, the application of grayscale image statistics in the classification of RLS rocks presents a promising opportunity, as these rocks naturally exhibit a colour spectrum ranging from white to black. This variation in light and dark tones aligns well with the capabilities of grayscale imaging, potentially enabling effective logging of lithological units and rock properties based on luminance contrasts alone.

Spectral imaging techniques operate across the electromagnetic spectrum and includes both multispectral and hyperspectral imaging. Multispectral imaging typically uses 5-10 broader bands with lower spectral resolution (Shukla and Kot, 2016), whereas hyperspectral imaging captures hundreds of spectral bands that contain a specific range of wavelengths, enabling detailed material discrimination (Shukla and Kot, 2016; Adao *et al.*, 2017). Nonetheless, high-resolution multispectral imagery, with the use of improved classification models (Zumsprekel and Prinz, 2000) can effectively produce digital mineral classification maps, achieving performance comparable to hyperspectral imaging for minerals exhibiting significant spectral reflectance variability within target wavelength bands (Ninomiya and Fu, 2019; Qasim *et al.*, 2022). Multispectral and hyperspectral images covering the visible to the infrared parts of the electromagnetic spectrum (Zwinkels, 2015) have been tested and applied in various commodity

mines (Kirsch *et al.*, 2023; Kruse *et al.*, 2012; Murphy and Monteiro, 2013; Tappert *et al.*, 2011). This has been driven by the distinct spectral signatures many minerals exhibit in the VNIR and shortwave-infrared (SWIR) regions of the electromagnetic spectrum, enabling mineralogical characterisation (Acosta *et al.*, 2019; Mandende *et al.*, 2023).

2.3 Spectral analysis

Spectral signatures, such as reflectance peaks and troughs, arise from vibrational and electronic absorption processes, which are influenced by the interactions between atomic bonds and electron orbitals (Acosta *et al.*, 2019) (Figure 2.1). Geologists compare these signatures by analysing absorption and reflectance features as well as the overall spectral shape (Jakob *et al.*, 2017). These spectral signatures are stored in reference spectral libraries for mineral identification and characterisation, providing compositional standards (Kokaly *et al.*, 2017). A widely used resource is the United States Geological Survey (USGS) Spectral Library, available in the Environment for Visualising Images (ENVI) software and integrated into the iSpec Sam Thiele spectral search engine.

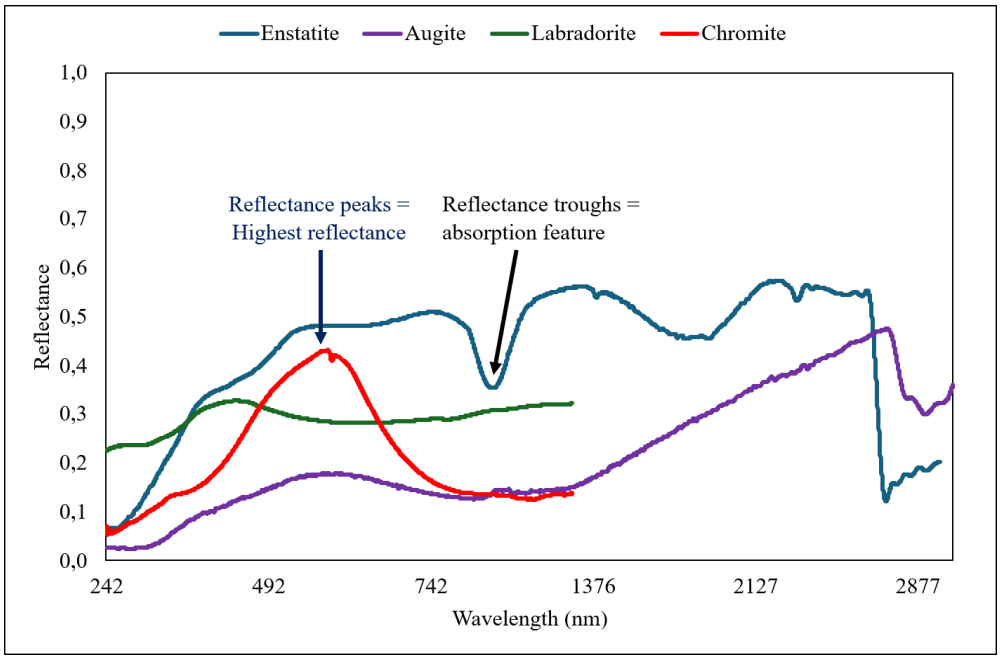

Figure 2.1: Reflectance features of major minerals of the Rustenburg Layered Suite across the visible, near-infrared, and shortwave-infrared range from the ENVI, USGS spectral library.

Spectra are acquired using laboratory, field, and airborne spectrometers, covering different wavelength ranges from the ultraviolet to the far infrared (Kokaly *et al.*, 2017). In this study,

the USGS Spectral Library Version 7 spectrometers were used due to their multiple spectral references of the same minerals within the target wavelength bands. The grain size and crystal structure affect the mineral's spectral signature, producing variations in spectral curves even for the same mineral (Kokaly *et al.*, 2017). Table 2.1 presents the responses of various silicate and non-silicate minerals across the VNIR, SWIR, and LWIR regions. It shows that mineral identification in these regions is possible through distinct absorption and reflectance features. (Mandende *et al.*, 2023). The highlighted minerals are the major minerals found in the RLS.

As seen in Table 2.1 and Figure 2.2, pyroxenes and olivine are diagnostic in the VNIR range, while feldspars and chromite are non-diagnostic. In the VNIR range of the spectrum, little to no differences are observed for feldspar and chromite, which lack distinct absorption features. Nonetheless, the small population of non-diagnostic minerals allows for the analysis of slight differences in spectral intensity, convexity, and slope (Jakob *et al.*, 2017). This does not imply that the far infrared data from hyperspectral imaging will address the issue, as some minerals remain non-diagnostic in the SWIR and LWIR. These observations highlight that even subtle spectral variations among key RLS minerals can offer valuable distinctions in the VNIR range, supporting efficient core logging.

Table 2.1: Diagnostic absorption features of minerals under VNIR, SWIR, and LWIR. Sourced from Terra-Core by Mandende *et al.* (2023), blue cells highlight major minerals of the RLS.

	Structure	Group	Mineral	VNIR	SWIR	LWIR
Silicates	Inosilicates	Amphibole	Actinolite	Non-diagnostic	Good	Good
		Pyroxene	Diopside	Good	Moderate	Good
		Olivine	Forsterite	Good	Non-diagnostic	Good
	Phyllosilicates	Mica	Muscovite	Non-diagnostic	Good	Moderate
		Chlorite	Clinochlore	Non-diagnostic	Good	Moderate
		Clay	Kaolinite	Non-diagnostic	Good	Moderate
	Tectosilicates	Feldspar	Albite	Non-diagnostic	Non-diagnostic	Good
		Silica	Quartz	Non-diagnostic	Non-diagnostic	Good
Non-silicates	Carbonates	Calcite		Non-diagnostic	Good	Good
	Oxides	Spinel	Chromite	Non-diagnostic	Non-diagnostic	Non-diagnostic
	Sulphides		Pyrite	Non-diagnostic	Non-diagnostic	Non-diagnostic

The Advanced Spaceborne Thermal Emission and Reflection Radiometer (ASTER) is another key source, capturing data in the VNIR, SWIR, and thermal infrared (TIR) ranges (Khaleghi *et al.*, 2014; Qasim *et al.*, 2022). The ASTER spectral library, also available in ENVI, is widely applied in lithological and mineralogical mapping (Ninomiya *et al.*, 2005; Ninomiya and Fu, 2019; Qasim *et al.*, 2022). Unlike the USGS library, ASTER contains rock spectra such as gabbro, pyroxenite, and anorthosite from the RLS of the BC, measured as directional hemispherical reflectance across the visible to shortwave infrared range. Directional hemispherical reflectance measures reflectance for illumination from a specific direction while integrating reflected energy over the entire hemisphere, better approximating natural illumination conditions in satellite remote sensing and improving the relevance of laboratory spectra for lithological mapping (Schaepman-Strub *et al.*, 2006; Baldridge *et al.*, 2009).

Other widely used libraries include the Johns Hopkins University spectral library, the Jet Propulsion Laboratory spectral library, and the ECOSTRESS spectral library, which collectively provide laboratory, field, and airborne spectra of minerals, rocks, soils, and vegetation across a broad wavelength range (Baldridge *et al.*, 2009; Kokaly *et al.*, 2017). Figure 2.2 presents the abstraction of the spectra of major rock-forming minerals of the RLS to the bands relevant to this study in the VNIR region from the USGS V7 Beckman Library, showing that while slight differences exist in the visible spectrum, analysis of the RE and NIR regions improves mineral discrimination, supporting the use of multispectral imaging as a viable tool for lithological and mineralogical mapping.

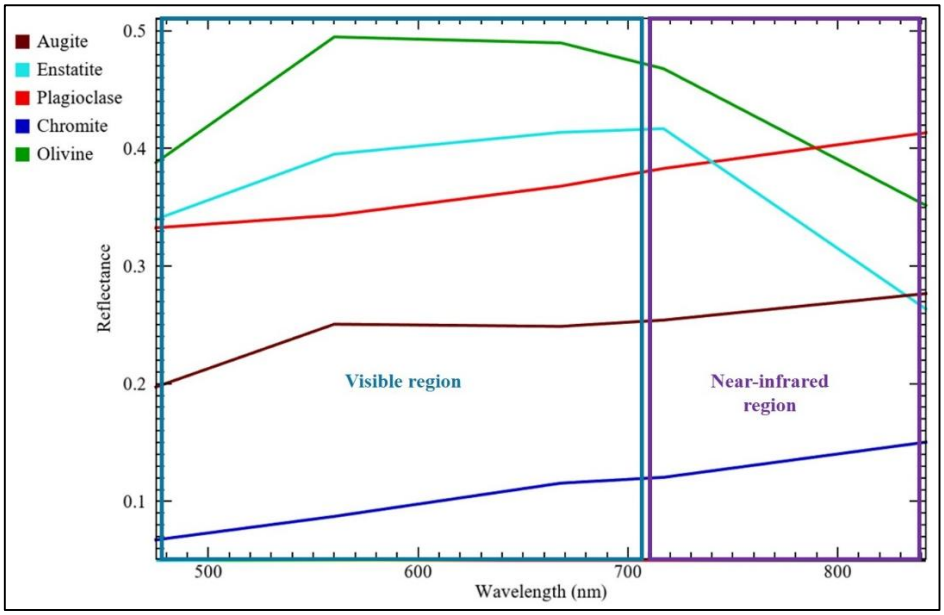

Figure 2.2: Spectral signatures of the major minerals of the rocks of the Rustenburg Layered Suite; blue and purple rectangles are visible and near-infrared regions, respectively.

2.4 Previous studies using multispectral imaging

Multispectral imaging, which records reflectance data across a limited number of discrete spectral bands across the 400-2500 nm range of the electromagnetic spectrum, has been widely employed in agriculture and forestry for monitoring crop health, analysing soil properties, and detecting land-use changes such as deforestation (Adão *et al.*, 2017; Chabrillat *et al.*, 2024; Laliberte *et al.*, 2011; Merino *et al.*, 2012; Turner *et al.*, 2011; Vuletić *et al.*, 2023). In geological applications, multispectral imaging has similarly been utilised for mineral identification and lithological discrimination. These applications are possible because multispectral datasets capture both spatial and spectral information, with minerals exhibiting diagnostic absorption features at specific wavelengths. The TIR region has been particularly useful for distinguishing compositional variations amongst rocks, allowing distinction between felsic and mafic lithologies, and for detecting silicate minerals like quartz, feldspars, and pyroxenes based on their unique thermal emissivity (Ninomiya *et al.*, 2005; Ninomiya and Fu, 2019).

The ASTER spectra also provide an opportunity to assess the difference between multispectral and hyperspectral data of rocks. Multispectral imaging allows detailed analysis of selected spectral bands, which can simplify the interpretation of certain spectral characteristics that may

be overlooked in the continuous and highly detailed nature of hyperspectral data. The difference can be seen from the ASTER spectra of rocks present in the BC where a single rock type can exhibit multiple spectral responses due to differences in mineral composition, grain size, weathering state, and surface conditions (Zhang and Li, 2014). This is demonstrated in Figure 2.3 where VNIR multispectral data effectively capture distinct spectral features at selected spectral bands, enabling the analysis of subtle compositional variations, whereas hyperspectral data provide continuous spectral information; their complexity can sometimes mask the finer diagnostic details

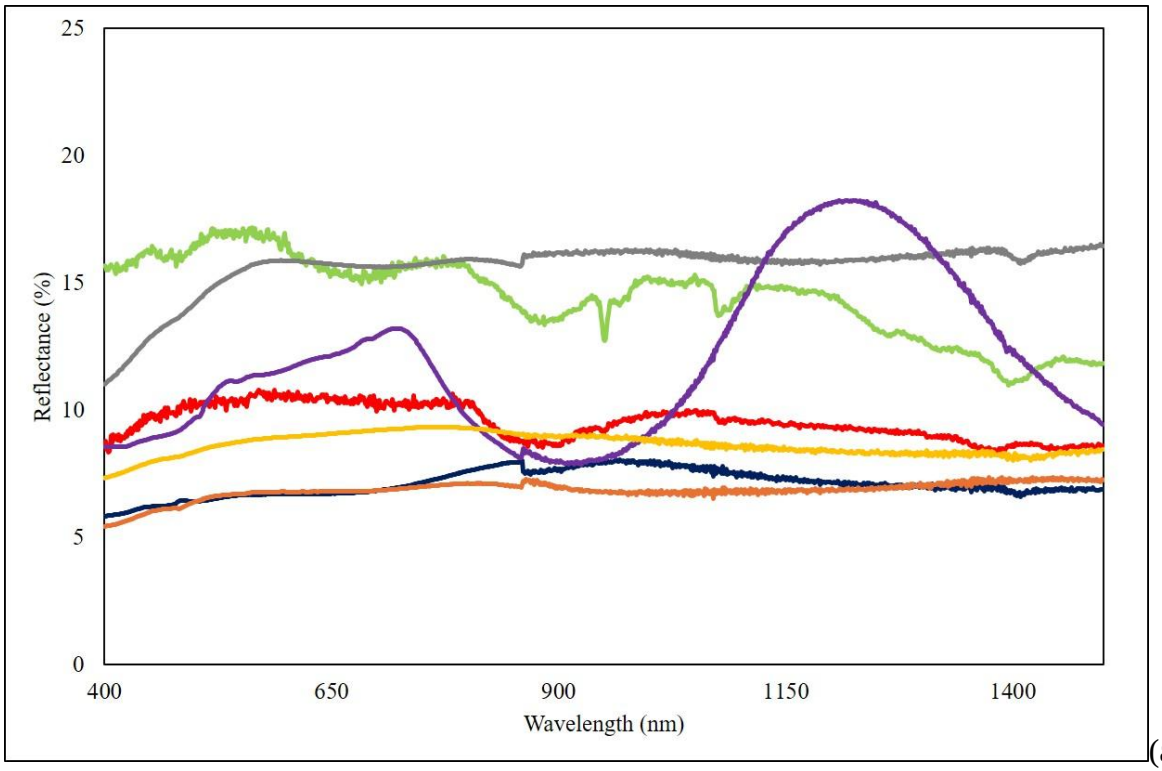

(a)

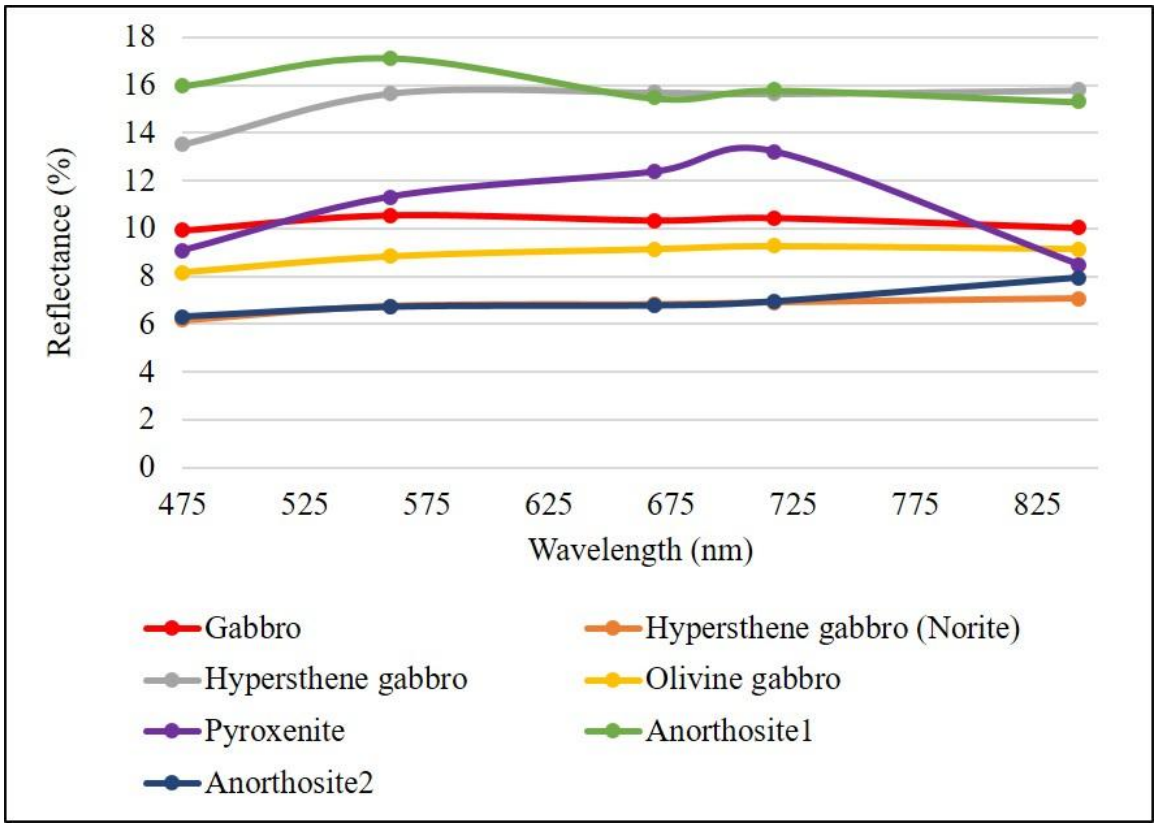

(b)

Figure 2.3: Bushveld Complex rock spectra derived from the ASTER hyperspectral repository (a) and converted to the visible-near infrared bands (b).

The image acquisition process and the conditions under which images are captured influence the subsequent processing steps. Kirsch *et al.* (2023) examined the influence of light and moisture, demonstrating that the handling of moisture and water-related artefacts impacts spectral responses, highlighting the need for proper data processing. This revealed the importance of lighting conditions, core handling, and image calibration. The correct preparation and processing of data from multispectral images is crucial, as raw spectral information, captured in digital numbers (DN), contains vast amounts of details that must be refined to extract meaningful insights. Correct data preparation is particularly critical when minerals exhibit weak or indistinct absorption features within the spectrum analysed, where these subtle variations in spectral absorption features are necessary for their identification and interpretation (Jakob *et al.*, 2017).

A widely adopted workflow in reflectance spectroscopy, applicable to both multispectral and hyperspectral approaches, typically involves: (i) converting raw sensor data to radiance, (ii) applying dark current and vignetting corrections, (iii) calibrating radiance to reflectance using a reference panel, (iv) performing geometric corrections to remove lens distortions, and (v) co-registering the imagery (Acosta *et al.*, 2019; Jakob *et al.*, 2017; Kirsch *et al.*, 2023; Kruse *et al.*, 2012). This pre-processing workflow (Figure 2.4), adapted from Jakob *et al.* (2017), addresses the geometric and radiometric challenges associated with data acquisition from airborne platforms to ground-based core imaging. The same principles are equally relevant to low-altitude or ground-based multispectral imagery used in geological logging, where accurate calibration and correction are critical for reliable interpretation. Moreover, the workflow incorporates topographic, radiometric, and atmospheric corrections to convert image radiance into reflectance (Jakob *et al.*, 2017; Kirsch *et al.*, 2023).

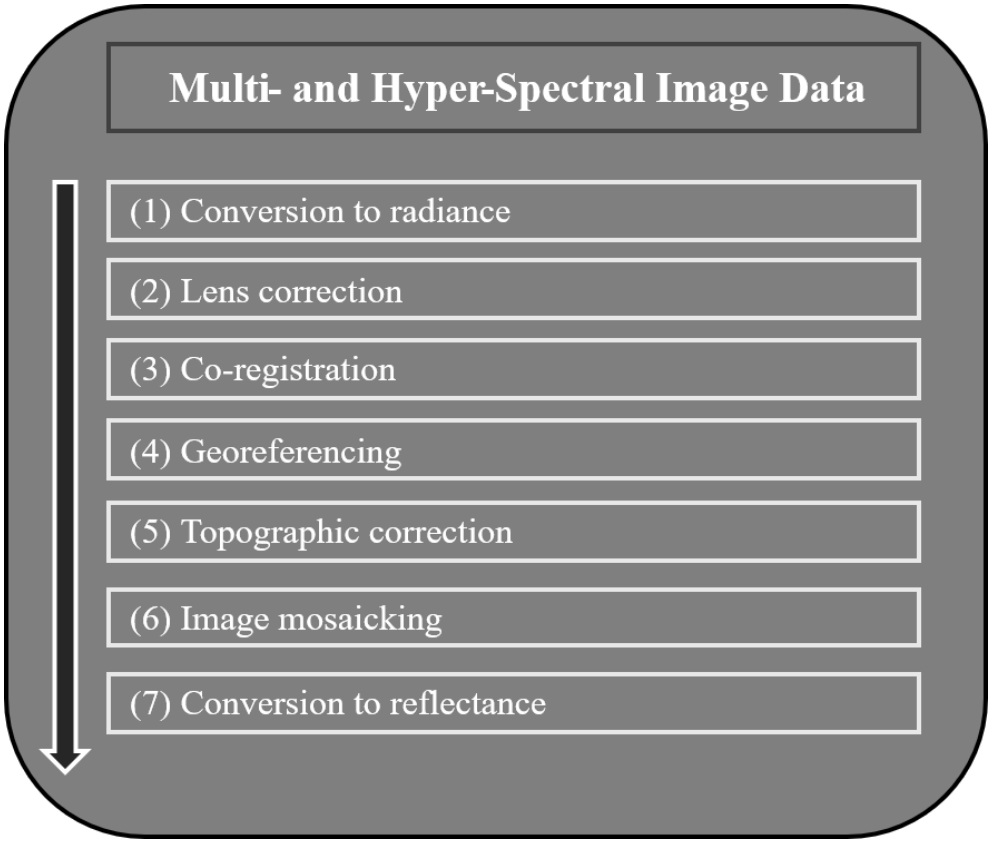

Figure 2.4: Processing workflow of multi- and hyper- spectral data adapted from Jakob *et al.* (2017).

Subsequently, dimensionality reduction techniques such as Principal Component Analysis (PCA) and Minimum Noise Fraction (MNF) enhance image interpretability by minimising redundancy and emphasising significant spectral features (Rahmat *et al.*, 2023; Santos *et al.*, 2024). The PCA is widely applied in mineral exploration for petrological and geochemical analysis (Ragland *et al.*, 1997; Sadeghi *et al.*, 2013), with the first three principal components capturing the majority of data variance. Minimum Noise Fraction improves signal-to-noise ratios, making it ideal for identifying spectral endmembers. Pure Pixel Index (PPI) computed from MNF-transformed bands helps locate pixels representing dominant mineral constituents, which are compared against reference spectra from USGS and ASTER libraries using ENVI software (Qasim *et al.*, 2022; Santos *et al.*, 2024). Additionally, endmembers can also be customised and applied through ENVI's Spectral Hourglass Workflow (SHW) for mineral detection in new regions (Santos *et al.*, 2024).

The SHW also incorporates algorithms for spectral classification using spectral endmembers. Among these, the Spectral Angle Mapper (SAM) is one of the most widely applied supervised

classification techniques. SAM compares the spectral angle between the spectral signature of an image pixel spectrum with reference spectra from known minerals from the spectral library (Hasan *et al.*, 2016; Khaleghi *et al.*, 2014; Liu and Yang, 2013; Meima and Rammlmair, 2020; Yonezawa, 2007), making it particularly effective for identifying specific mineralogical compositions (Meima and Rammlmair, 2020; Qasim *et al.*, 2022). This allows for accurate mineral identification, even in variable lighting conditions, as it is dependent on intensity (Meima and Rammlmair, 2020). Other approaches, such as Matched Filtering (MF) and Mixture-Tuned Matched Filtering (MTMF) (Routh *et al.*, 2018), enhance the detection of specific mineral signatures, even when they are mixed with others (Santos *et al.*, 2024). Linear Spectral Unmixing is another powerful approach, used to estimate the proportion of different materials within a single pixel where there are concerns with subpixel occurrence (Plaza *et al.*, 2004; Santos *et al.*, 2024). The application of these spectral classification algorithms ultimately produces mineral maps of drill-core, rock faces, and other geological materials under investigation.

In mineral exploration, multi- and hyperspectral imaging is increasingly combined with analytical techniques including bulk geochemical analysis, by means of X-ray fluorescence (XRF), determination of the bulk mineralogical composition using X-ray diffraction (XRD), optical microscopy, and scanning electron microscopy with mineral liberation analysis to enhance mineral identification, lithological classification, and resource estimation (De La Rosa *et al.*, 2021; Mandende *et al.*, 2023; Meima and Rammlmair, 2020; Tappert *et al.*, 2011). Back-scattered electron imaging by SEM generates grayscale images within the 0-255 range, where brighter areas indicate minerals with higher average atomic numbers (containing heavier elements; e.g. lead) and darker areas indicate lower atomic numbers (containing lighter elements; e.g. sodium) (De La Rosa *et al.*, 2021). Although laboratory methods provide detailed mineralogical and geochemical information, they are time-consuming, destructive, and limited to small sample sets in operational environments where rapid decision-making is required.

Spectral imaging, by contrast, offers a rapid and non-destructive means of mineralogical characterisation, with laboratory analyses typically used for validation. For instance, Khaleghi *et al.* (2014) and Tappert *et al.* (2011) validated alteration mineral maps with thin-section petrography and XRD, while Kirsch *et al.* (2023) integrated hyperspectral imaging with XRD and Laser-Induced Breakdown Spectroscopy (LIBS) to quantify mineral abundances. Similarly, Meima and Rammlmair (2020) combined XRF with spectral angle mapper (SAM)

classification to interpret LIBS images, and Mandende *et al.* (2023) applied high-resolution hyperspectral core scanning to identify apatite-rich zones in the BC, which were subsequently validated using SEM.

Major element compositions obtained by XRF analysis can be utilised to derive normative mineralogy for igneous rock classification, following the CIPW norm calculation scheme developed by Cross, Iddings, Pirsson, and Washington (Rollison, 1993; Verma *et al.*, 2003). The studies (Khaleghi *et al.*, 2014; Kirsch *et al.*, 2023; Tappert *et al.*, 2011; Meima and Rammlmair, 2020) presented above emphasise the value of integrating multiple analytical techniques in mineral exploration, achieving results comparable to traditional core logging while reducing dependence on these methods (Mandende *et al.*, 2023; Tappert *et al.*, 2011).

2.5 Igneous rock classification systems

Understanding igneous rock classification is essential for the precise lithological logging of drill-core extracted in the course of exploration of the RLS. Igneous rocks may be classified based on their texture, chemistry, mineralogy, and petrography (Le Bas and Streckeisen, 1991). Texture provides clues about the cooling history and emplacement depth, while mineralogical and chemical data reflect the magma's origin and evolution (Philpotts and Ague, 2009).

The International Union of Geological Sciences (IUGS) classification standardises igneous rock nomenclature globally based on modal mineral percentages in igneous rocks determined by examining thin sections under a petrographic microscope (Streckeisen, 1980; Le Bas & Streckeisen, 1991). It primarily uses the Quartz-Alkali Feldspar-Plagioclase-Feldspathoids (QAPF) diagram to classify rocks with a colour index less than 90, i.e. containing less than 90 modal% mafic minerals (Figure 2.5a) (Streckeisen, 1976; Le Bas & Streckeisen, 1991). The QAPF diagram (Figure 2.5a), subdivided into the upper QAP and lower APF triangles, applies to silica oversaturated and silica undersaturated, feldspathoid-bearing plutonic rocks, respectively.

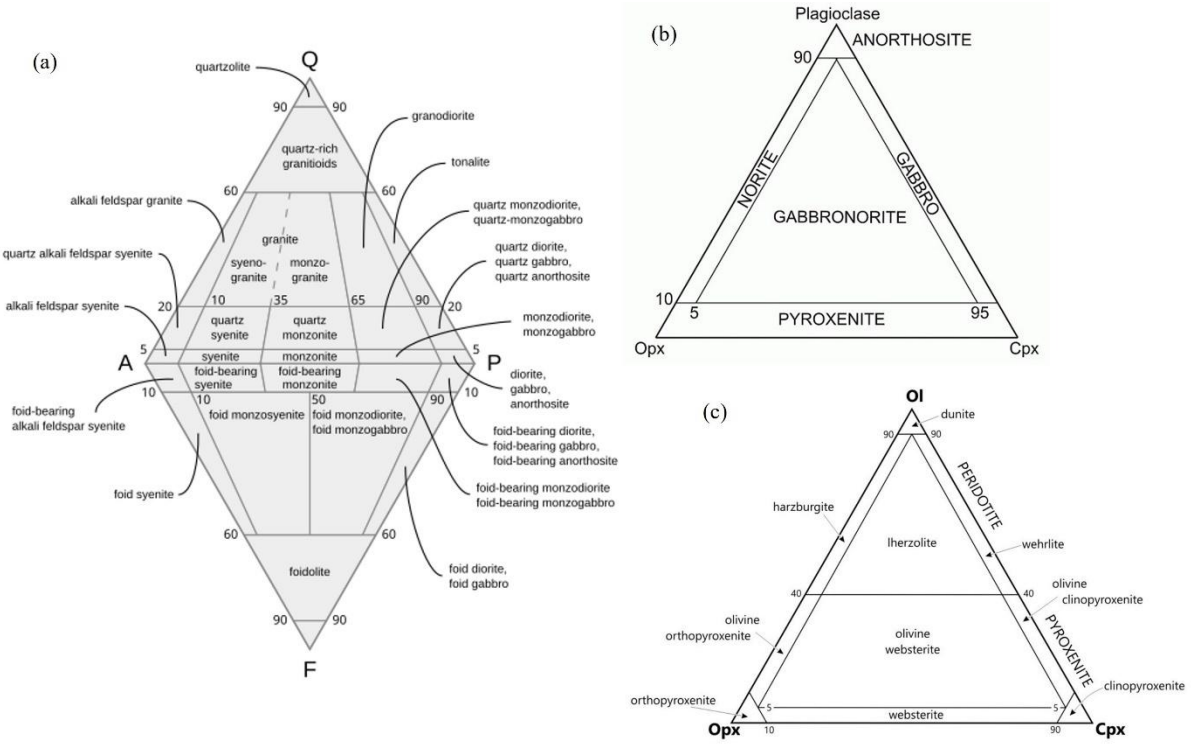

Figure 2.5: QAPF diagram used for the classification of plutonic igneous rocks based on their modal mineralogical composition after Streckeisen (1976) (a) the gabbroic rocks according to the relative abundance of plagioclase, orthopyroxene, and clinopyroxene (b). Ultramafic rocks containing olivine, orthopyroxene, and clinopyroxene, classifying the pyroxenitic and peridotite rocks (c) (Le Maitre, 1984; Stanley, 2017).

In those parts of the RLS where mafic intrusive rocks dominate, the IUGS classification provides a systematic framework for lithological identification based on observed mineralogy, particularly plagioclase and pyroxenes (orthopyroxene and clinopyroxene), following the classification of gabbroic rocks after Streckeisen (1976) and Le Bas & Streckeisen (1991). Anorthosite is composed mainly of plagioclase, typically labradorite and bytownite in layered intrusions (Streckeisen, 1976). Streckeisen (1976) further classifies the gabbroic rocks according to the relative abundance of plagioclase, orthopyroxene, and clinopyroxene (Figure 2.5b) (Le Maitre, 1984). Prefixes like mela- and leuco- are used to indicate that specific rocks are richer in mafic or felsic constituents, respectively, than what is considered "typical" for the rock in question. (Streckeisen, 1976; Le Bas & Streckeisen, 1991; Le Maitre, 2002). Ultramafic rocks (those with a colour index >90) are classified according to the relative proportions of mafic minerals, primarily olivine, pyroxenes, and hornblende. For rocks dominated by olivine, orthopyroxene, and clinopyroxene, this classification framework is used to distinguish between peridotite and pyroxenite varieties encountered in the lower reaches of the RLS. (Figure 2.5c) (Le Maitre, 1984).

3 Research methodology

3.1 Geology of the study area

The core used to conduct this study is the 1876.1 m long drill-core from borehole BH7929, which was drilled on the farm Elandsheuvel JQ 0282, northeast of Rustenburg in the Western limb (described under chapter 1) of the BC (Figure 3.1).

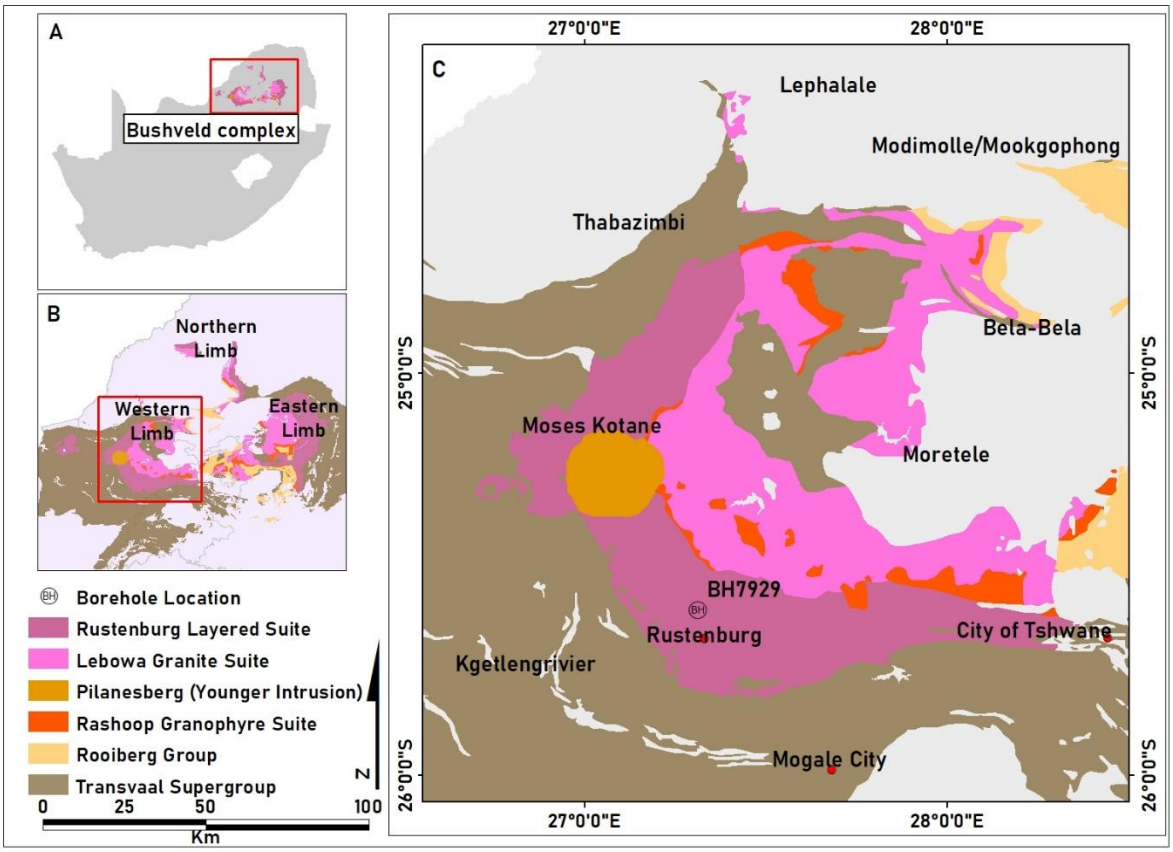

Figure 3.1: Location and geological map of the Bushveld Complex, the constituent limbs of the Rustenburg Layered Suite, and that of the studied borehole. Location of the Bushveld Complex relative to the landmass of South Africa. The red square shows the extent of the Bushveld Complex (a). Surficial geological expression of the Bushveld Complex rocks relative to the landmass of South Africa. The red square shows the area in c of the dominant surface coverage in the Western Limb of the Rustenburg Layered Suite (b). Geological map of the Western Limb of the Rustenburg Layered Suite, with local municipalities indicated, showing the location of borehole BH7929 (c). Maps prepared using data of the Council for Geoscience.

Impala Platinum Ltd donated the core to the University of the Free State. Stratigraphically, borehole BH7929 extends through part of the MZ (with a thickness of 1328.17 m), the entire

UCZ, and the upper reaches of the LCZ down to the level of the LG6 hanging wall (Figure 3.2).

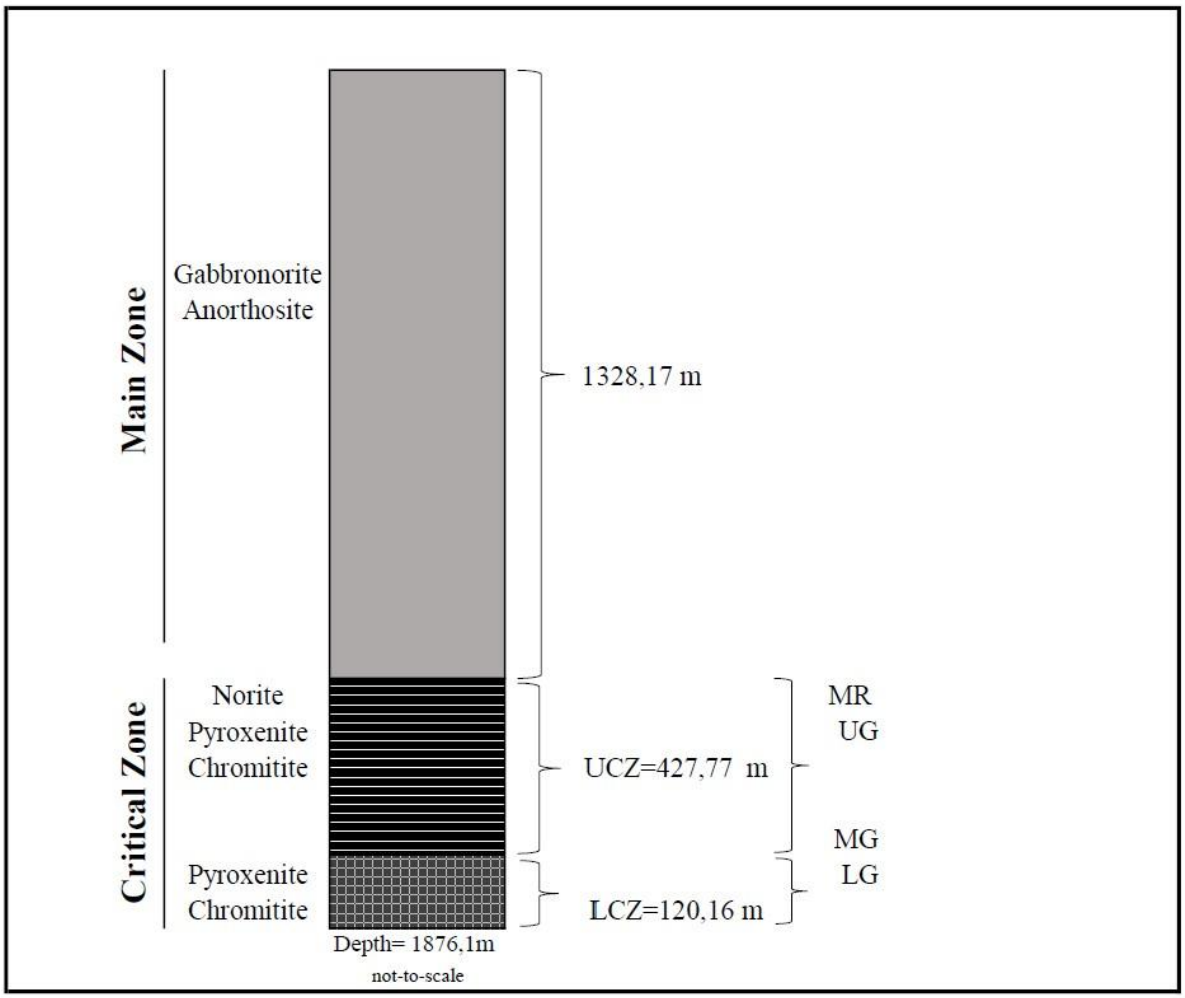

Figure 3.2: Simplified stratigraphic column of BH7929.

The MZ in BH7929 consists mainly of medium-crystalline gabbronorite. Lithologies in the UCZ include norite, pyroxenite, chromitite, and anorthosite. The top of the UCZ consists of a thick mottled anorthosite, known as the Giant Mottled Anorthosite (GMA) (Grobler *et al.*, 2019; Maier *et al.*, 2023). Beneath this are interlayered barren norite and pyroxenite, followed by a PGE-rich pyroxenite unit that forms the Bastard Reef (Grobler *et al.*, 2019; Maier *et al.*, 2023). This is succeeded by the Merensky Cyclic Unit, which begins with poorly mineralised or barren norite or pyroxenite. Below this lies a medium-crystalline, mineralised pyroxenite. The Merensky Reef with its footwall and the UG2, UG1, MG4, and MG3 chromitites are intersected. The contact between the UCZ and the LCZ was intersected at a depth of 1755.94 m. The LG7 chromitite layer of the LCZ was the lowermost chromitite layer intersected.

3.2 High-resolution RGB and multispectral cameras

To evaluate the use of high-resolution visible (RGB) and multispectral images as a potential tool for drill-core logging, high-resolution RGB and multispectral images were captured from several sections of the core using a Sony RX1RII and MicaSense RedEdge Panchromatic (RE-P) camera (Figure 3.3), respectively. The Sony RX1RII camera captures colour images within the visible light spectrum with 3 channels (red, green, and blue) as compared to the MicaSense Red-Edge Panchromatic (RE-P) camera of multispectral images with the addition of 2 more channels (RE and NIR).

Figure 3.3: The cameras utilised in this study (a) Sony RX1R II (b) MicaSense RE-P.

The Sony RX1R II camera is a high-resolution compact camera featuring a 42.4-megapixel full-frame Exmor R Complementary metal-oxide semiconductor (CMOS) sensor with a fixed 35 mm lens that captures detailed images with excellent dynamic range, even in low light, and is known for its sharpness and low distortion (Canter, 2023; Wiącek, 2020) (Table 3.1). The camera is powered by the BIONZ X image processor, allowing fast image processing and support for 14-bit uncompressed RAW files, preserving image quality for advanced editing (Sony Web Manual). The sensor is sensitive to the visible light spectrum, typically covering a wavelength range of approximately 400-700 nm, making it suitable for high-resolution RGB imaging. In remote sensing and photogrammetry, the Sony camera is often utilized in aerial surveys and UAV-based imaging platforms where high-resolution RGB data are required (Bobkowska *et al.*, 2024; Canter, 2023; Wiącek, 2020). Despite its compact size, the Sony RX1R II delivers professional-level image quality and is comparable to high-resolution smartphones, which can be used for capturing core images. Additionally, its compact size and lightweight design allow for seamless integration into drone systems (Wiącek, 2020).

The MicaSense RE-P camera is a frame-based multispectral camera that captures six spectral bands using separate monochrome sensors, including a high-resolution panchromatic band.

The spectral bands are five narrow multispectral bands (Blue (B): 475 nm, Green (G): 560 nm, Red (R): 668 nm, Red-Edge (RE): 717 nm, and Near-Infrared (NIR): 842 nm) and one 5.1 MP panchromatic band (Table 3.1) (MicaSense, 2017). The inclusion of the high-resolution panchromatic band in the RedEdge-P also allows for pan-sharpening, which not only enhances spatial detail but can also assist in improving the alignment of the lower-resolution multispectral bands. Each sensor has its optical path, which can cause slight image misalignment due to differences in lens position, distortion, and perspective. These misalignments are common in raw data but can be corrected during post-processing using software like Agisoft Metashape and other software with georeferencing tools. The MicaSense cameras with up to 10 spectral bands within the 400-1100 nm range and global shutter ensure all bands are captured simultaneously, minimizing motion blur and making it well-suited for UAV-based remote sensing applications like vegetation and water-quality monitoring, land classification, pollution, and precision agriculture application (Barjaktarovic *et al.*, 2024; Bobkowska *et al.*, 2024; Simpson *et al.*, 2024; Staniszewski *et al.*, 2024; Tysiąc *et al.*, 2025; Vuletić *et al.*, 2023).

Table 3.1: Camera specifications.

Specifications	**Sony RX1RII (RGB) Camera**	**MicaSense RedEdge (multi-spectral) camera**
Zone of spectrum covered	Visible	Visible, Near-infrared (NIR)
Spectral bands	3 bands (red, blue, green)	5 bands (blue, green, red, red-edge, NIR)
Wavelength range and wavelength centres	400 - 700 nm	Blue (475 nm), green (560 nm), red (668 nm), red-edge (717 nm), NIR (842 nm), panchromatic (634.5 nm)
Spectral bandwidth	Not applicable	Blue (32 nm), green (27 nm), red (16 nm), red-edge (12 nm), NIR (57 nm), panchromatic (463 nm)
Pixel size (spatial resolution)	42.4 MP	1456 x 1088 (1.58 MP per multispectral band) and 2464 x 2056 (5.1 MP panchromatic band)
Focal length of lens	32.8 mm (1.29 in)	5.5 mm (0.22 in)
Sensor type	Full Frame 35mm	Global Shutter Frame 6.3mm
Camera model number	10.00342.02	MSPN 900-00028
Output file format	14-bit uncompressed RAW (Sony ARW 2.3 format)	12-bit, ENVI compatible

The MicaSense RE-P camera contains a plastic case that contains a light gray calibration square and a QR code. The large gray square adjacent to the QR code serves as a calibrated reflectance panel (CRP) (MicaSense, 2024), which contains calibration data used to convert raw pixel values from the captured images into absolute reflectance values (Appendix B). Every MicaSense panel is individually tested to determine its reflectance across the specific wavelengths measured by the specific MicaSense sensor. The specific CRP used in this study, with model number RP06-2210469-OB, provides albedo values and absolute reflectance data (between 0-1.0) across the VNIR spectrum. Although the QR code on the panel may list values ranging from 250 nm to 950 nm, the actual reflectance values used in this study obtained from MicaSense, are 0.4732, 0.4743, 0.4739, 0.4734, and 0.4713 for the wavelengths 475, 560, 668, 717, and 842 nm, respectively. These correspond to the five spectral bands captured by the camera (Figure 3.4), which differ in recorded contrast and light intensity because each band represents a unique portion of the electromagnetic spectrum and therefore responds differently to the spectral properties of surface materials, atmospheric effects, and the sensor's spectral response function; these differences influence how energy is absorbed, reflected, or scattered at each wavelength hence the need to calibrate remote sensing data (Clark *et al.* 2002). A photo of the calibration panel was taken with each image capture but can be taken before and after capturing. The RE-P camera was mounted on a Wingtra drone to serve as its power source.

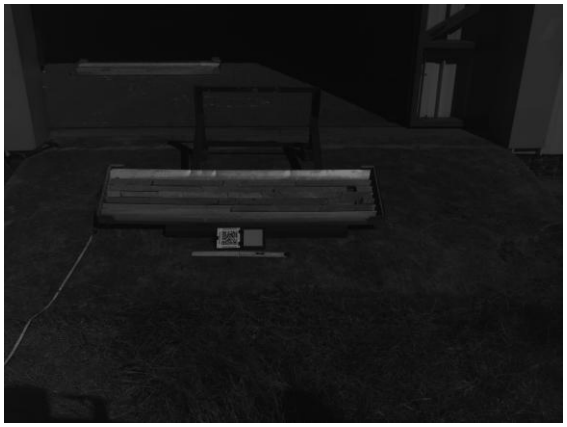

(a) Band 1: Blue

(b) Band 2: Green

(c)Band 3: Red

(d) Band 4: Near-Infrared

(e)Band 5: Red-Edge

(f) Band 6: Panchromatic

Figure 3.4: Multispectral band images captured with a MicaSense RE-P camera.

3.3 Data acquisition

3.3.1 Image data

High-resolution visible (RGB) and multispectral images were captured from various sections of the BH7929 core. These sections were selected based on the lithological variability of BH7929 to capture the major MZ and CZ rock types. Natural light was used to illuminate the core. Images were taken from a distance that allowed the entire core box to be captured in a single image. The subsequent sections outline the procedure followed for capturing the multispectral images for training and validation images.

A) Test 1:

Initially, test drill-cores were selected based on the variability of the core and images of whole rounds were collected, i.e. the core was not halved. Three images were captured for each core box at varying distances ranging from 1 m to 4 m. After spraying the core with water, three additional images were taken at each distance. This test demonstrated that images collected at approximately 3 m from the core box were optimal for capturing the entire core box in a single frame, whereas at distances shorter than 2.5 m, the core box was not fully included in the frame. These images were not analysed further for two reasons:

a) **The influence of water:** Wet surfaces affected reflectance, making the core image appear too dark to visually distinguish different features.
b) **Uneven light distribution from the whole round core surface:** The cylindrical shape of the core caused uneven illumination, with some areas receiving more light than others, leading to shadow effects and radiance variations of the same material with its position towards or away from the incident sunlight.

B) Test 2:

For the second test, selected drill-core sections from the MZ and UCZ were cut longitudinally in half using an automated circular saw with a diamond blade expose fresh, flat surfaces and then dried to prevent water interference with mineral reflectance. Kirsch *et al.* (2023) similarly to Test 1 demonstrated the impact of water, showing that the overall reflectance is reduced by 40-50% and interferes with absorption features. The flat surface was positioned upward to capture multispectral images using the MicaSense RE-P camera and to enable detailed manual logging and better visual examination.

Core boxes were angled at approximately 35° from horizontal towards to maximize sunlight illumination as images were captured around midday. Figure 3.5 illustrates a schematic diagram of the image capture process. Images captured include Image 1 (561.26 m to 568.7 m), Image 2 (919.88 m to 927.35 m), Image 3 (1373.84 m to 1380.88 m), and Image 4 (1509.58 m to 1517.02 m) (Figure 3.6). These images were taken from a distance of ~3 m, with cameras angled towards the core and held at ~2 m above the ground parallel to the corebox. These images were used as training images in the study.

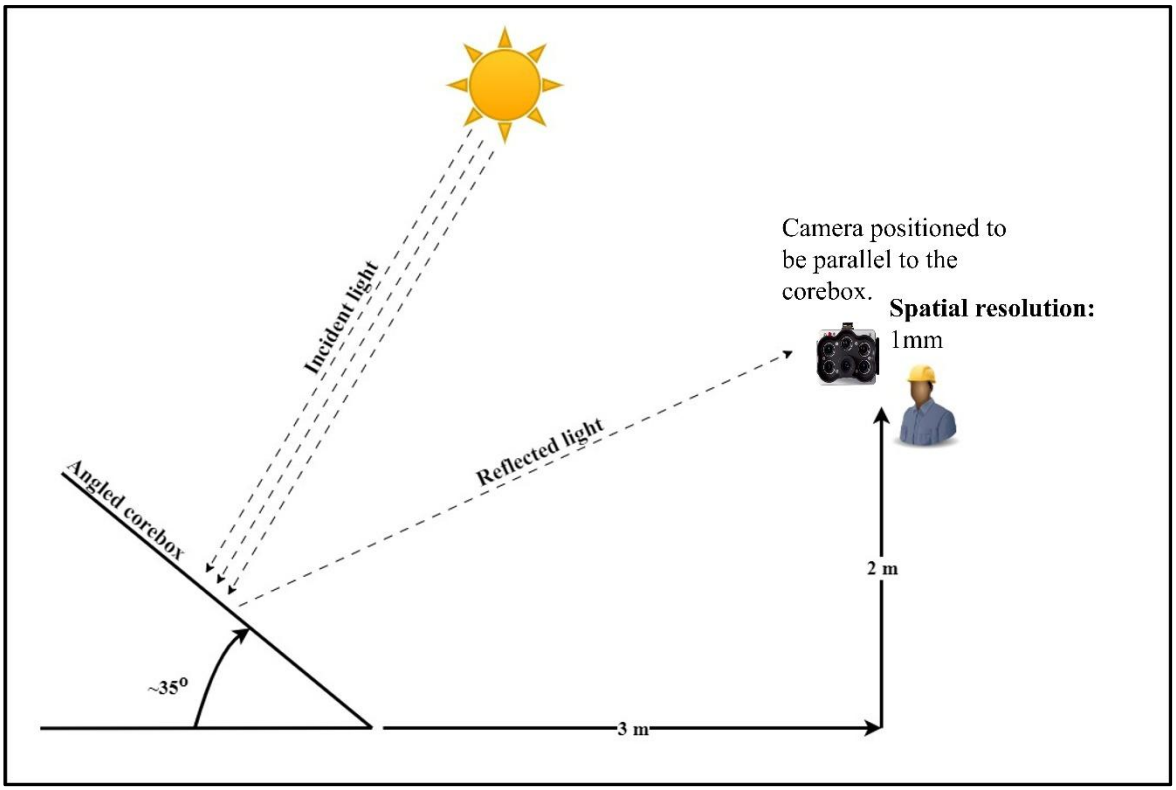

Figure 3.5: Schematic diagram of the image capturing process.

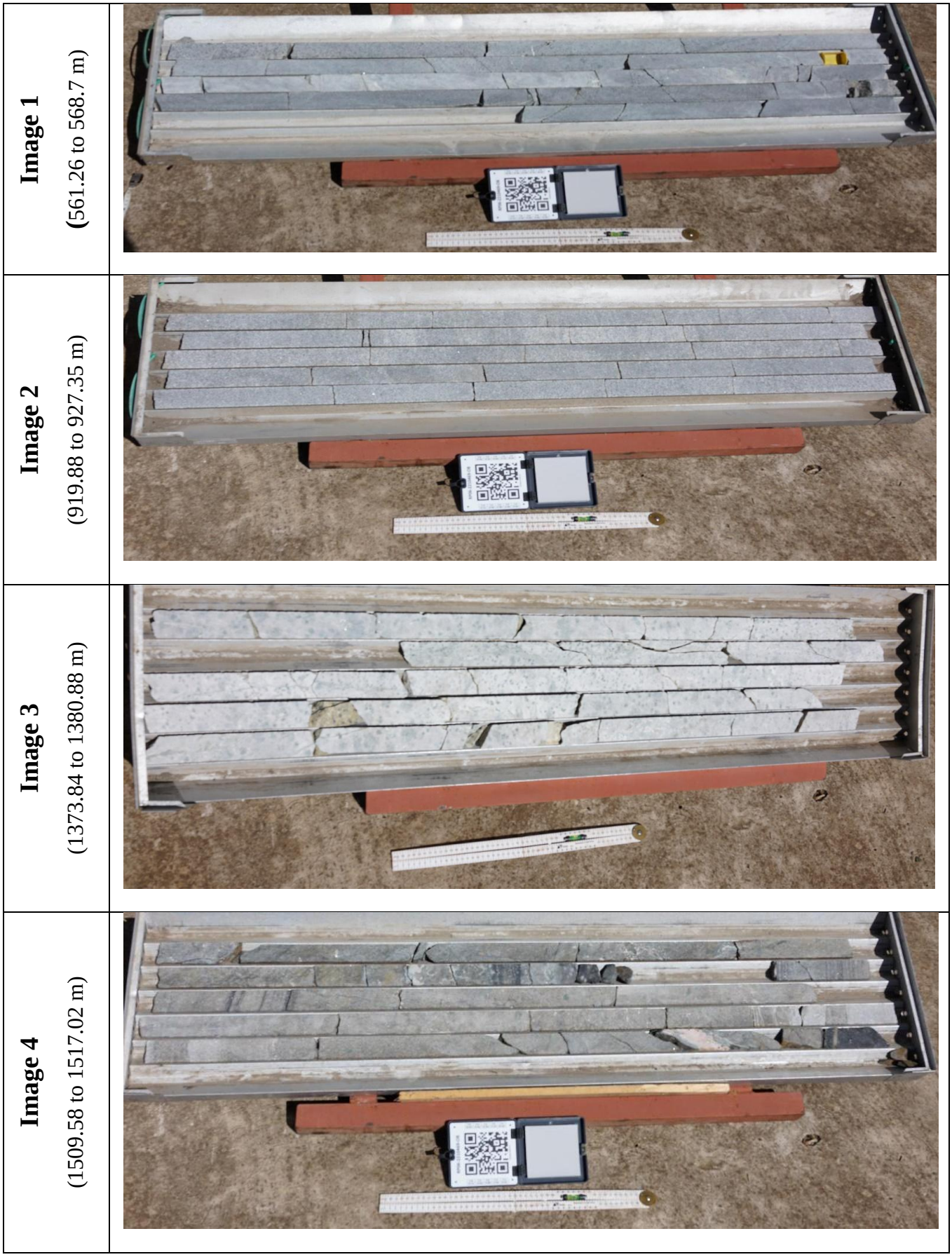

Figure 3.6: RGB images from Test 2 collected using the Sony RX1RII camera.

C) Test 3: Validation images

These sections were selected to test and evaluate the ability of the methodology developed in the dissertation to identify "unknown" sections of the core accurately for both the grayscale and multispectral approaches. The image capturing process utilised during Test 2 was maintained to obtain comparable results. Image 5 was taken from the MZ at a depth of 576.09 to 583.45 m, while Images 6 and 7 were captured from the UCZ at depths 1402.83 m to 1409.62 m and 1559.52 m to 1564.72 m, respectively (Figure 3.7).

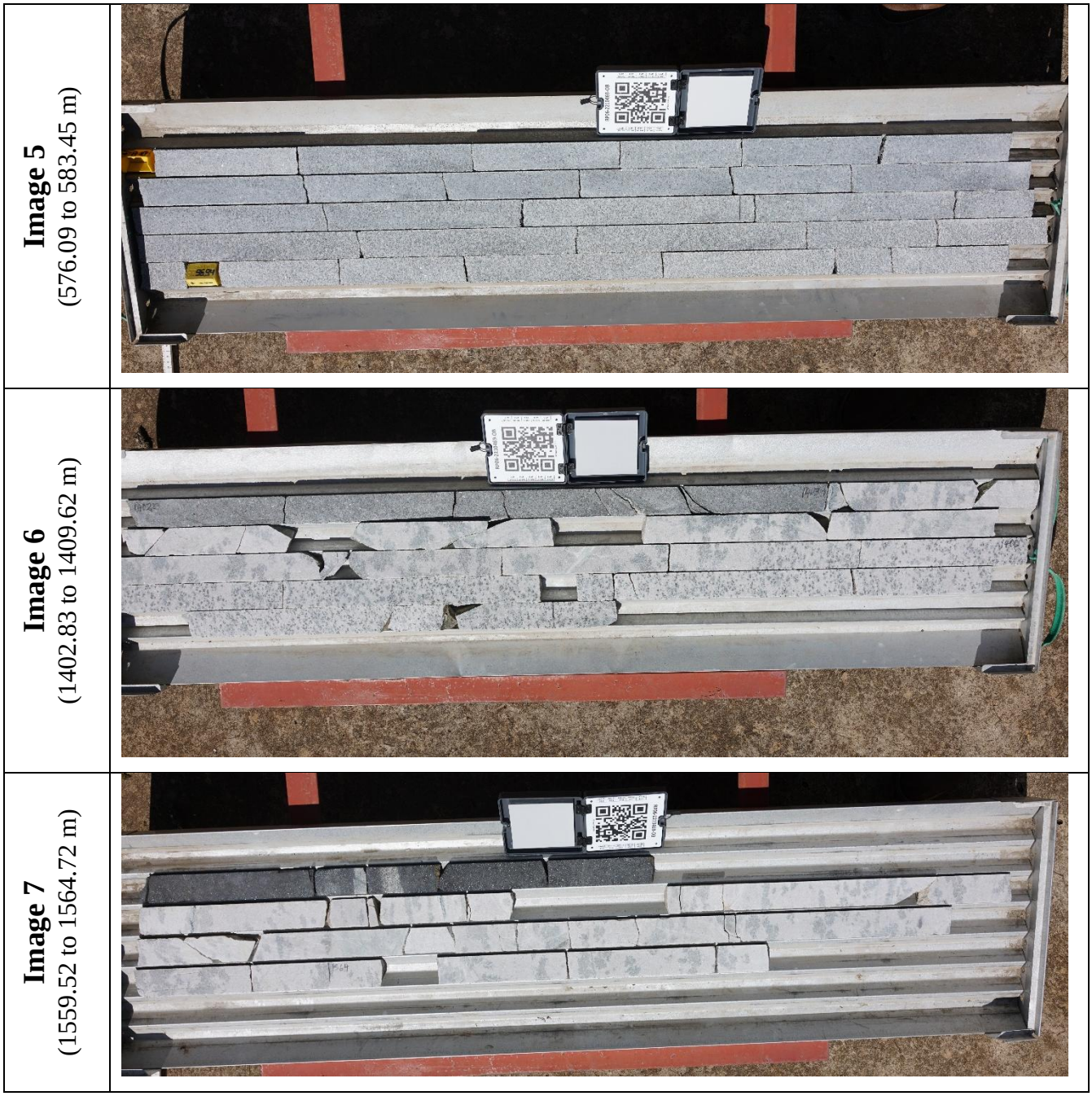

Figure 3.7: RGB images from the Sony RX1RII camera captured in Test 3.

3.3.2 Sampling and sample preparation for geochemical and mineralogical characterisation of drill-cores

Twenty-five samples representative of the major lithologies of the MZ and CZ of the RLS were collected from the cores imaged in Test 2 to assist with lithological classification (Figure 3.8). Fifty percent of the sample was used for geochemical analysis, while the remaining 50% was reserved for the preparation of thin sections. Sample lengths ranged from 4 to 22 cm (Table 3.2). Polished thin sections were prepared by a commercial laboratory, Lab Crystals, in India.

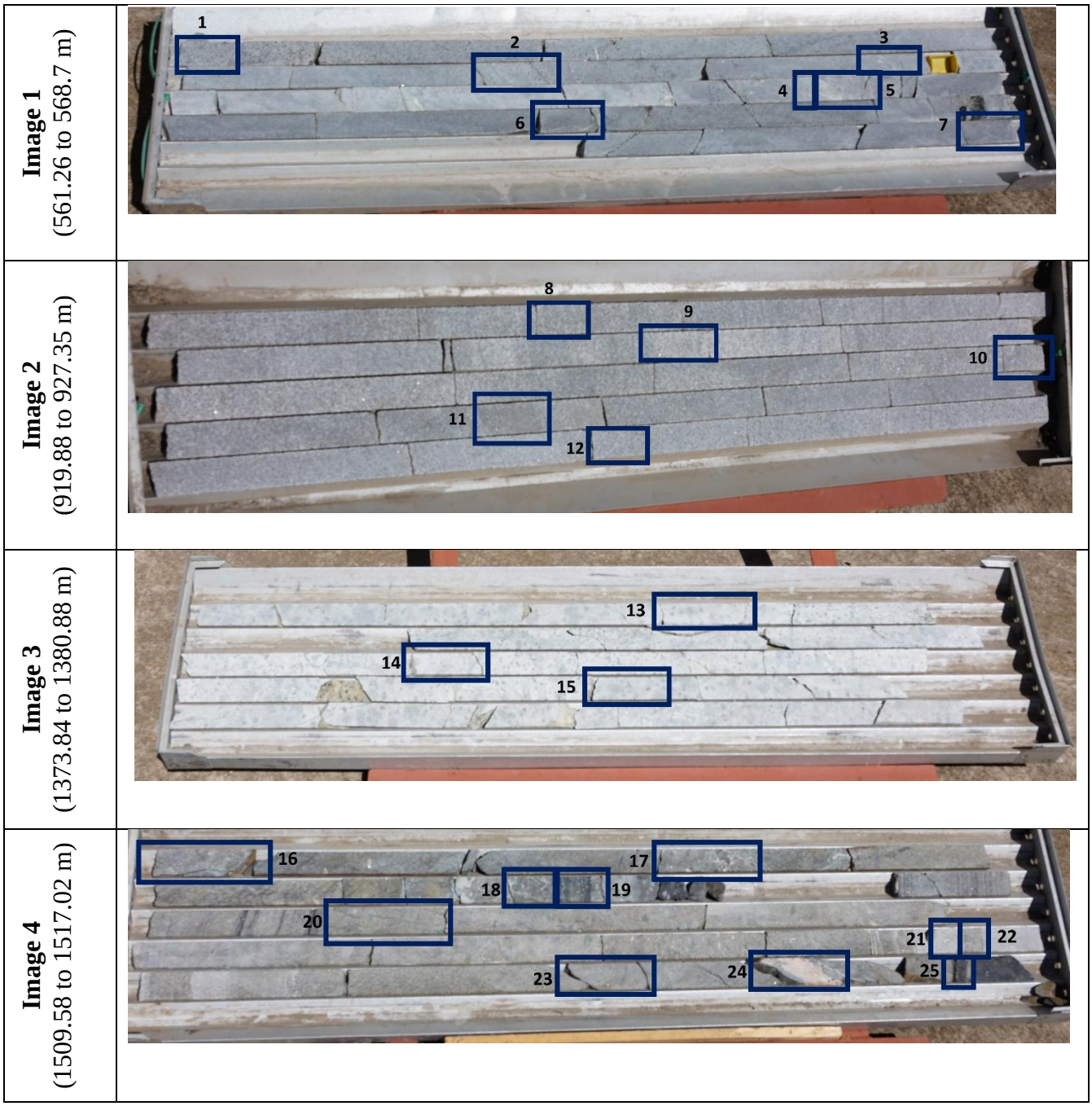

Figure 3.8: Locations of the 25 samples collected.

Table 3.2: List of samples collected from the core boxes imaged in Test 2.

Sample ID	Image	From (m)	To (m)	Length (m)
BH29-NM-01	Image 1	561,26	561,36	0,10
BH29-NM-02		563,27	563,40	0,13
BH29-NM-03		563,96	564,07	0,11
BH29-NM-04		565,30	565,34	0,04
BH29-NM-05		565,30	565,40	0,10
BH29-NM-06		566,33	566,44	0,11
BH29-NM-07		568,56	568,66	0,10
BH29-NM-08	Image 2	920,41	920,53	0,12
BH29-NM-09		922,19	922,30	0,11
BH29-NM-10		924,26	924,36	0,10
BH29-NM-11		924,49	924,59	0,10
BH29-NM-12		926,45	926,55	0,10
BH29-NM-13	Image 3	1374,70	1374,86	0,16
BH29-NM-14		1377,11	1377,23	0,12
BH29-NM-15		1378,89	1379,02	0,13
BH29-NM-16	Image 4	1509,58	1509,74	0,16
BH29-NM-17		1510,42	1510,60	0,18
BH29-NM-18		1511,61	1511,69	0,08
BH29-NM-19		1511,69	1511,77	0,08
BH29-NM-20		1512,80	1513,02	0,22
BH29-NM-21		1515,21	1515,26	0,05
BH29-NM-22		1515,26	1515,31	0,05
BH29-NM-23		1516,11	1516,23	0,12
BH29-NM-24		1516,42	1516,56	0,14
BH29-NM-25		1516,77	1516,85	0,08

3.3.3 Analytical methods

3.3.3.1 Whole-rock major and trace element analysis

Samples (Table 3.3) from the core were selected based on the variability; the more lithological variable, the more samples were taken from a specific core box. Half of each sample was used for geochemical analysis. Fused beads and pressed powder pellets were prepared for the analysis of major and trace elements, respectively, at the Geology Department of the University of the Free State (UFS). For calibration purposes, NIM-P and NIM-N certified reference materials were used.

To prepare fused beads, 10 g of the finely powdered sample was initially heated to 110°C to remove moisture, and then further heated to 1050°C to determine the loss or gain on ignition (LOI/GOI). For fusion, a precise flux mixture was added, consisting of 0.2445 g La_2O_3, 0.705 g $Li_2B_4O_7$, 0.5505 g Li_2CO_3, and 0.02 g $NaNO_3$, combined with 0.28 g of the sample powder. This mixture was heated in a platinum crucible at 950°C for approximately 5 minutes, until a homogenous molten fluid was formed. The melt was then poured into a mould and rapidly pressed to form a glass disc suitable for XRF analysis**.**

To prepare pressed powder pellets for trace element analysis, 8 g of the finely powdered sample was mixed with 3 g of Hoechst wax ($C_6H_8O_3N_2$) as a binder. The mixture was thoroughly homogenized using a Turbula mixer for 20 minutes to ensure even distribution of the wax. The blended powder was then subjected to a pressure exceeding 395 N/m^2 to form solid, compact pellets suitable for XRF analysis. Whole-rock geochemical analyses were carried out using the Rigaku Primus IV Wavelength Dispersive X-ray Fluorescence spectrometer at the Department of Geology.

3.3.3.2 Normative mineralogy

Whole-rock major element results were used to assist with lithological classification of samples using CIPW norm calculations. The CIPW norm, developed by Cross, Iddings, Pirsson, and Washington (Cross *et al.*, 1902), is a geochemical method that converts a sample's bulk geochemical composition into mineral assemblages making mineralogical classification possible. The composition thus obtained are known as the rock's "normative mineralogical composition" (Buckle *et al.*, 2023; Rollinson, 1993). This approach allows for a standardized and reproducible classification of igneous rocks, especially where direct petrographic interpretation is limited.

The CIPW norm calculations were executed in Microsoft Excel using a Visual Basic macro, following the procedure outlined by Kelsey (1965). The calculated normative mineralogy was then compared to the modal mineralogy determined from visual petrographic estimates, providing a means to cross-validate the classification and identify discrepancies between geochemical predictions and modal mineral content. Differences between the norm and mode are not uncommon. The CIPW norm is based on assumptions of equilibrium crystallization from anhydrous magma, which excludes hydrous minerals like biotite even if they are present in the actual rock (Rollinson, 1993). These discrepancies are particularly notable in altered or metamorphosed samples, where secondary minerals form post-crystallization. By comparing both norm and mode, it was possible to assess the degree of alteration and to refine rock classification.

3.3.3.3 Petrographic analysis

Petrographic analysis was performed on 25 polished thin sections of rock samples (Table 3.3) to visually identify and quantify mineral phases using an Olympus light microscope equipped with a high-resolution SC30 Olympus camera at the Department of Geology, University of the Free State. Microscopic images were captured and archived using the user-friendly PRECiV™ software. This analysis enabled the estimation of modal mineralogy, which is the relative abundances of minerals determined through visual estimates and textural observations. The results were used to cross-validate spectral mineralogical classifications, helping ensure that interpretations based on spectral analysis reflect the true mineral assemblages present in the samples. The classification and nomenclature applied to the RLS rocks in this study follow those established by Streckeisen (1976) and Le Maitre (1984).

In cases where samples showed significant hydrothermal alteration or contained fine-crystalline mineral intergrowths, optical identification under the microscope became challenging. To overcome these challenges, selected samples were further analyzed using a JEOL JSM-6610 Scanning Electron Microscope (SEM) at the Geology Department of the UFS, which operates with an electron beam generated by a tungsten (W) filament. The instrument is equipped for both secondary electron imaging (SEI) and backscattered electron (BSE) imaging, and features spectrometers for Wavelength Dispersive Spectrometry (WDS) (Thermo Fisher MagnaRay) as well as Energy Dispersive Spectrometry (EDS) using a JED-2300 EDS system.

Ten polished thin sections were studied using the SEM. Prior to SEM analysis, polished thin sections were carbon-coated to ensure conductivity and image quality (Table 3.3). Samples

were analysed in batches of five within a sealed vacuum chamber to ensure stable imaging conditions during SEM analysis, conducted at an accelerating voltage of 20 kV and an emission current of 60–100 μA. The SEM was operated using the SEM Main Menu interface, while elemental analysis was performed using EDS analysis. This allowed the performance of point-based chemical analysis, enabling precise identification of minerals that were difficult to distinguish optically. The integration of petrographic and SEM analysis ensured a comprehensive and reliable determination of mineralogy, which is particularly important in altered lithologies or spectrally complex lithologies where spectral responses may be unclear.

Table 3.3: Sample list showing the analyses performed on each sample.

Sample ID	Image	Petrography	SEM	XRF whole rock major elements	XRF trace elements
BH29-NM-01	Image 1	✓		✓	✓
BH29-NM-02		✓	✓	✓	✓
BH29-NM-03		✓	✓	✓	✓
BH29-NM-04		✓	✓	✓	✓
BH29-NM-05		✓	✓	✓	✓
BH29-NM-06		✓	✓	✓	✓
BH29-NM-07		✓	✓	✓	✓
BH29-NM-08	Image 2	✓		✓	✓
BH29-NM-09		✓		✓	✓
BH29-NM-10		✓		✓	✓
BH29-NM-11		✓		✓	✓
BH29-NM-12		✓		✓	✓
BH29-NM-13	Image 3	✓	✓	✓	✓
BH29-NM-14		✓		✓	✓
BH29-NM-15		✓		✓	✓
BH29-NM-16	Image 4	✓		✓	✓
BH29-NM-17		✓	✓	✓	✓
BH29-NM-18		✓		✓	✓
BH29-NM-19		✓		✓	✓
BH29-NM-20		✓	✓	✓	✓
BH29-NM-21		✓		✓	✓
BH29-NM-22		✓		✓	✓
BH29-NM-23		✓		✓	✓
BH29-NM-24		✓	✓	✓	✓
BH29-NM-25		✓		✓	✓

3.4 Data management & storage

Image data were stored in uncompressed and unprocessed RAW formats that are compatible with ArcGIS and ENVI for image analysis.

3.5 Image processing

The workflow in Figure 3.9 outlines the steps that were followed for processing high-resolution RGB and classifying multispectral images, as detailed in the following sections.

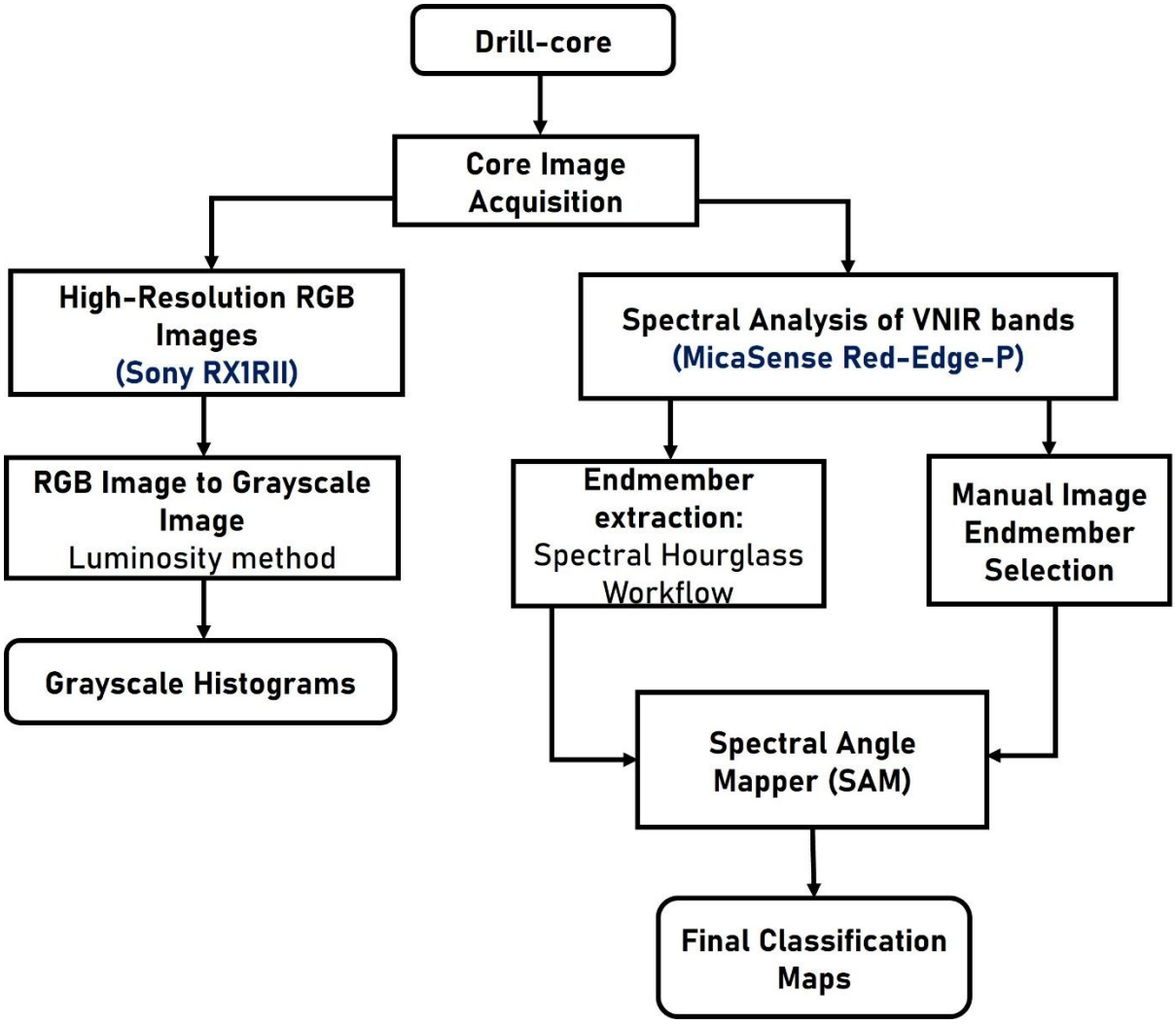

Figure 3.9: Image processing workflow and outputs generated.

3.5.1 High-resolution RGB image processing

High-resolution RGB images were calibrated along with the multispectral images as described under Section 3.2. To evaluate the applicability of grayscale imagery for classifying RLS lithologies, high-resolution RGB images were then converted to grayscale using the luminosity method in RStudio (Appendix G). This method applies weighted values to each colour channel, 0.2989 for red, 0.587 for green, and 0.114 for blue, to reflect the human eye's sensitivity to different colours (Jyothi *et al.*, 2015), R, G, B, are the RGB bands (Equation 1). Green, being the most perceptible, is given the highest weight, followed by red and then blue. This approach produces a more realistic grayscale image that better preserves visual contrast and texture, making it suitable for detailed analysis of geological features.

$$\boldsymbol{Grayscale\ Intensity\ Value} = (\mathbf{0.299} \times \boldsymbol{R}) + (\mathbf{0.587} \times \boldsymbol{G}) + (\mathbf{0.114} \times \boldsymbol{B}) \ldots\ldots \mathbf{(1)}$$

Representative regions of interest (ROIs) ranging from 120 pixels x 356 pixels (approximately 2,4 cm x 7 cm) were selected from Images 2-7 to capture the various rock types. Statistical analysis of the grayscale data was used to assess its effectiveness in distinguishing lithologies, with the image histogram serving as a key tool for visualising pixel intensity distribution across the 0-255 range.

3.5.2 Multispectral image processing

Multispectral images were pre-processed following the steps described under Section 2.4. First calibrated using the CRP in AgiSoft Metashape and processed and analysed in the ArcGIS and ENVI software (MicaSense, 2017; MicaSense, 2024) (Table 3.4). The raw pixel values of multispectral images were converted to spectral radiance values using the CRP in AgiSoft Metashape, which offers a structured workflow for processing MicaSense RE data (Simpson *et al.*, 2024). The process begins with importing the multispectral images and locating the calibration panel. Next, all elements unrelated to the calibration panel were manually masked. Reflectance calibration is then performed using the albedo values specified in Section 3.2 for the five spectral bands. This radiometric calibration step converts raw pixel data into absolute spectral radiance values (measured in $W/m^2/sr/nm$), correcting for sensor sensitivity, dark current, vignetting, gain and exposure settings. It also compensates for variations in lighting and scene conditions.

Subsequent image alignment was carried out in ArcGIS Pro, where bands 1 through 5 were registered to band 6. This was done because band 6, the panchromatic band, has a higher spatial resolution, making it an ideal reference for alignment using four ground control points manually selected for each band. Following alignment, composite images were exported for subsequent processing and analysis in ENVI v6.0. In ENVI, the aligned images underwent further steps, including metadata editing using the MicaSense radiometric calibration guide (MicaSense, 2023), application of the Quick Atmospheric Correction (QUAC), and setting the gain and offset to 1 for each of the five spectral channels. The detailed steps performed in each software are summarized in Table 3.4. This process converts spectral radiance values to spectral reflectance from 0 to 1.0.

Table 3.4: Steps applied in each of the software used.

Agisoft Metashape	ArcGIS (Georeferencing)	ENVI (Image pre-processing)
• Calibration with a Calibration Reflectance Panel	• Aligned Band 1- 5 to Band 6	• Metadata edit (Wavelength, Units, Offsets)
• Increase brightness	• Created a single Composite image with multiple bands	• Quick Atmospheric Correction (QUAC)
	• Image clipped to the core box	• Apply Gains & Offset
	• Clipped image exported in a TIFF file	• Masking

3.6 Spectral classification

The SHW (Figure 3.10) in the ENVI software was adopted to extract pure pixels representative of the spectral responses present in the core. The core chosen for extracting pure pixels was based on the lithological variation hence, more spectral responses can be obtained. In this case, Image 4 was utilised due to the increased lithological variability exhibited, compared to other core images.

The SHW compiles steps to reduce data, extract endmembers, and classify images. Data reduction, including MNF and PPI (described in Section 2.4), isolates spectrally pure pixels dominated by single mineral components within the rock. These are visualised in the n-Dimensional visualizer as spectrally similar clusters, which are refined into class groups, and only those with 10 or more pixels were retained. Using the USGS V7 Beckman Library, class groups were identified with the material identification tool, and an endmember library was created. This library served as reference spectra for image classification of other core images using the SAM method (Section 2.4).

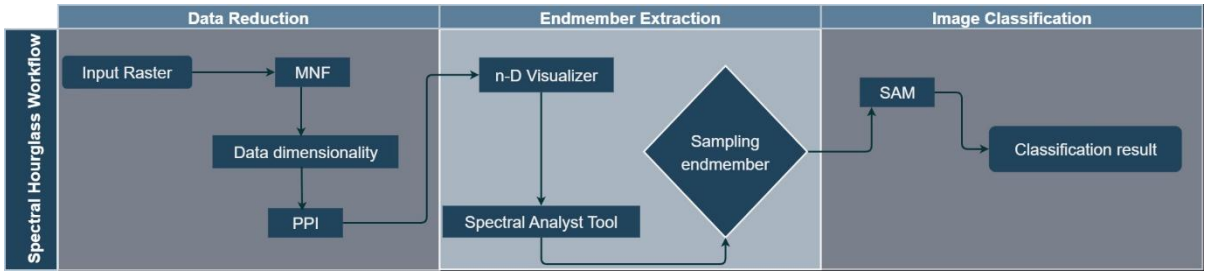

Figure 3.10: The Spectral Hourglass Workflow

Extracted endmembers underwent detailed spectral analysis to assess their similarity to reference mineral spectra from the USGS V7 Beckman Library, as well as to known mineral spectra in other core images. The Pearson Correlation Coefficient (Akoglu, 2018; Markogianni *et al.*, 2020; Novais *et al.*, 2021; Sui *et al.*, 2025) was employed to quantify the degree of linear similarity between spectral profiles, with values close to +1 indicating strong positive correlation and high spectral similarity. The coefficient effectively compares the overall shape of spectra without being influenced by variations in reflectance values. Lastly, the mineral spectra of each image were selected as ROIs to classify the images and assess any improvement in image classification using the SAM technique. Thus, two sets of SAM classification results are presented for Images 1-3 from Test 2, while the extracted spectra from all images were compiled into a Reference Library Spectra of the RLS to classify the additional Images 5-7.

4 Data analysis and results

4.1 Lithology of the imaged zones

Images 1 to 4 captured under Test 2 represent stratigraphic intervals from both the MZ and CZ of the RLS. Images 1 and 2 are from the MZ, and Images 3 and 4 from the UCZ (Table A1 and A2, Appendix A).

- Image 1 (561.26-568.7 m): captures fine-to-medium-crystalline anorthosite exhibiting alternating spotted and mottled textures, with dark gray to brownish-gray colours. The anorthosite based on modal mineralogy shows a gradational contact into medium-crystalline norite, interlayered with thin layers of fine- to medium-crystalline dark gray pyroxenite.
- Image 2 (919.88-927.35 m): cuts through fine- to medium-crystalline gabbronorite ~20 m above the Pyroxenite Marker, ranging in colour from dark brownish-gray to light gray, with variable modal proportions.
- Image 3 (1373.84-1380.88 m): intersects the white-gray to gray GMA in the UCZ characterised by irregularly distributed large pyroxene mottles and occasional small to large leopard spots with a gradational contact.
- Image 4 (1509.58-1517.02 m): captures a UG2 chromitite seam along with pegmatitic pyroxenite of the UG2 hanging wall with thin chromitite layers with irregular contacts at the top of the pegmatitic pyroxenite (pyroxene crystal size greater than 2 mm) transitioning to a normal pyroxenite (crystal size less than 2 mm) (consistent with the findings of Cawthorn (2006)) and norite with clinopyroxene phenocrysts. The drill-core exhibits surface oxidation, evidenced by yellowish-brown to greenish-brown staining attributed to the alteration of iron-bearing minerals.

Additional Images 5 to 7 further illustrate lithological variability across the MZ and UCZ. Image 5 is from the MZ, and Images 6 and 7 are from the UCZ (Table A3, Appendix A).

- Image 5 (576.09-583.45 m): shows a gray to light gray, coarse-crystalline gabbronorite unit, characteristic of the MZ, exhibiting a mineralogical transition from mafic to plagioclase-dominated phases.
- Image 6 (1402.83-1409.62 m): captures a sequence composed of medium-crystalline, green to dark green Bastard Pyroxenite, underlain by a narrow (~2 cm) chromitite

stringer with irregular contacts. This is followed by a white to light gray, medium-crystalline mottled anorthosite, which transitions gradationally into a gray to light gray spotted anorthosite.

- Image 7 (1559.52-1564.72 m): captures a UG1 chromitite seam with thin green, fine-crystalline pyroxenite layers. This sequence is underlain by a gray to light gray mottled anorthosite.

4.2 Geochemistry

4.2.1 Major and trace element data

The chemical composition of the sampled sections is reported in terms of major oxides (wt.%) and trace elements (ppm) and summarised in Appendix C, Table C1 and Table C2, respectively. Loss on ignition (LOI) values across the sampled core sections range from -0.14 to 4.4 wt.%. Notably, samples 1 to 5 (Image 1) and sample 14 (Image 2) exhibit elevated LOI values exceeding 2 wt.%. Samples 20 and 21 (Image 4) display negative LOI values, indicating a gain on ignition, likely caused by oxidation during heating.

Silica (SiO_2) concentrations range widely from 9.34 to 67.81 wt.%, with an average value of 47.96 wt.%. Alumina (Al_2O_3) content varies between 3.33 and 29.36 wt.%, averaging 16.43 wt.%, while calcium oxide (CaO) ranges from 1.33 to 21.45 wt.%, with a mean of 9.12 wt.%. Variation diagrams plotting MgO versus CaO and MgO versus Al_2O_3 for the RLS samples reveal bimodal mixing trends between pure anorthite and orthopyroxene endmembers (Figure 4.1). Potassium oxide (K_2O) concentrations range from 0.04 to 5.06 wt.%, with the highest value observed in sample 24 (Granitoid). Anorthosite contains more than 90% modal plagioclase (Figure 2.5), and the sampled anorthosite lies towards the pure anorthite field of the bimodal mixing trend.

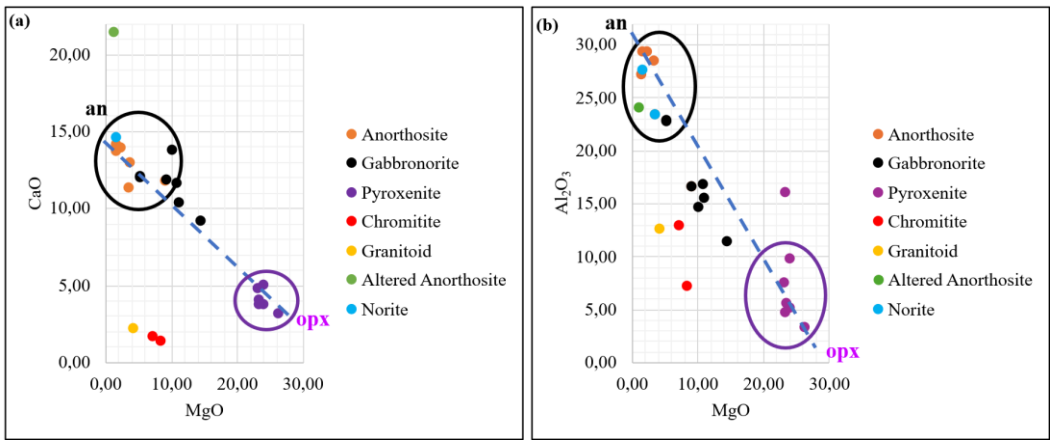

Figure 4.1: Bimodal mixing trends between pure anorthite and orthopyroxene are shown in modal MgO vs. CaO (a) and MgO vs Al_2O_3 (b) variation diagrams. Chromitite and granitoid samples plot off the mixing lines because these lithologies are not dominated by plagioclase and orthopyroxene.

4.2.2 Normative mineralogy

The normative mineral calculations based on the Kelsey (1965) scheme revealed both discrepancies and correlations between the CIPW norms and modal mineralogy, providing a basis for cross-validation of lithological classifications. Discrepancies between CIPW norms and modal mineralogy occur where the amount of normative minerals differs or correlates to that of modal mineralogy, and this is not uncommon in mafic to intermediate igneous rocks (Table 4.1). Nonetheless, the calculated normative minerals align with typical minerals of the RLS and include quartz (generally in minor amounts), orthoclase (alkali feldspar), albite and anorthite (plagioclase feldspars), hypersthene (orthopyroxene), diopside (clinopyroxene), olivine, ilmenite, apatite, and wollastonite. Notably, normative olivine is present in samples 4, 16-18, 20, 22, and 23; sample 5 (altered anorthosite) contains normative wollastonite; and sample 25 (chromitite) exhibits a comparatively higher normative quartz content.

Table 4.1: Normative mineralogy as calculated with the Kelsey (1965) scheme. Note that chromium-rich samples (BH29-NM-19 and BH29-NM-25) are excluded.

Sample no.	Quartz	Corundum	Orthoclase	Albite	Anorthite	Diopside	Hypersthene	Olivine	Ilmenite	Apatite	Wollastonite
1	5,01		2,86	15,51	56,08	8,10	12,01		0,35	0,10	
2	3,63	4,63	2,61	15,98	57,38		15,45		0,25	0,07	
3	3,02		2,97	18,65	64,51	4,11	6,38		0,27	0,10	
4			0,92	15,35	7,22	9,81	41,02	25,18	0,39	0,12	
5	3,62		1,10	2,65	66,94	13,51			0,10	0,03	12,06
6	3,41		2,31	11,06	39,10	16,82	26,80		0,46	0,07	
7	2,79		1,47	8,20	35,35	27,49	24,26		0,43	0,05	
8	0,20		1,60	11,79	38,94	15,19	31,88		0,38	0,05	
9	4,10		2,44	16,03	53,77	5,63	17,68		0,29	0,05	
10	3,01		2,45	11,03	35,59	13,14	34,34		0,39	0,07	
11	1,60		1,88	8,03	26,28	15,82	45,92		0,44	0,06	
12	6,12		2,44	13,01	55,23	4,23	18,56		0,35	0,05	
13	5,05	1,31	2,00	10,84	72,94		7,73		0,10	0,02	
14	1,13		2,31	14,75	37,31	17,94	26,08		0,44	0,07	
15	3,62	1,12	1,09	14,58	70,17		9,27		0,13	0,03	
16			0,98	1,96	12,84	4,99	74,20	4,47	0,43	0,13	
17			1,81	2,19	11,35	7,37	75,65	1,16	0,40	0,08	
18			0,69	3,51	25,75	0,26	41,12	28,27	0,37	0,03	
20		8,67	0,41	2,80	18,39		44,95	24,28	0,48	0,02	
21	8,89		2,15	7,80	71,56	1,99	7,46		0,14	0,02	
22			0,38	5,11	17,70	5,07	63,75	7,70	0,29	0,01	
23			0,32	3,27	7,36	6,69	74,45	7,52	0,37	0,04	
24	32,66	2,45	30,87	5,34	10,37		16,71		1,35	0,26	

Figure 4.2 presents a comparison of strontium (Sr) concentrations across the different lithologies. As expected, modal anorthosite displays the highest Sr values, while altered anorthosite shows notably lower concentrations. Norite exhibits the second-highest Sr levels. Pyroxenite samples have notably low Sr content, except for a high-value outlier in pegmatitic pyroxenite. Gabbronorite shows moderate Sr concentrations with one outlier on the higher end, while granitoid samples also fall within the moderate range. Sr concentration is therefore a good proxy for plagioclase abundance.

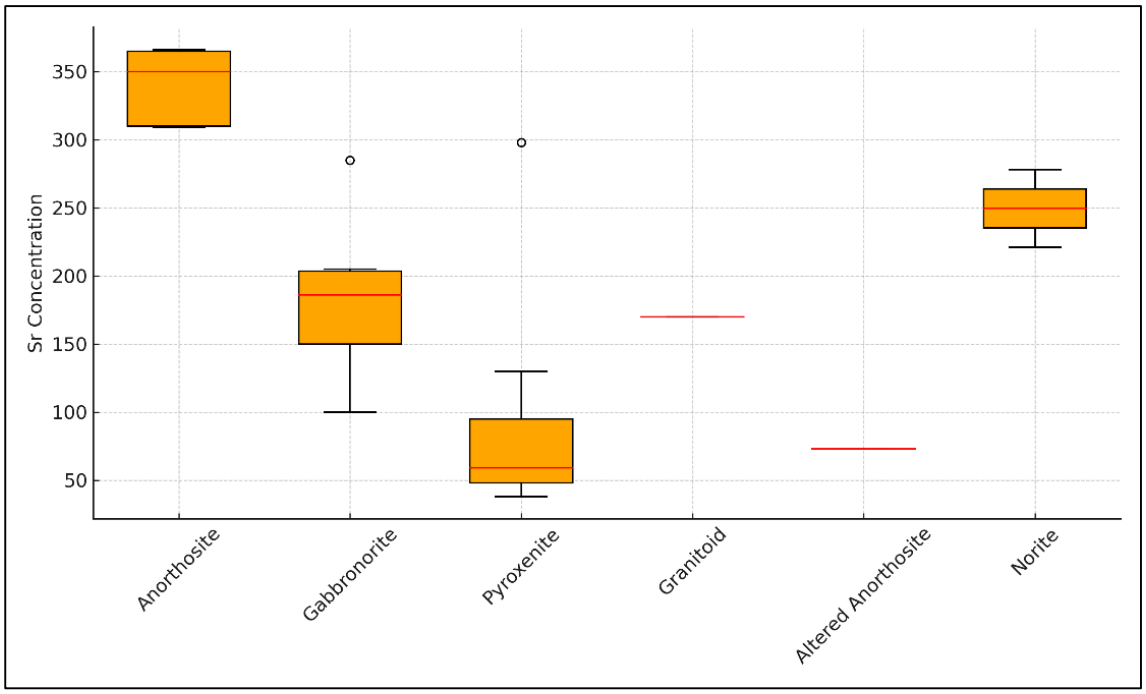

Figure 4.2: Box and Whisker Plot of lithologies with strontium concentrations

4.3 Petrography

Petrographic descriptions are based on thin sections analysed under a microscope to determine the rocks' mineralogy and texture as described by Nesse (2009). Mineral abundances for the different lithologies were determined through visual estimation (Table 4.2). Orthopyroxene and plagioclase are the dominant minerals present in these rocks. Clinopyroxene is rare in some lithologies, and where present, it occurs as oikocrysts enclosing orthopyroxene or as exsolution lamellae within orthopyroxene and interstitially between larger cumulus plagioclase minerals. Petrographic descriptions and SEM analysis confirmed the presence of these minerals in samples that were not resolved by optical microscopy (Appendix D). Other rare minerals include mica, quartz, and sulphides.

Table 4.2: Summary of major lithologies and mineralogy of the Rustenburg Layered Suite (BH7929).

Lithology	**Samples**	**Petrographic description**
Leucogabbronorite	8, 9, 12	Cumulus plagioclase (~ 70-83%), anhedral-subhedral cpx (~ 5-7%) and opx (~ 10- 20%); biotite (0-2%) and quartz (~ 1%), intergranular-subophitic texture.
Melagabbronorite	22	Cumulus opx (~ 70%), anhedral-subhedral cpx (~ 10%), elongated plagioclase (~ 15%); biotite (~ 1%), opaque minerals (~1%), and quartz (~ 3%), subophitic-intergranular texture.
Gabbronorite	6, 7, 10, 11	Cumulus plagioclase (~ 40-50%), anhedral cpx (~ 10-30%), and opx (~ 15-45%); opaque (~0-2%), biotite (~ 3%), and quartz (~ 3%), intergranular texture.
Anorthosite	2, 3, 4, 13, 14, 15	Elongated plagioclase (~ 90-100%), anhedral cpx (~ 2- 4%), subhedral opx (~ 3-5%), and quartz (~ 2%), ophitic-subophitic texture.
Highly altered Anorthosite	5	Completely altered calcium-rich plagioclase, the presence of quartz and epidote was identified through SEM.
Leuconorite	1, 21	Cumulus plagioclase (~ 75-85%), anhedral cpx (<5-7%), subhedral opx (~ 10-20%), opaque (~1%), and quartz (< 3%), subophitic-poikilitic texture.
Orthopyroxenite	16, 18, 23	Cumulus rounded-bladed opx (> 90%), oikocrysts of plagioclase (<5%), and of cpx (~ 5%); with intergranular biotite (~ 3-5%), chromite (~1%), and quartz (~ 1%), poikilitic texture.
Chromite-bearing Pyroxenite	20	Elongated, oikocrysts of plagioclase (~ 5%) hosting coarse-crystalline rounded-bladed opx (~ 35%) and cpx (~40%); biotite (~ 4%), chromite (~15%), and quartz (~ 1%), poikilitic texture.

Pegmatitic Pyroxenite	17	Large oikocrysts of plagioclase (3%) hosting >5 mm crystalline rounded-subhedral opx (>90%) and cpx (~ 1%); biotite (~ 2%), opaque (~3%), and quartz (~ 1%), in interstices of pyroxenes, poikilitic texture.
Chromitite	19, 25	Rounded-subhedral chromite (~70-90%) hosted in opx (~ 5-15%) and plagioclase (<5%); biotite (~ 2%), intergranular- poikilitic texture.
Granitoid	24	Minor alteration, biotite (5%), quartz (75%), opx (4%), cpx (1%), altered plagioclase, and orthoclase (15%).
	All samples have a degree of alteration and microfracturing.	**Alteration:** Hydrothermal alteration in the samples is marked by extensive microfracturing, facilitating fluid infiltration and mineral replacement. This includes the saussuritization of calcium-rich plagioclase into epidote and albite, as well as the uralitization of orthopyroxene and clinopyroxene to actinolite. Alteration intensity varies from approximately 15 - 90% in affected samples.

The anorthosites are predominantly composed of cumulus plagioclase blades exhibiting twin lamellae (Figure 4.3a), locally altered to varying degrees. Minor amounts of anhedral orthopyroxene, commonly displaying exsolution lamellae, and altered clinopyroxene occupy intergranular spaces. These phases collectively define a spotted anorthosite with an intergranular texture and a mottled anorthosite exhibiting ophitic to sub-ophitic textures. Quartz is present in trace amounts.

Gabbronorite consists of cumulus plagioclase blades with anhedral orthopyroxene and clinopyroxene forming an intergranular texture with minor opaque minerals as inclusions and irregular biotite crystals (Figure 4.3b and c). Norite from the MZ is composed predominantly of cumulus plagioclase with minor interstitial orthopyroxene, which contains rounded plagioclase inclusions. Clinopyroxene occurs between crystals, forming a characteristic intergranular texture. In contrast, norite from the CZ consists of bladed to rounded and

subrounded plagioclase enclosed within anhedral orthopyroxene, resulting in a sub-ophitic to poikilitic texture (Figure 4.3d).

In pegmatitic pyroxenite, large oikocryst plagioclase crystals enclose coarse-crystalline orthopyroxene, clinopyroxene, and minor opaque chromite and biotite (Figure 4.3e). Normal pyroxenites exhibit interstitial plagioclase between cumulus pyroxenes (Figure 4.3f). The granitoid is moderately altered and characterised by elevated amounts of quartz, with lower concentrations of K-feldspar and plagioclase (Figure 4.4a). Chromitite layers contain chromite hosted within orthopyroxene crystals, often accompanied by intergranular biotite (Figure 4.4b and c).

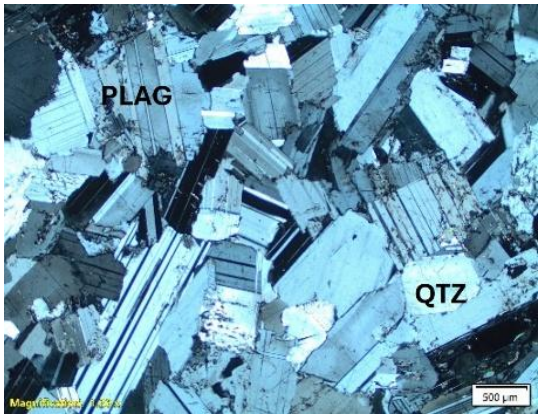

(a) Anorthosite from the depth between 565,3 - 565,34 m.

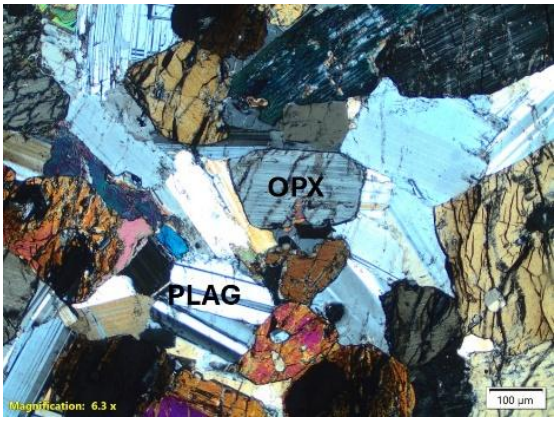

(b) Gabbronorite from the depth between 924,49-924,59 m.

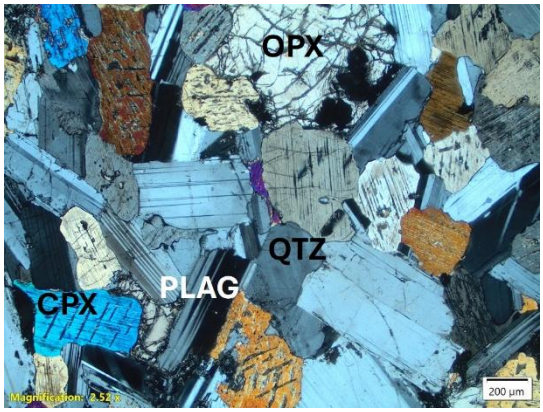

(c) Leucogabbronorite from the depth between 568,56 - 568,66 m.

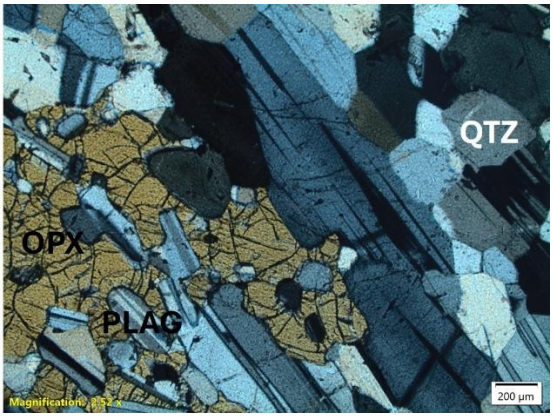

(d) Norite from the depth between 1515,26 - 1515,31.

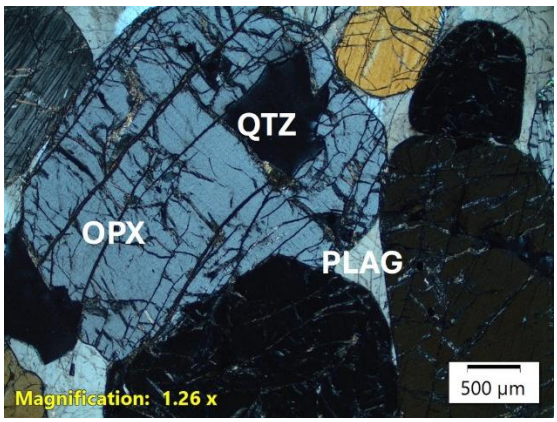

(e) Pegmatitic pyroxenite from the depth between 1510,42 - 1510,60 m.

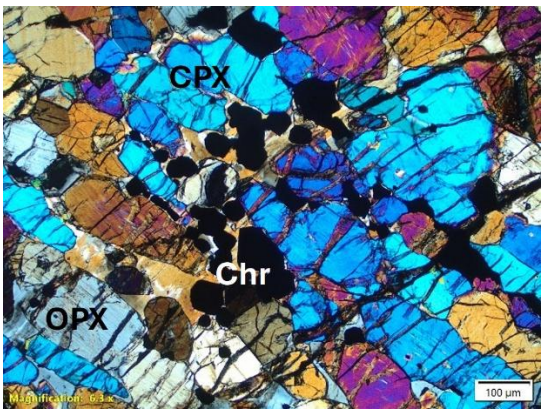

(f) Pyroxenite from the depth between 1512,80 - 1513,02 m.

Figure 4.3: Photomicrographs of representative lithologies in cross-polarised, transmitted light, of anorthosite (a), gabbronorite (b), leucogabbronorite (c), norite (d), pegmatitic pyroxenite (e), and pyroxenite (f).

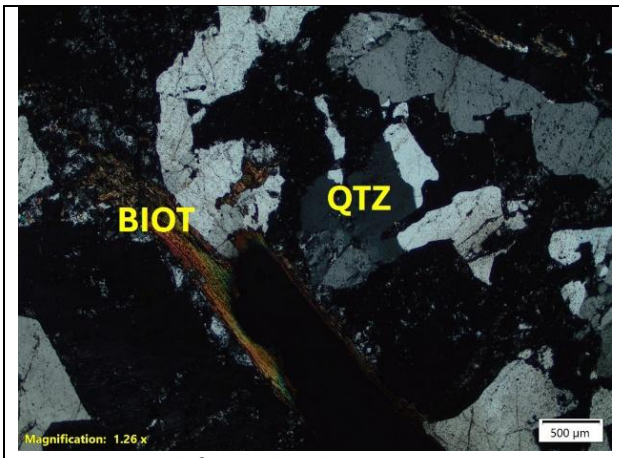

(a) Granitoid from the depth between 1516,42 - 1516,56 m.

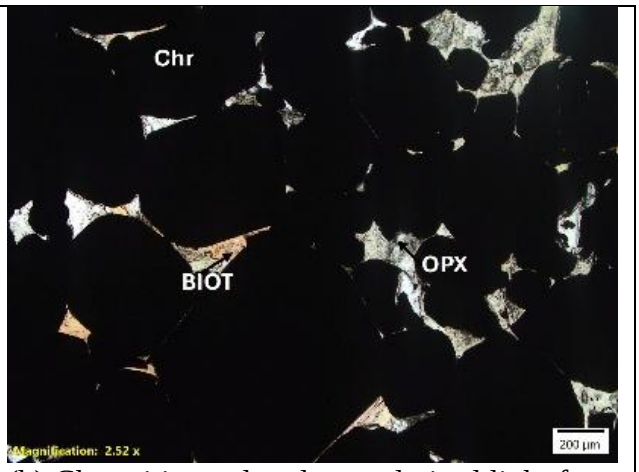

(b) Chromitite under plane polarised light from the depth between 1516,77 - 1516,85 m.

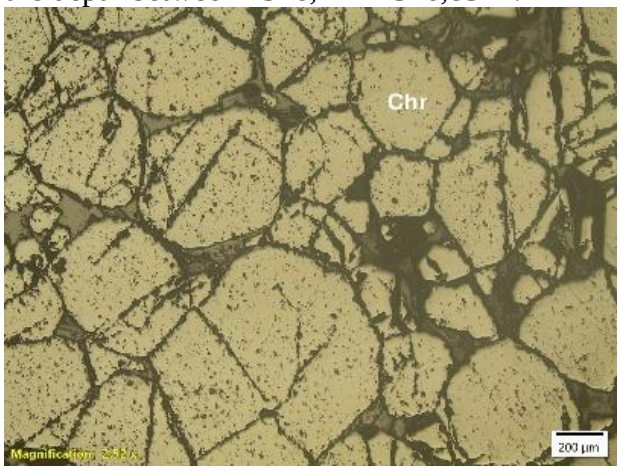

(c) Chromitite under plane polarised, reflected light from the depth between 1516,77 - 1516,85 m.

Figure 4.4: Photomicrographs in cross-polarised light of granitoid (a) and chromitite layers (b) and chromitite in reflected light (c).

Of the 25 samples analysed, most from Images 1 and 3 display extensive hydrothermal alteration. Alteration occurs to varying degrees in all samples, manifesting as fine-crystalline mineral intergrowths that hinder optical identification; consequently, alteration products were characterised using SEM analysis by comparing SEM-derived compositions with standardized mineral descriptions in the Handbook of Mineralogy (Anthony *et al.*, 2022). The alteration is closely linked to micro-fracturing, which facilitated fluid infiltration and subsequent

mineralogical changes such as saussuritization of calcium-rich plagioclase into epidote and albite (Figure 4.5a, b, c), as well as the uralitization of orthopyroxene and clinopyroxene to actinolite pseudomorphs (Figure 4.5d).

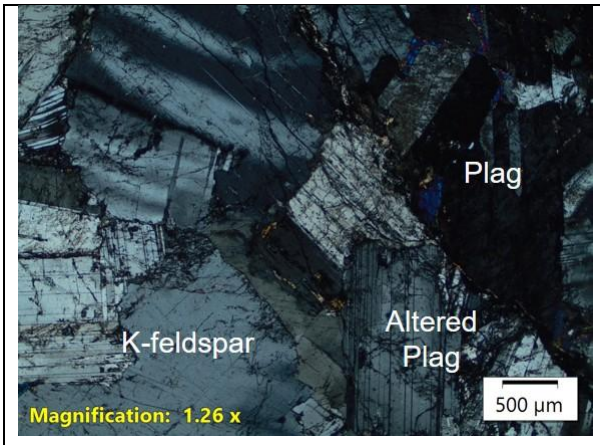

(a) Anorthosite from the depth between 563,27 - 563,40 m (BH29-NM-02).

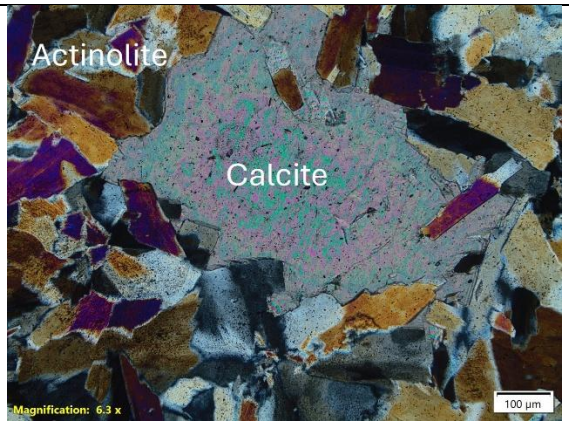

(b) Anorthosite from the depth between 563,96 - 564,07 m (BH29-NM-03).

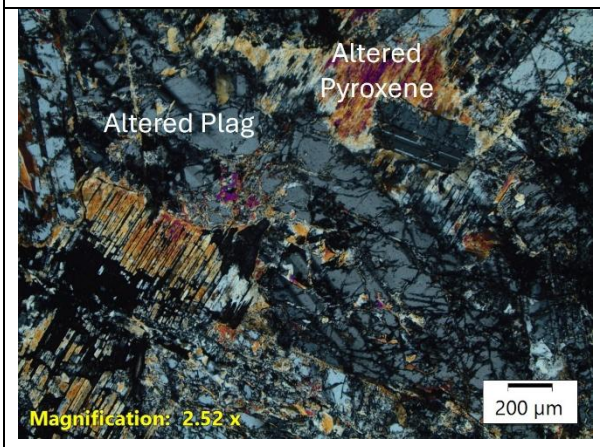

(c) Anorthosite from the depth between 563,96 - 564,07 m (BH29-NM-03).

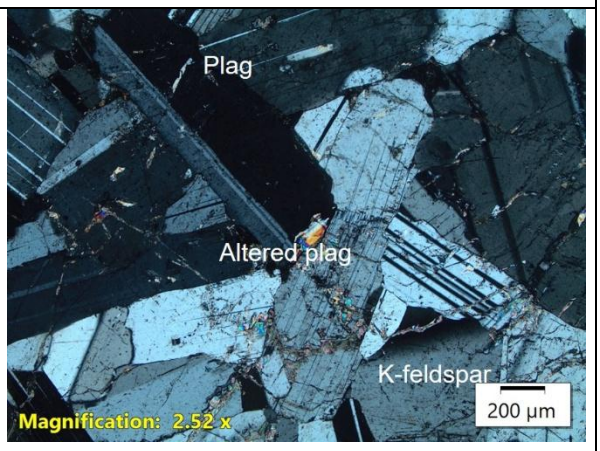

(d) Anorthosite from the depth between 1374,7 - 1374,86 m (BH29-NM-13).

Figure 4.5: Photomicrographs of hydrothermal alteration in cross-polarised light in anorthosites in the MZ (a), (b), and (c) and an anorthosite in the CZ (d).

4.4 Grayscale image analysis

The high-resolution RGB training Images 2-4 (Figure 4.6) and validation Images 5-7 (Figure 4.7) were used to assess the grayscale approach in lithological classification of the major rock types of the RLS rocks, gabbronorite, anorthosite, pyroxenite, and chromitite. Highly altered core sections were excluded from analysis, as they obscure the primary lithological characteristics; Image 1 contains extensively altered zones and was therefore omitted.

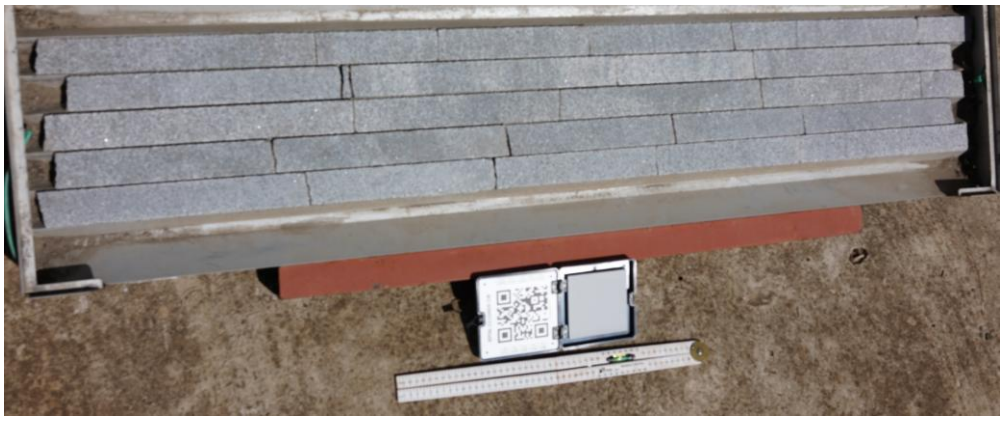

(a) 919.88-927.35 m (Image 2)

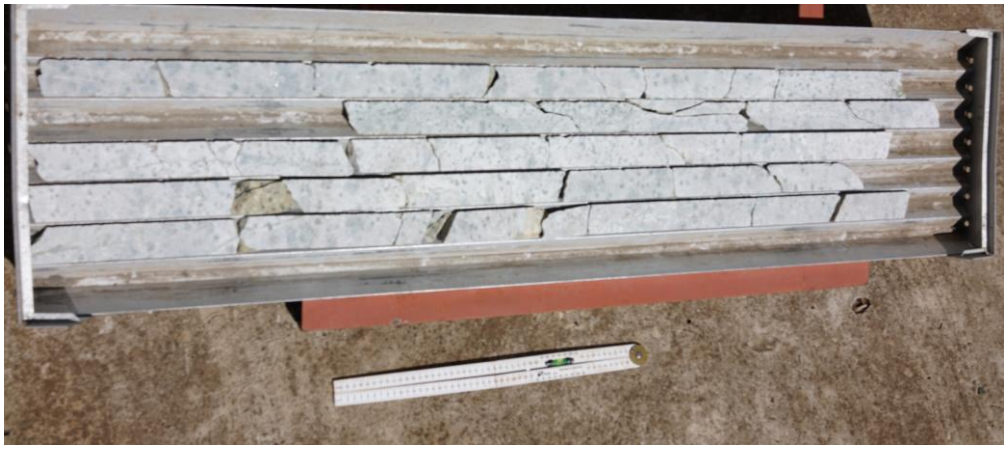

(b) 1373.84-1380.88 m (Image 3)

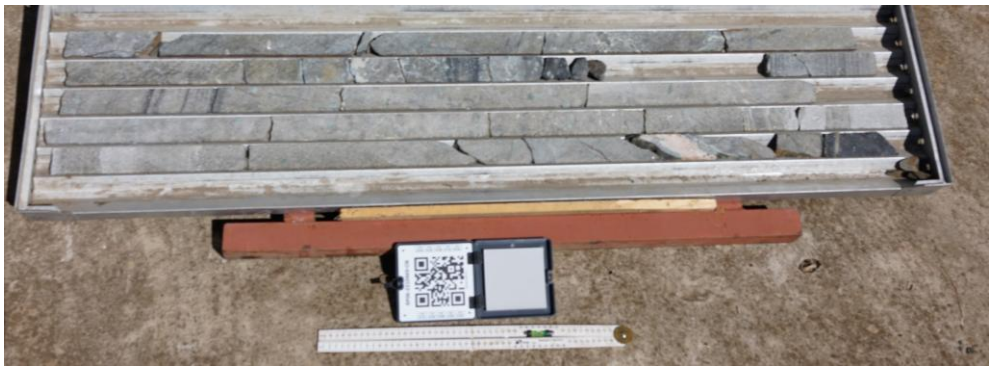

(c) 1509.58-1517.02 m (Image 4)

Figure 4.6: Calibrated high-resolution RGB training Images 2 (919.88 m to 927.35 m) (a), Images 3 (1373.84 m to 1380.88 m) (b), and Images 4 (1509.58 m to 1517.02 m) (c).

(a) 576.09 m - 583.45 m (Image 5)

(c) 1402.83 m -1409.62 m (Image 6)

(e) 1559.52 m -1564.72 m (Image 7)

Figure 4.7: Calibrated high-resolution RGB validating Images 5 (576.09 m to 583.45 m) (a), Images 6 (1402.83 m to 1409.62 m) (b), and Images 7 (1559.52 m to 1564.72 m) (c).

Representative ROIs outlining different lithologies, ranging from 120 pixels x 356 pixels (approximately 2 cm x 7 cm), were selected from both the training Images 2-4 (Figure 4.8) and validating Images 5-7 (Figure 4.9). The ROIs in the training images were used to capture and distinguish lithologies of known composition, serving as reference data for grayscale statistical analysis. The validation images were then used to test whether the grayscale statistics from the training data could reliably identify comparable lithologies in the validation images.

Image 2 (919.88 to 927.35 m)	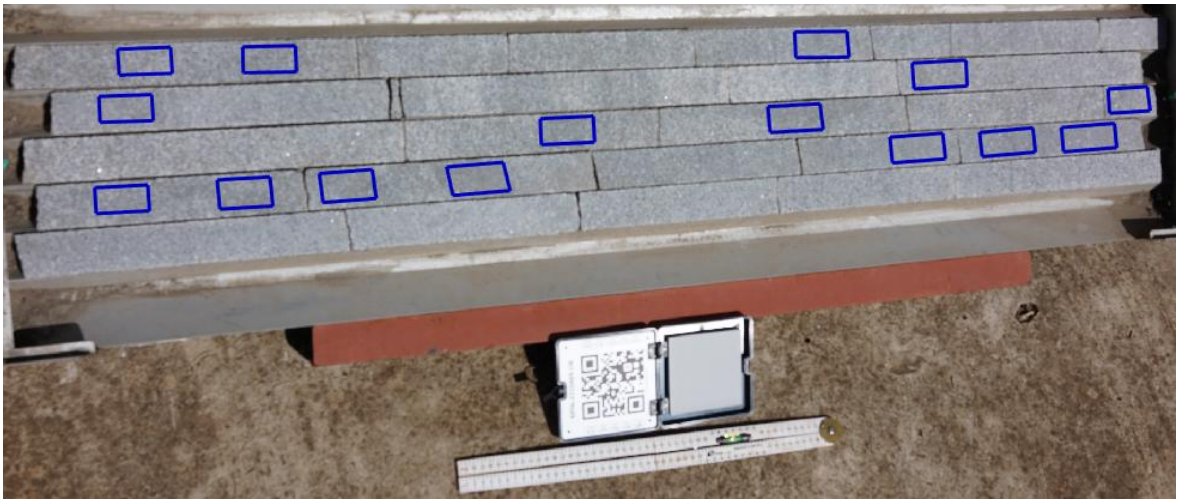
Image 3 (1373.84 to 1380.88 m)	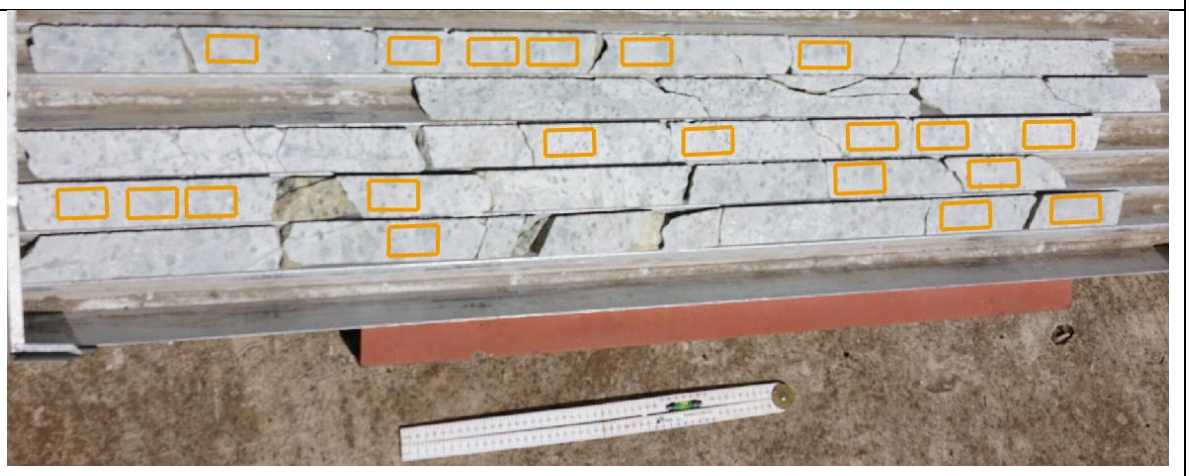
Image 4 (1509.58 to 1517.02 m)	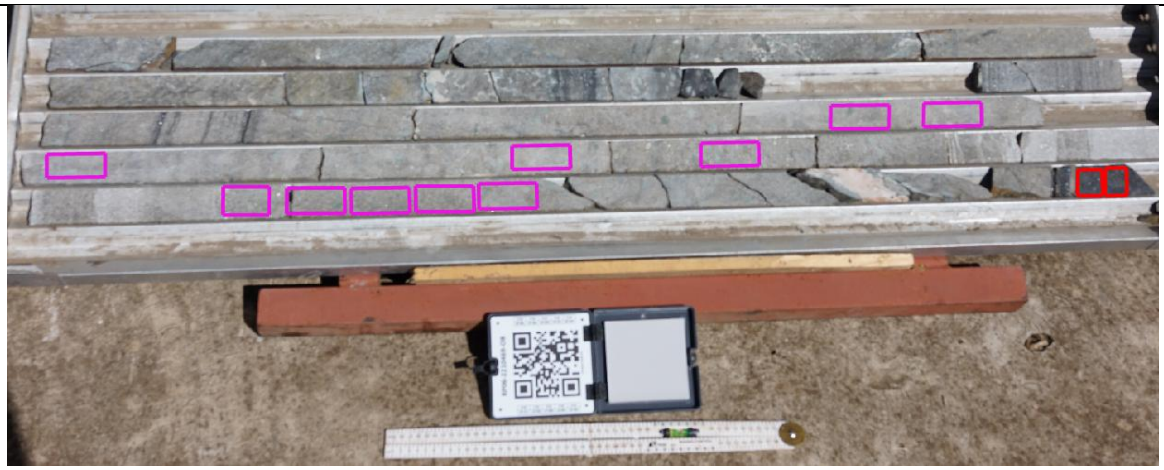

Figure 4.8: Selected Region of Interests for the different rock types: blue (gabbronorite), orange (mottled anorthosite), red (chromitite), and pink (pyroxenite).

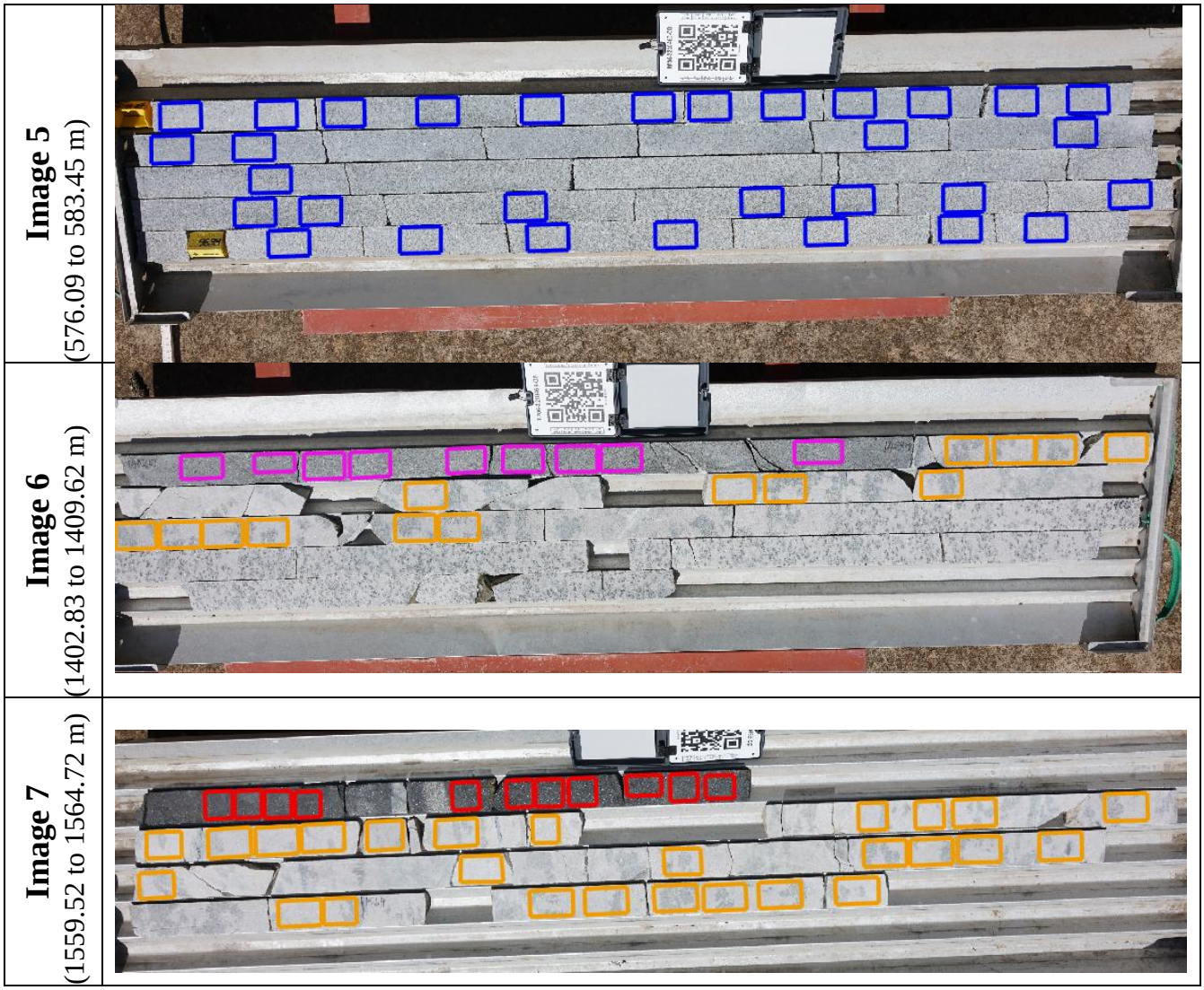

Figure 4.9: Selected Regions of Interest for the different rock types: blue (gabbronorite), orange (mottled anorthosite), red (chromitite), and pink (pyroxenite).

4.4.1 Grayscale pixel intensity histograms

The histograms for chromitite and anorthosite (Figure 4.10), gabbronorite and pyroxenite (Figure 4.11) display the pixel intensity distributions (0-255) for representative lithological regions from training and validation image data. All statistical data of pixel intensity distribution in DN for the representative regions are presented in Appendix E and Appendix F, where the regions shown in bold blue indicate those selected for histogram illustration.

Lighter-coloured lithologies with higher reflectance typically show pixel intensity histograms concentrated toward the higher values of the grayscale range (negatively skewed), whereas darker lithologies show peaks concentrated at lower intensity values (positively skewed). These variations in the histogram shape and distribution serve as effective indicators for distinguishing lithologies based on visual and underlying compositional differences.

Chromitite exhibits a positively skewed pixel intensity histogram, with the majority of pixel intensity values concentrated toward the lower values of the grayscale range and a decrease of lighter pixels towards the right of the histogram, highlighting the limited presence of bright pixels within the sample. However, the primary distinction between the training and validation chromitite histograms lies in the distribution, where the validation chromitite exhibits a broader intensity range, although the pixel values remain predominantly concentrated in the lower grayscale region, consistent with the training chromitite.

Anorthosite is characterized by a prominent peak concentrated toward the higher end of the grayscale spectrum in both the training and validation datasets. The subtle variation between the two lies in the skewness of their pixel intensity distributions, with the training anorthosite exhibiting a positive skew and the validation anorthosite showing a negative skew.

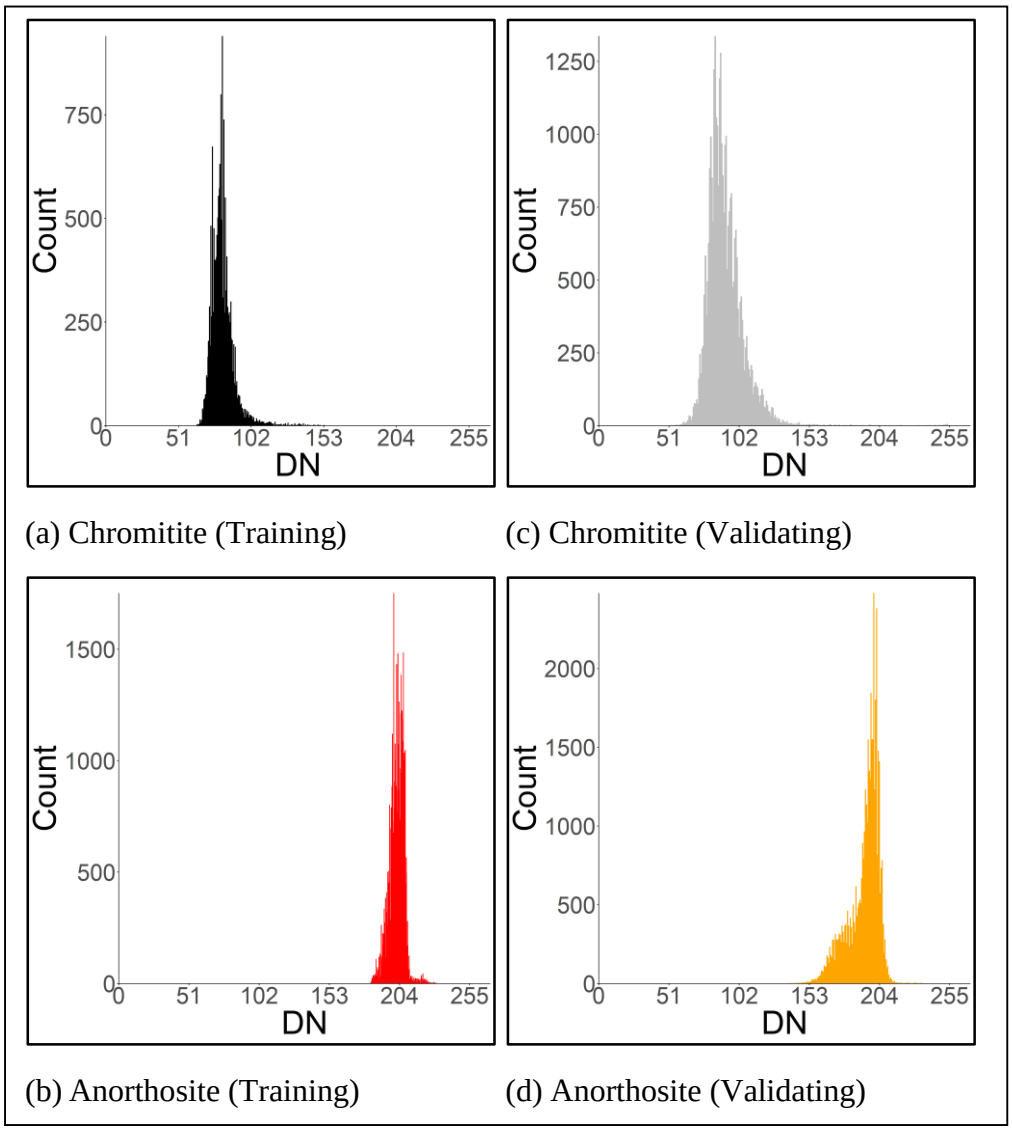

Figure 4.10: Histograms of pixel intensity distribution from training chromitite (a), training anorthosite (b), validating chromitite (c), and validating anorthosite (d).

The training pyroxenite and gabbronorite histograms exhibit peaks toward the higher end of the grayscale range, reflecting a predominance of lighter pixel values, with relatively narrow distributions slightly skewed toward higher intensities. In contrast, the validation pyroxenite and gabbronorite histograms display broader intensity ranges and a slight skew toward lower values.

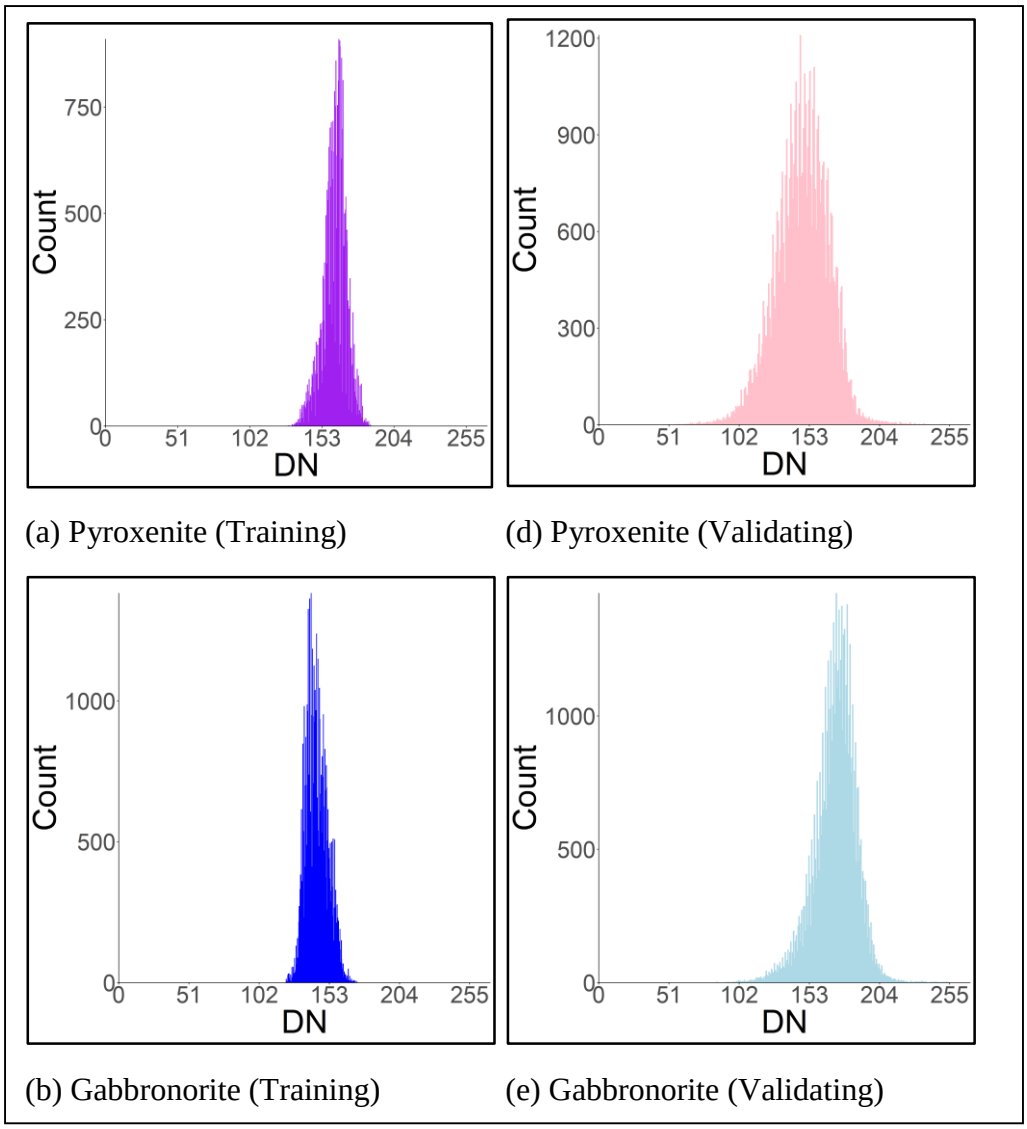

Figure 4.11: Histograms of pixel intensity distribution from training pyroxenite (a), training gabbronorite (b), validating pyroxenite (c), and validating gabbronorite (d).

4.4.2 Grayscale pixel intensity distribution histogram statistics

Appendix E and Appendix F present the summary statistics of the pixel intensity distribution histograms for the training and validation datasets, respectively, including the median, standard deviation (SD), and variance. To assess and compare the distributions, only the median and SD were considered for chromitite, anorthosite, pyroxenite, and gabbronorite (Figure 4.12). Across

all lithologies, the validation data exhibit higher SD values than the corresponding training data. The median values of the training data differ slightly from those of the validation data for most lithologies. However, for chromitite, where only two training regions were used, a higher median difference is observed between the training and validation datasets, suggesting greater variability and potential underrepresentation in the training data.

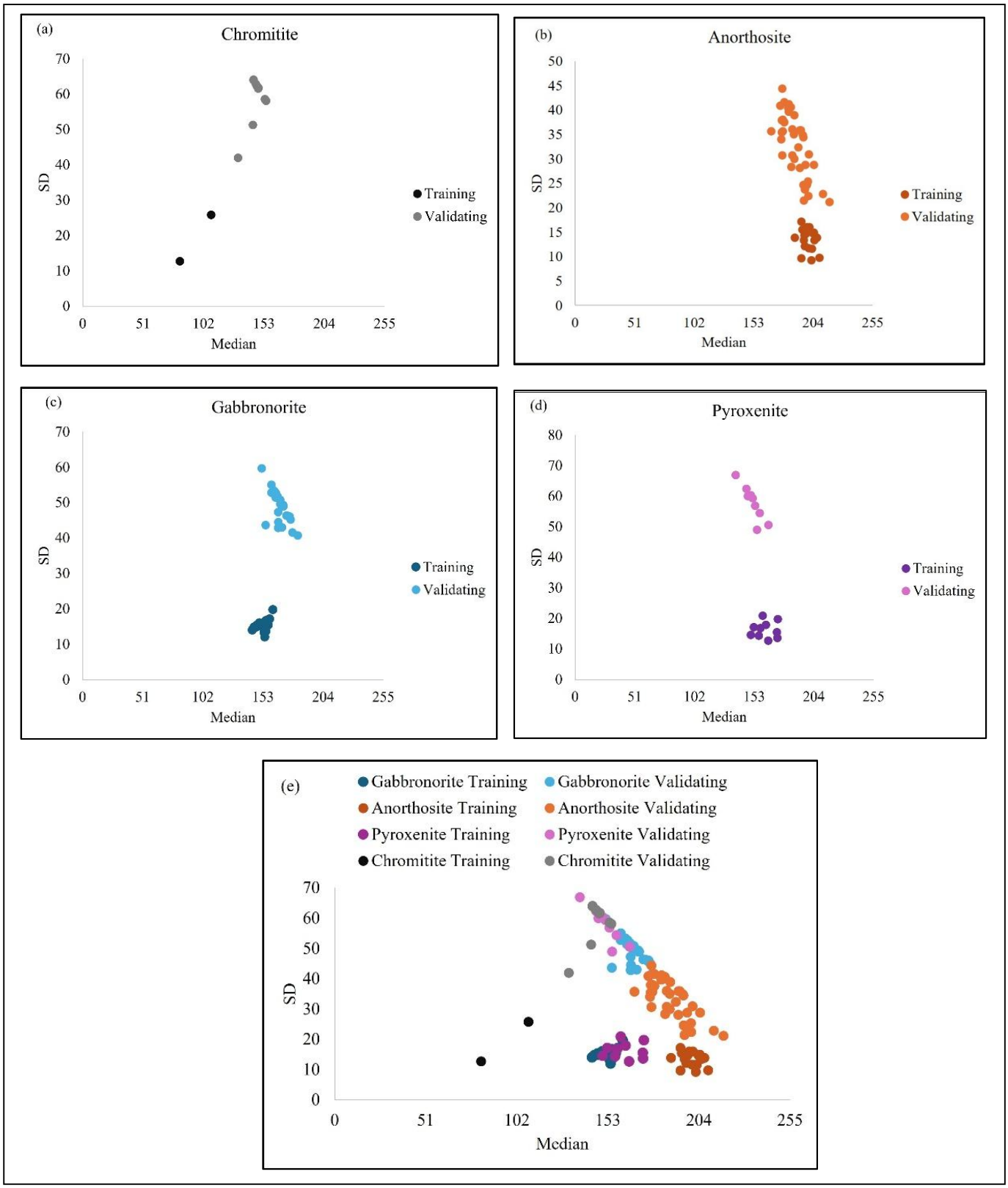

Figure 4.12: Distribution of the DN median and DN standard deviation of the training and validating chromitite (a), anorthosite (b), gabbronorite (c), pyroxenite (d), and both data of all lithologies in a single plot (e).

4.4.3 Grayscale classification accuracy assessment

The statistical measures, the median and the median range, derived from the training data of the four major rock types, were used to evaluate whether regions from the validation dataset could be identified or classified as those specific rock types based on the median values of the training data. The classification ranges for the test data were established using the minimum and maximum median values of the training datasets for pyroxenite, anorthosite, chromitite, and gabbronorite. These ranges were then used to categorize the results into pyroxenite, gabbronorite, gabbronorite/pyroxenite, chromitite, anorthosite, or unclassified groups (Table 4.3)

Table 4.3: Training medians and assigned training ranges

Lithology	Training Median		Assigned median ranges for validation	
	Minimum	Maximum	Minimum	Maximum
Pyroxenite	150,07	173,12	161,23	173,12
Gabbronorite/ Pyroxenite	-	-	150,07	161,23
Anorthosite	188,23	209,06	>188,23	
Gabbronorite	144,01	161,23	144,01	150,07
Chromitite	81,94	108,49	<108,49	
Unclassified	-		Out of range	

Of the 26 validation regions corresponding to gabbronorite, none were classified as gabbronorite when using the assigned testing range of 144.01-150.07. Instead, 80.77% were categorized as unclassified, while 19.23% were identified as either gabbronorite or pyroxenite (Table 4.4). For the 39 anorthosite validation regions, when tested with a median threshold greater than 188.23, 43.59% were correctly classified as anorthosite, whereas 56.41% remained unclassified. Among the nine pyroxenite validation regions, 11.11% were classified as pyroxenite, 44.44% as either gabbronorite or pyroxenite, and 44.44% as unclassified when the testing range of 150.07-161.23 was applied. Lastly, for the 11 chromitite validation regions, none were classified as chromitite when tested with a median value below 108.49; consequently, 100% were designated as unclassified.

Table 4.4: Grayscale Classification Accuracy

Lithology	Classified	Unclassified	Overlap (Gabbronorite/Pyroxenite)
	(%)		
Gabbronorite	0,00	80,77	19,23
Anorthosite	43,59	56,41	-
Chromitite	0,00	100,00	-
Pyroxenite	11,11	44,44	44,44

4.5 Spectral analysis using spectral hourglass workflow

Six endmember spectra (Figure 4.13a) with more than 10 pixels each were selected from the ten classes extracted using the SHW method. These spectra were visually compared with the USGS V.7 Beckman reference spectral library (Figure 4.13b), focusing on major minerals typical of the BC, to aid in identifying the extracted mineral spectra based on subtle spectral variations within the VNIR and their location in the core. The reference spectra used are enstatite for orthopyroxene, augite for clinopyroxene, labradorite for plagioclase, chromite, and hematite (better visualisation of the classes: Appendix H). The drill-core exhibits surface oxidation, evidenced by yellowish-brown to greenish-brown staining attributed to the alteration of iron-bearing minerals. As a result, the Fe-staining spectrum is combined with two enstatite spectra and displayed using a similar colour in the classification results, unless stated otherwise.

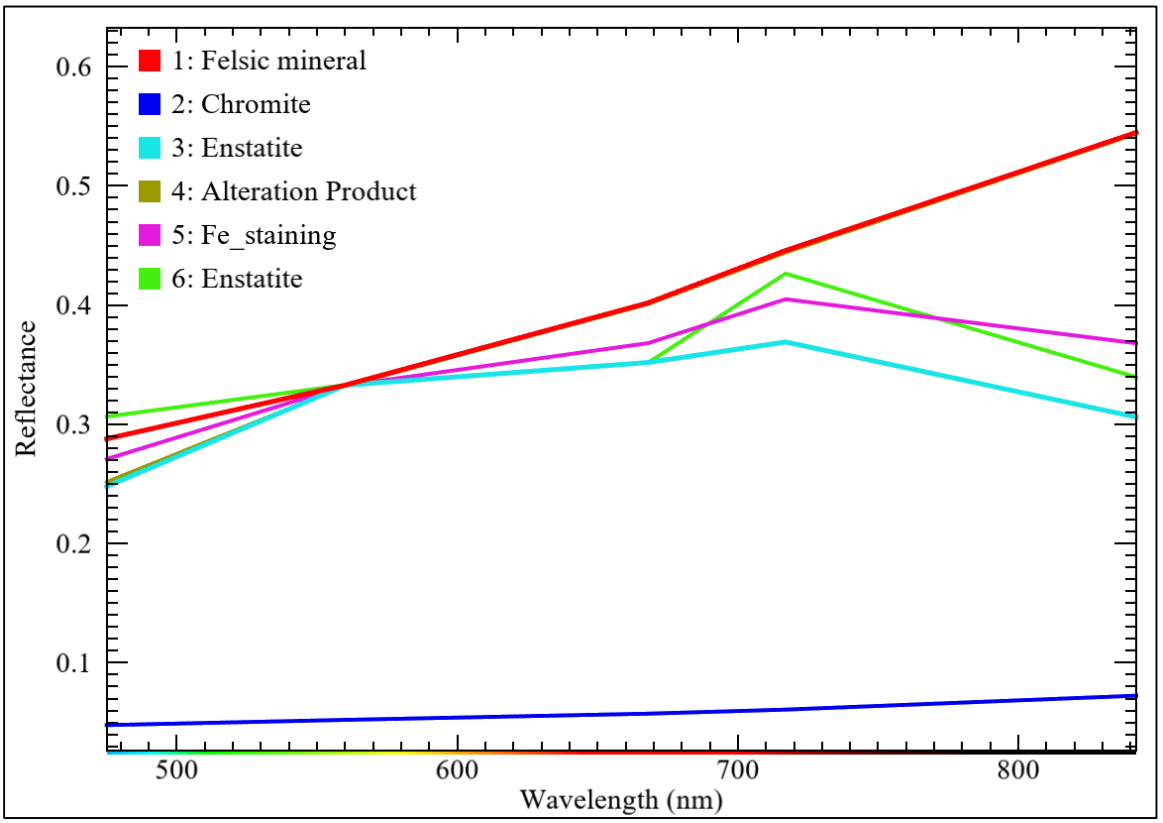

(a)

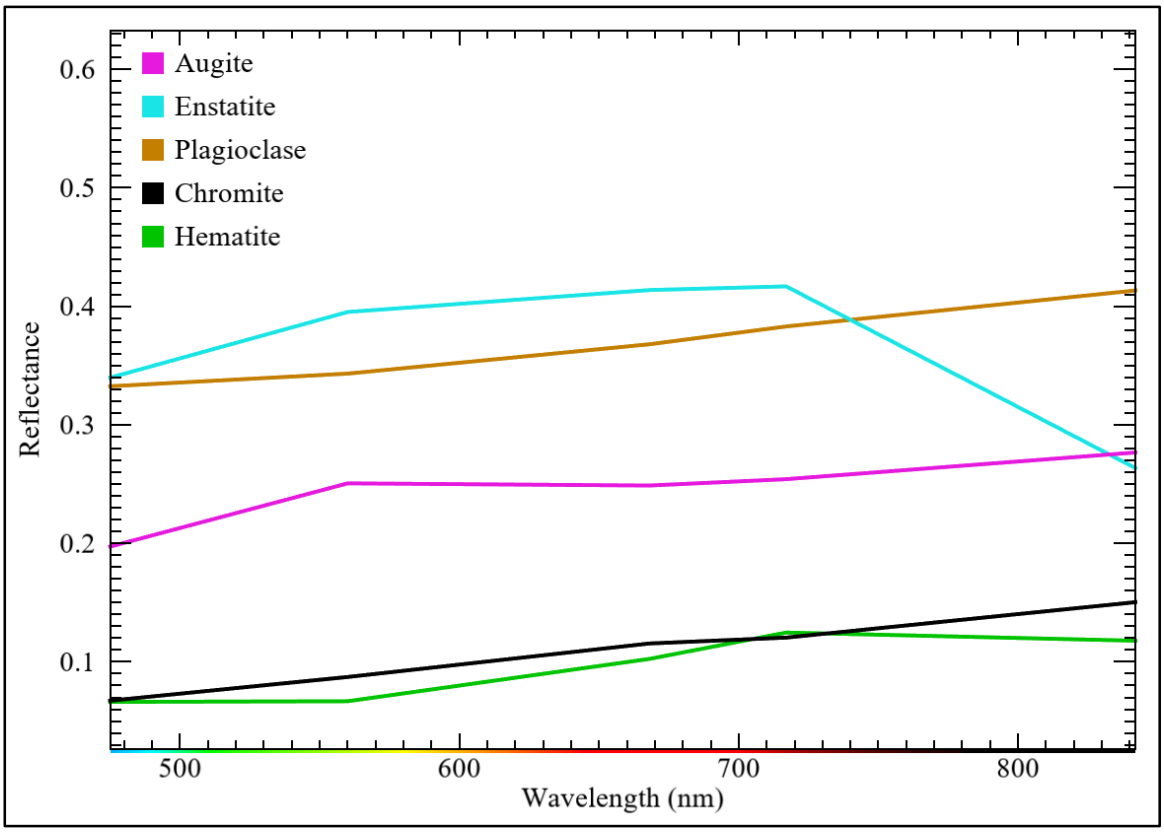

(b)

Figure 4.13: Comparison of the extracted endmembers (a) with the major minerals of the Bushveld Complex from the USGS V7 Beckman mineral library (b).

The reflectance curves of Classes 1 and 4, along with their spatial distribution in Image 4, suggest the presence of felsic minerals consistent with plagioclase spectra, as well as alteration minerals associated with granitoid intrusion. These classes lack distinct absorption features but show a notable difference around 475 nm, corresponding to the blue region of the spectrum (Appendix H). Class 2 lacks distinct absorption features but is characterised by low reflectance values, consistent with the spectral signature of chromite. Classes 3, 5, and 6 display peak reflectance at 717 nm, followed by a sharp decline towards 842 nm within the NIR region, closely corresponding to the diagnostic spectral signature of enstatite (Appendix H). The spectral variation observed among the enstatite classes is expected and can be attributed to Fe-staining noted in certain sections of the pyroxenite. However, the extracted spectra associated with Fe-staining more closely resemble enstatite than hematite, suggesting that the iron alteration modifies the enstatite signature without fully resembling the spectral characteristics of hematite, and is identified as enstatite. This iron enrichment can alter the spectral response, particularly in the NIR region, leading to subtle shifts in absorption features and overall reflectance profiles.

The extracted endmembers served as reference spectra for building a custom spectral library tailored to the RLS rocks, which was then used to classify all captured sections under Test 2. It was noted that the extracted felsic mineral spectra did not correspond to the expected locations of plagioclase in the core, and many areas containing plagioclase were included among the unclassified pixels reported by the SHW method. To address this, representative plagioclase spectra were manually selected directly from the image and incorporated into the custom reference library (Figure 4.14) to improve classification accuracy.

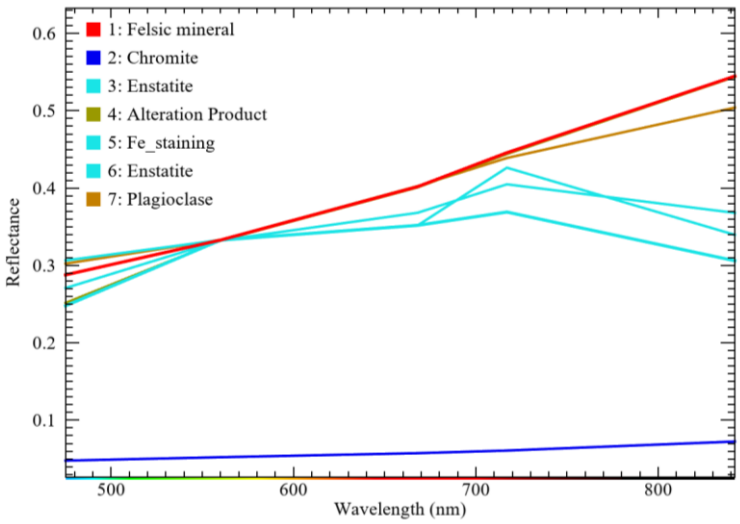

Figure 4.14: Custom reference library from Image 4.

The Pearson correlation coefficient was applied to quantify the similarity between the extracted spectra and the corresponding spectra from the USGS library (Table 4.5), providing a statistical measure to assess both the degree of similarity and the subtle differences between them.

Table 4.5: Pearson correlation coefficient

	Reference USGS Spectra					Extracted endmembers						
	Augite	**Enstatite**	**Plagioclase**	**Chromite**	**Hematite**	**1: Felsic mineral**	**2: Chromite**	**3: Enstatite**	**4: Alteration Product**	**5: Fe-stains**	**6: Enstatite**	**7: Plagioclase**
Augite	1,00											
Enstatite	-0,16	1,00										
Plagioclase	0,83	-0,44	1,00									
Chromite	0,89	-0,35	0,99	1,00								
Hematite	0,69	-0,08	0,89	0,89	1,00							
1: Felsic mineral	0,85	-0,44	1,00	0,99	0,88	1,00						
2: Chromite	0,85	-0,52	0,99	0,98	0,83	0,99	1,00					
3: Enstatite	0,66	0,63	0,38	0,48	0,59	0,40	0,32	1,00				
4: Alteration Product	0,90	-0,37	0,99	0,99	0,88	0,99	0,99	0,48	1,00			
5: Fe-stains	0,82	0,26	0,75	0,80	0,88	0,75	0,69	0,89	0,80	1,00		
6: Enstatite	0,45	0,48	0,45	0,46	0,75	0,44	0,36	0,80	0,48	0,85	1,00	
7: Plagioclase	0,85	-0,44	1,00	0,99	0,88	1,00	0,99	0,40	0,99	0,75	0,44	1,00

The reference (Table 4.6) enstatite spectrum exhibits a negative correlation with the extracted spectra of felsic minerals, chromite, and alteration products; shows a weak positive correlation with Class 5, which corresponds to Fe-stained material; a moderate correlation with Class 6, identified as enstatite; and a strong correlation with Class 3, also enstatite. The reference spectra for plagioclase and chromite show moderate correlation with the extracted spectra of Class 3 and Class 6, both identified as enstatite; a strong correlation is observed with Class 5, associated with Fe-staining; while a very strong correlation is found with Class 1 (felsic minerals), Class 2 (chromite), and Class 4 (alteration products). Similarly, the reference augite spectrum exhibits a moderate correlation with Class 6 (enstatite); strong correlations with Class 1 (felsic minerals), Class 2 (chromite), Class 3 (enstatite), and Class 5 (Fe-staining); and a very strong correlation with Class 4 (alteration products).

Table 4.6: Pearson correlation coefficient of the reference spectra and extracted spectra

Correlation coefficient	Correlation interpretation	Reference spectra vs. the extracted spectra
<0	Negative correlation	• Enstatite vs. Classes 1 (felsic mineral), 2 (chromite), Class 4 (alteration product), and Class 7 (plagioclase).
0-0,1	no correlation	-
0,1-0,3	weak correlation	• Enstatite vs. Class 5 (Fe-stains)
0,3-0,6	moderate correlation	• Plagioclase vs. Class 3 (enstatite), and Class 6 (enstatite) • Augite vs. Class 6 (enstatite). • Enstatite vs. Class 6 (enstatite). • Chromite vs. Class 3 (enstatite), and Class 6 (enstatite). • Hematite vs. Class 3 (enstatite).
0,6-0,9	strong correlation	• Augite vs Class 1 (felsic mineral), Class 2 (chromite), Class 3 (enstatite), Class 5 (Fe-stains), and Class 7 (plagioclase). • Enstatite vs. Class 3 (enstatite). • Hematite vs. Class 1 (felsic mineral), Class 2 (chromite), Class 4 (alteration product), Class 5 (Fe-stains), Class 6 (hematite), and Class 7 (plagioclase). • Plagioclase vs and Class 5 (Fe-stains). • Chromite vs and Class 5 (Fe-stains).
0,9-1	very strong correlation	• Augite vs. Class 4 (alteration product). • Plagioclase vs. Class 1 (felsic mineral), Class 2 (chromite), Class 4 (alteration product), and Class 7 (plagioclase). • Chromite vs. Class 1 (felsic mineral), Class 2 (chromite), Class 4 (alteration product), and Class 7 (plagioclase).

Furthermore, the extracted endmember classes were also examined to identify any similarities with the associated spectral signatures (Table 4.7). The extracted felsic mineral (Class 1) and chromite spectra (Class 2) show moderate correlation with the extracted spectra of Class 3 and Class 6, both identified as enstatite, a strong correlation is observed with Class 5, associated with Fe-staining, while a very strong correlation is found with Class 2 (chromite), Class 4

(alteration products), and Class 7 (plagioclase). The extracted enstatite (Class 3) spectrum exhibits a moderate correlation with Class 4 (alteration products) and Class 7 (plagioclase) and a strong correlation with both Class 5 (Fe-stains) and Class 6 (enstatite), suggesting consistency within the enstatite group and shared spectral features with Fe-stain spectra. The extracted enstatite (Class 6) spectrum exhibits a moderate correlation with Class 7 (plagioclase). A very strong correlation exists among Class 1 (felsic mineral), Class 2 (chromite), Class 4 (alteration product), and Class 7 (plagioclase).

Table 4.7: Pearson correlation coefficient of the extracted classes.

Correlation coefficient	Correlation interpretation	Extracted classes
<0	Negative correlation	-
0-0,1	no correlation	-
0,1-0,3	weak correlation	-
0,3-0,6	moderate correlation	• 1 (felsic mineral) vs. 3 (enstatite) and 6 (enstatite) • 2 (chromite) vs. 3 (enstatite) and 6 (enstatite) • 3 (enstatite) vs. 4 (alteration product) and 7 (plagioclase) • 4 (alteration product) vs. 6 (enstatite) • 6 (enstatite) vs. 7 (plagioclase)
0,6-0,9	strong correlation	• 1 (felsic mineral) vs. 5 (Fe-stains). • 2 (chromite) vs. 5 (Fe-stains). • 3 (enstatite) vs. 5 (Fe-stains) and 6 (enstatite) • 4 (alteration product) vs. 5 (Fe-stains). • 5 (Fe-stains) vs. 6 (enstatite) and 7 (plagioclase)
0,9-1	Very-strong correlation	1 (felsic mineral), 2 (chromite), 4 (alteration product), 7 (plagioclase)

Therefore, Class 3 (enstatite) showed a strong correlation with both Class 5 (Fe-stains) and Class 6 (enstatite), suggesting spectral similarity among them. Consequently, these three classes were merged to develop a custom spectral library consisting of five classes (Figure 4.15).

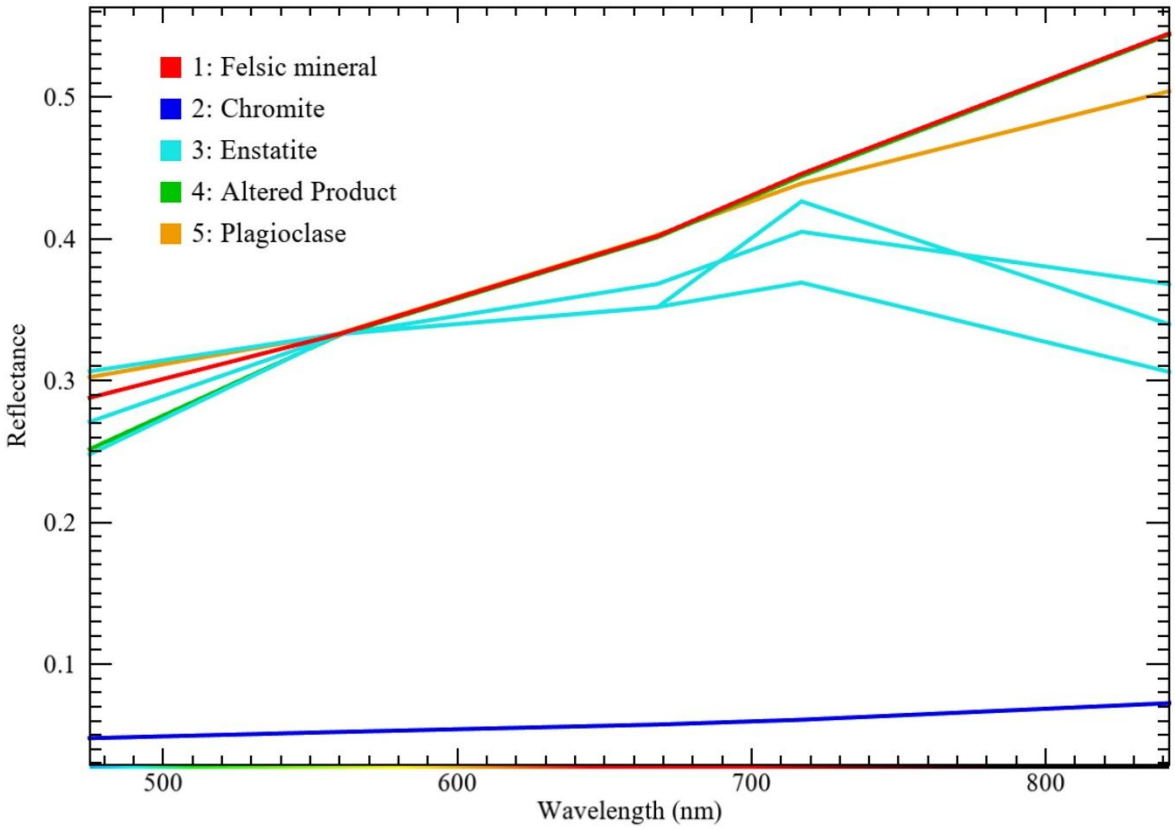

Figure 4.15: Simplified custom reference library from Image 4.

4.6 Spectral classification

The extracted endmembers served as reference spectra to develop a custom multispectral library tailored to the RLS rocks, which was then used to classify all captured sections from Test 2 using the SAM algorithm. Multiple angular thresholds were evaluated during the classification process to determine the optimal value, with 0.5 radians found to be the most suitable for accurate classification. The following sections report the spectral classification results of the captured images.

4.6.1 Spectral classification of Image 4

SAM classification was first applied to Image 4 (1509.58 m to 1517.02 m) from which the custom reference spectra (Figure 4.15) were extracted. The RGB composite image (Figure 4.16a), constructed from multispectral bands 3, 2, and 1, is displayed alongside the corresponding lithological units as per manual logging. To improve visual interpretation, the image was enhanced using histogram equalisation, as shown in Figure 4.16b, which increases tonal contrast and makes geological features easier to distinguish. The final SAM classification output for Image 4 is presented in Figure 4.16c.

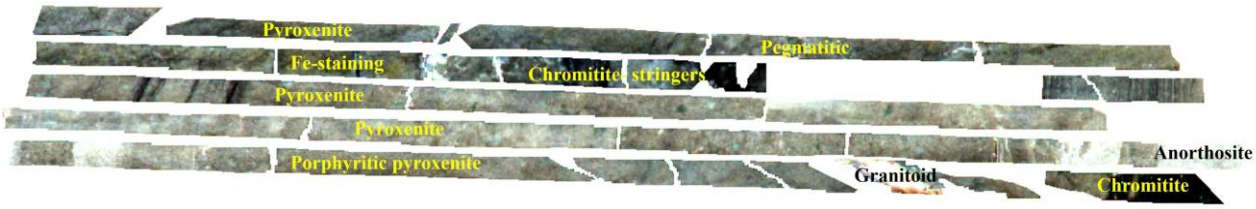

(a) Multispectral bands 3, 2, 1 (RGB) to display different lithologies.

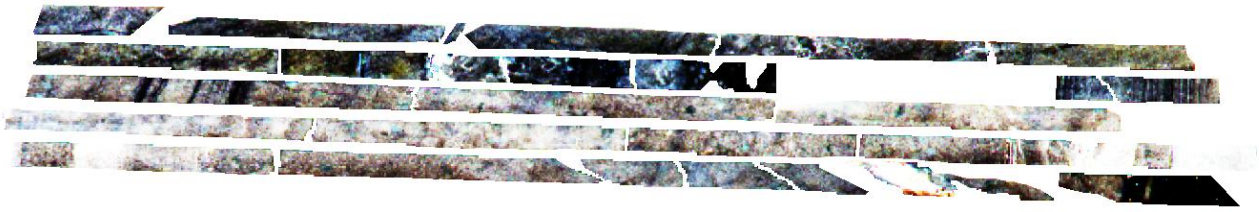

(b) Multispectral bands 3, 2, 1 (RGB) enhanced with histogram equalisation.

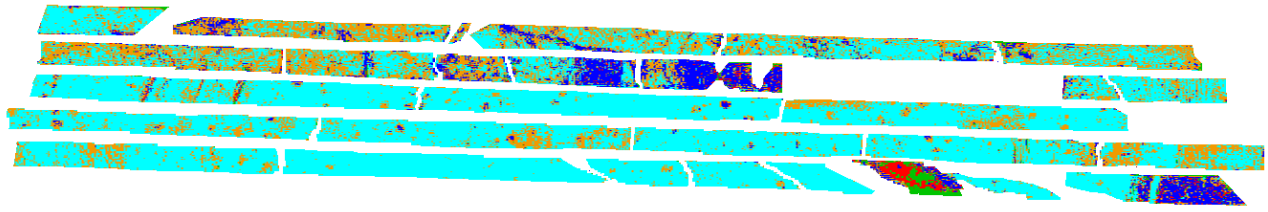

(c) SAM classification with mineral spectra extracted from the same image.

Figure 4.16: Image 4 (1509.58 m to 1517.02 m) lithologies (a), enhanced with histogram equalisation (b), and spectral angle mapper (c) with cyan (enstatite), orange (plagioclase), red (felsic mineral), green (alteration product), and blue (chromite).

4.6.2 Spectral classification of Images 1, 2, and 3 from Test 2

The four spectra of the custom reference spectral library (Figure 4.15) were used to classify Image 1 (Figure 4.17a), excluding the chromite spectrum, as this section of the core does not contain chromitite. The RGB composite images, constructed from multispectral bands 3, 2, and 1, are displayed alongside the corresponding lithologies for Image 1 (Figure 4.17a). To improve visual interpretation, the image was also enhanced using histogram equalisation for Image 1 (Figure 4.17b). The final SAM classification output for Image 1 is presented in Figure 4.17c. The enstatite class in Figure 4.17d is presented to evaluate the classification accuracy of the SAM outputs.

(a) Multispectral bands 3, 2, 1 (RGB) to display different lithologies

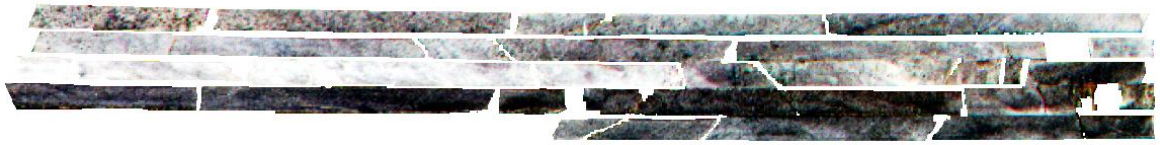

(b) Multispectral bands 3, 2, 1 (RGB) enhanced with histogram equalisation.

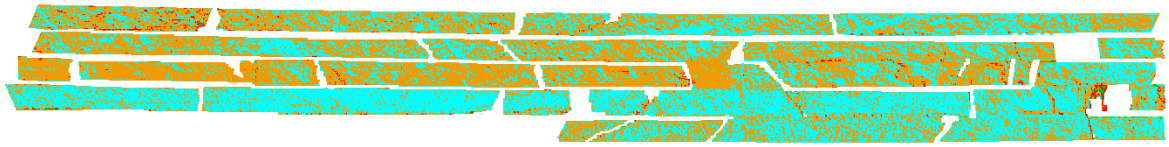

(c) SAM classification with mineral spectra from image 4

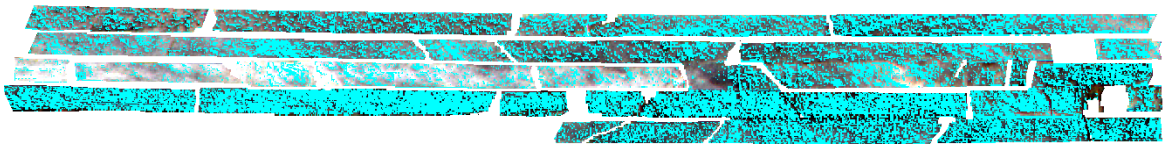

(d) Enstatite from SAM classification

Figure 4.17: Image 1 (561.26 m to 568.7 m) lithologies (a), enhanced with histogram equalisation (b), spectral angle mapper classification (c), and the display of enstatite only from the SAM classification (d) cyan (enstatite), green (alteration product), red (felsic-mineral), and orange (plagioclase).

Image 2 (919.88 m to 927.35 m) was classified using enstatite and plagioclase spectra from the custom reference spectral library (Figure 4.15). The results are illustrated through the RGB composite (Figure 4.18a), histogram-equalised image (Figure 4.18b), and the final SAM classification output (Figure 4.18c). To assess the accuracy of the SAM classification, the plagioclase class is separately visualised in Figure 4.18d.

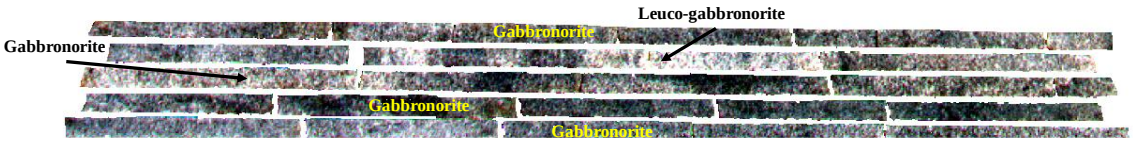

(a) Multispectral bands 3, 2, 1 (RGB) to display different lithologies.

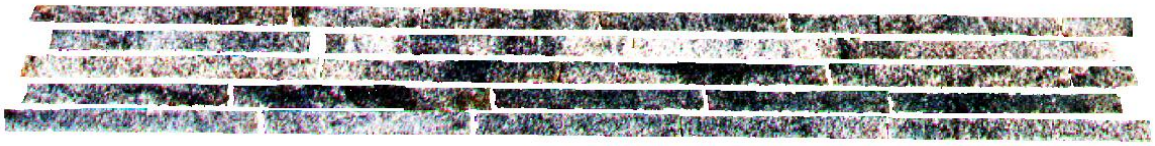

(b) Multispectral bands 3, 2, 1 (RGB) enhanced with histogram equalisation.

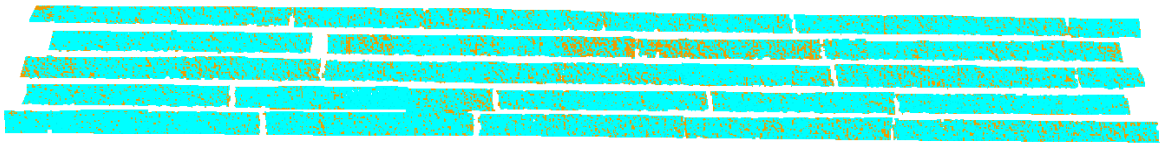

(c) SAM classification

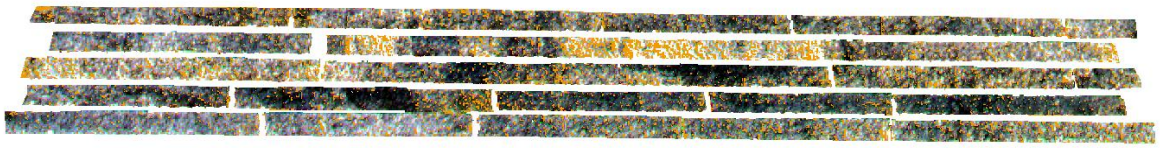

(d) Classified plagioclase from SAM classification

Figure 4.18: Image 2 (919.88 m to 927.35 m) lithologies (a), enhanced with histogram equalisation (b), spectral angle mapper (c), and the display of plagioclase only (d) cyan (enstatite), and orange (plagioclase).

Image 3 (1373.84 m to 1380.88 m) was also classified using felsic mineral rather than the plagioclase spectra, enstatite, and alteration product spectra from the custom reference spectral library (Figure 4.15). The results are illustrated through the RGB composite (Figure 4.19a), histogram-equalised image (Figure 4.19b), and the SAM classification output (Figure 4.19c). The enstatite and alteration product classes were combined in the final classification output Figure 4.19d.

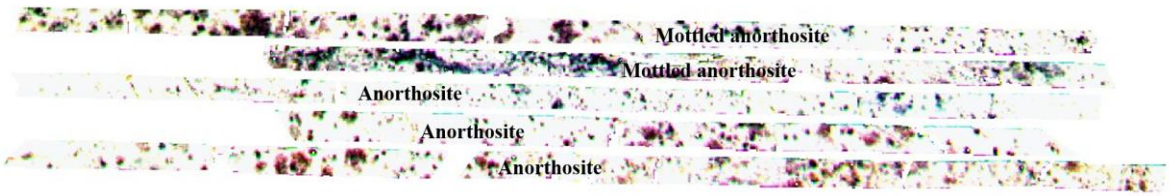

(a) Multispectral bands 3, 2, 1 (RGB) to display different lithologies.

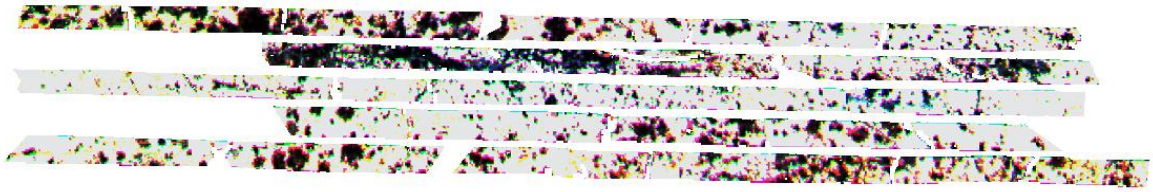

(b) Multispectral bands 3, 2, 1 (RGB) enhanced with histogram equalisation.

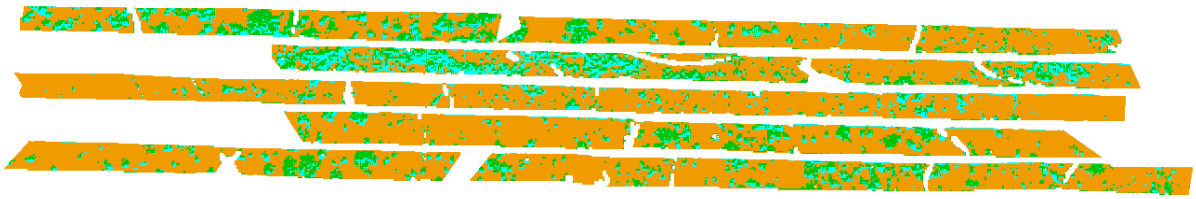

(c) SAM classification with all the classes.

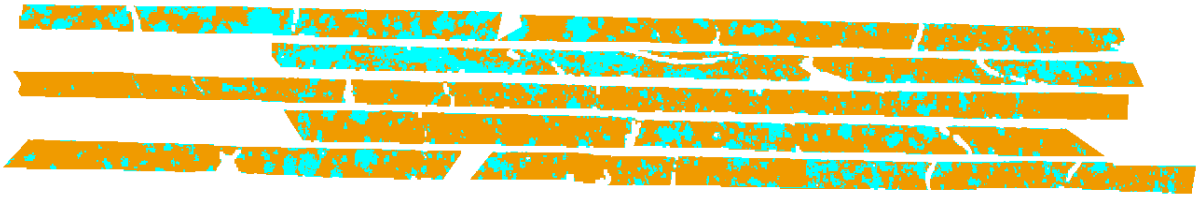

(d) Final SAM classification

Figure 4.19: Image 3 (1373.84 m to 1380.88 m) lithologies (a), enhanced with histogram equalisation (b), spectral angle mapper with all classes (c), and the display of plagioclase and combined classes (d) cyan (enstatite), green (alteration product), and orange (plagioclase).

4.6.3 Spectral classification with the image-specific spectra of Images 1, 2, and 3

To evaluate improvements in the classification of Images 1, 2, and 3 using the SAM algorithm with a threshold of 0.5, mineral spectra from each image were extracted using both SHW and manual extraction of plagioclase spectra used to classify the same images from which they were extracted.

The endmember spectra extracted from Image 1 (Figure 4.20) were used to classify the same image. Five endmembers were identified and compared with USGS reference spectra for major minerals (Figure 4.13) and potential alteration products (Figure 4.21), based on visible surface alteration of the drill-core. Class 1 was identified as actinolite, Class 2 as variable plagioclase spectra, Class 3 as enstatite, and Classes 4 and 5 as alteration products. The latter may include alteration products of the RLS rocks such as albitised plagioclase, chlorite, serpentine, talc, epidote, actinolite, and secondary carbonates (e.g., calcite), commonly noted in the BC (Roelofse *et al.*, 2024; Roelofse and Ashwal, 2012), as well as Fe-oxides resulting from hydrothermal or low-grade metamorphic processes (Di Tommaso and Rubinstein, 2007).

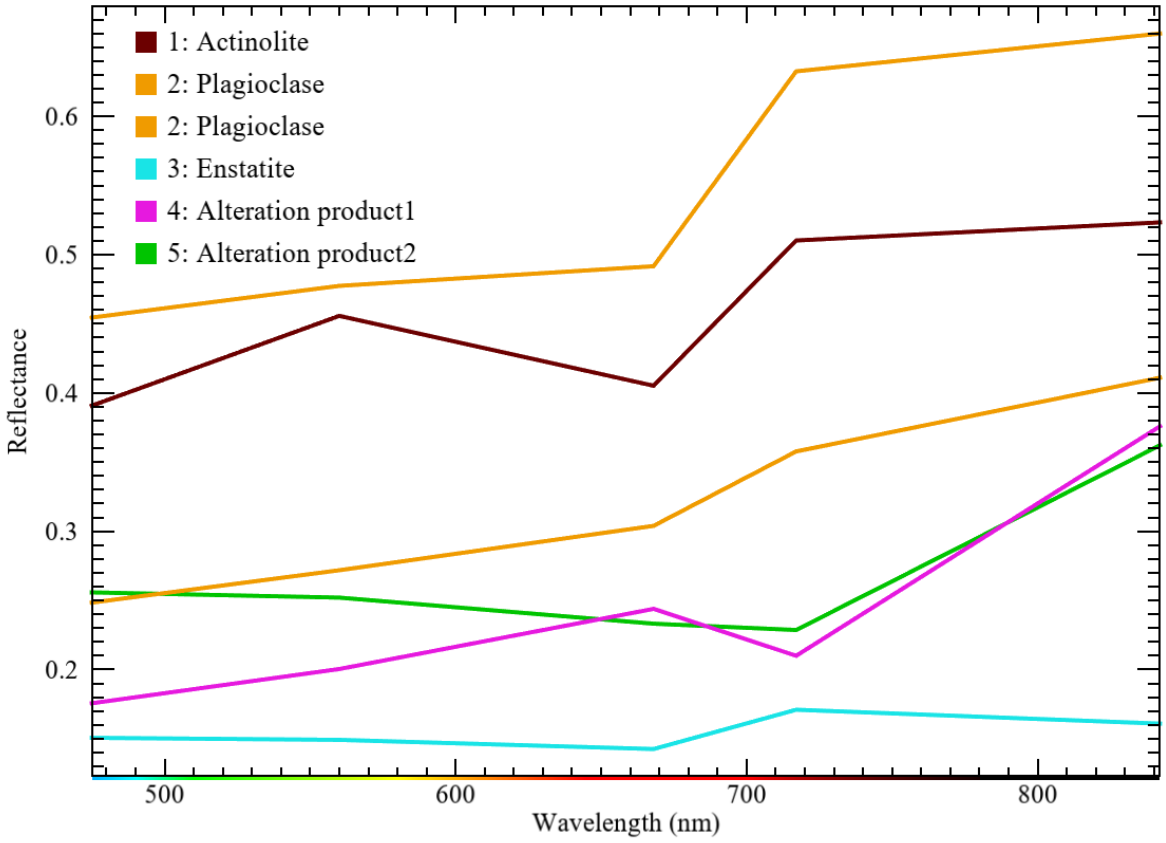

Figure 4.20: Extracted mineral spectra from Image 1 (561.26 m to 568.7 nm).

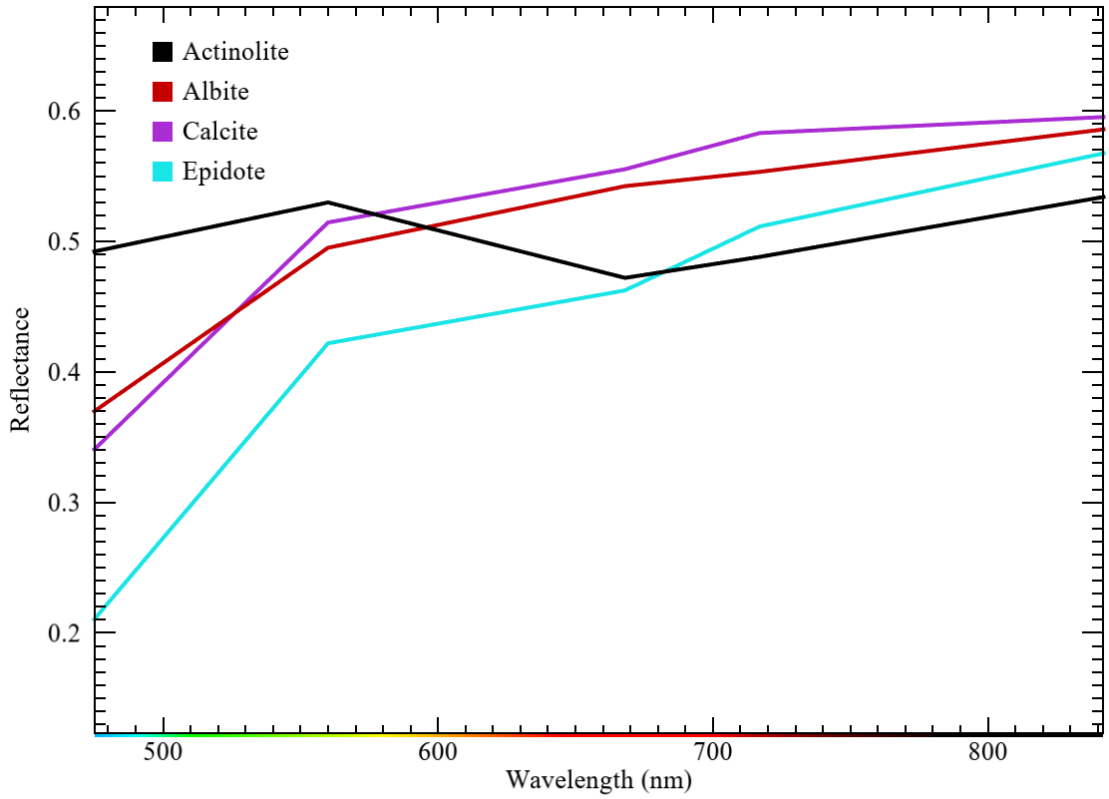

Figure 4.21: Potential alteration minerals of the Bushveld Complex from the USGS Version 7 Beckman mineral spectral library.

Classes 1 to 5 (Figure 4.20) were used to classify Image 1 (Figure 4.22a) and generate the full classification map (Figure 4.22b). For improved visualization of major minerals, alteration classes were omitted, and enstatite and actinolite were grouped (Figure 4.22c). Additionally, the plagioclase class was isolated and overlaid on the RGB composite image to highlight its spatial distribution (Figure 4.22d).

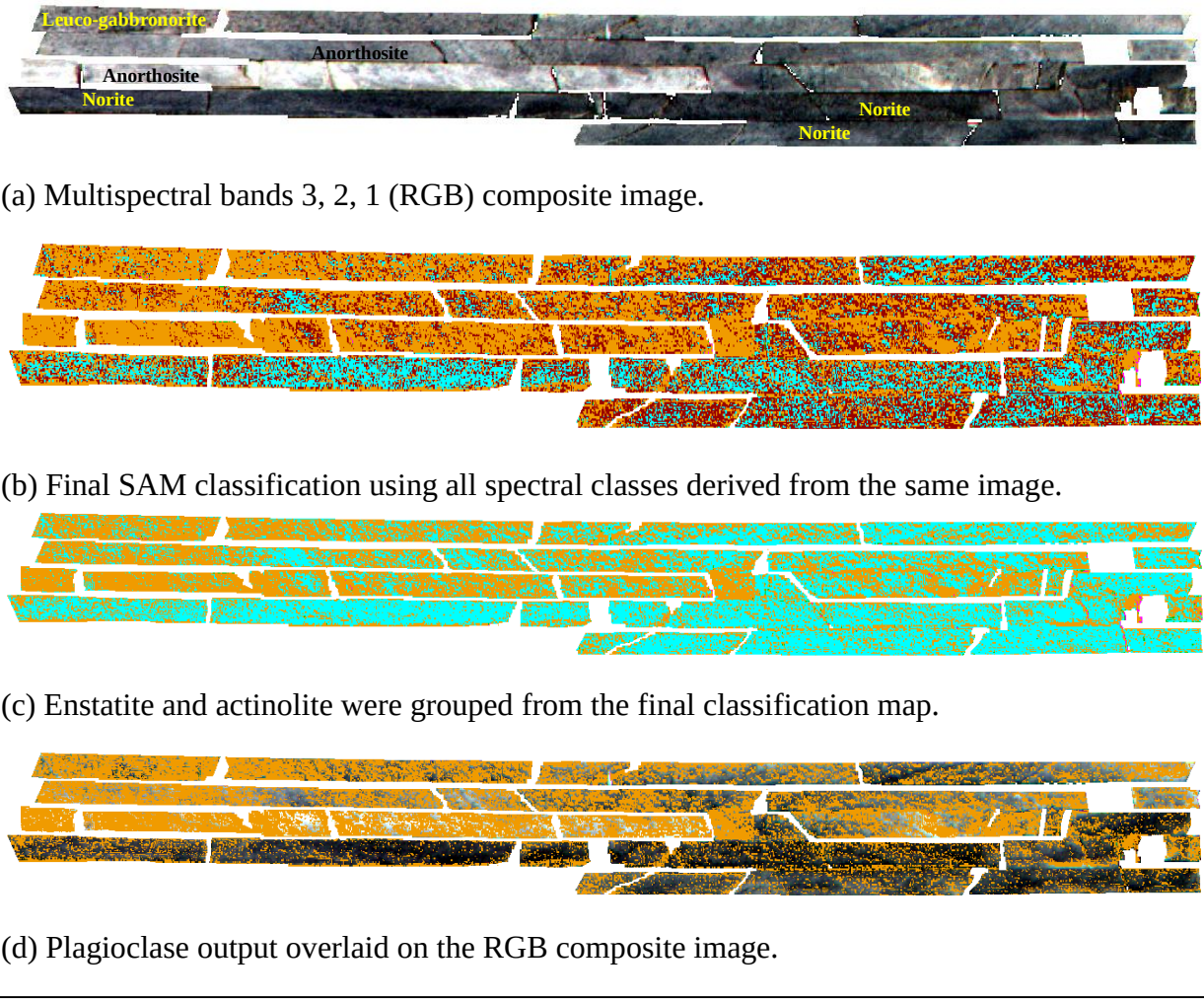

(a) Multispectral bands 3, 2, 1 (RGB) composite image.

(b) Final SAM classification using all spectral classes derived from the same image.

(c) Enstatite and actinolite were grouped from the final classification map.

(d) Plagioclase output overlaid on the RGB composite image.

Figure 4.22: RGB composite of Image 1 (561.26 m to 568.7 m) (a); final SAM classification output for Images 1 (b), enstatite and actinolite grouped (c), plagioclase output class displayed separately (d). cyan (enstatite), maroon (actinolite), green and pink (alteration products), and orange (plagioclase).

The derived endmember spectra from Image 2 (Figure 4.23) were subsequently utilised to classify the same image. Five endmembers were extracted, with Classes 1 to 4 corresponding to enstatite, and Class 5 representing manually extracted plagioclase.

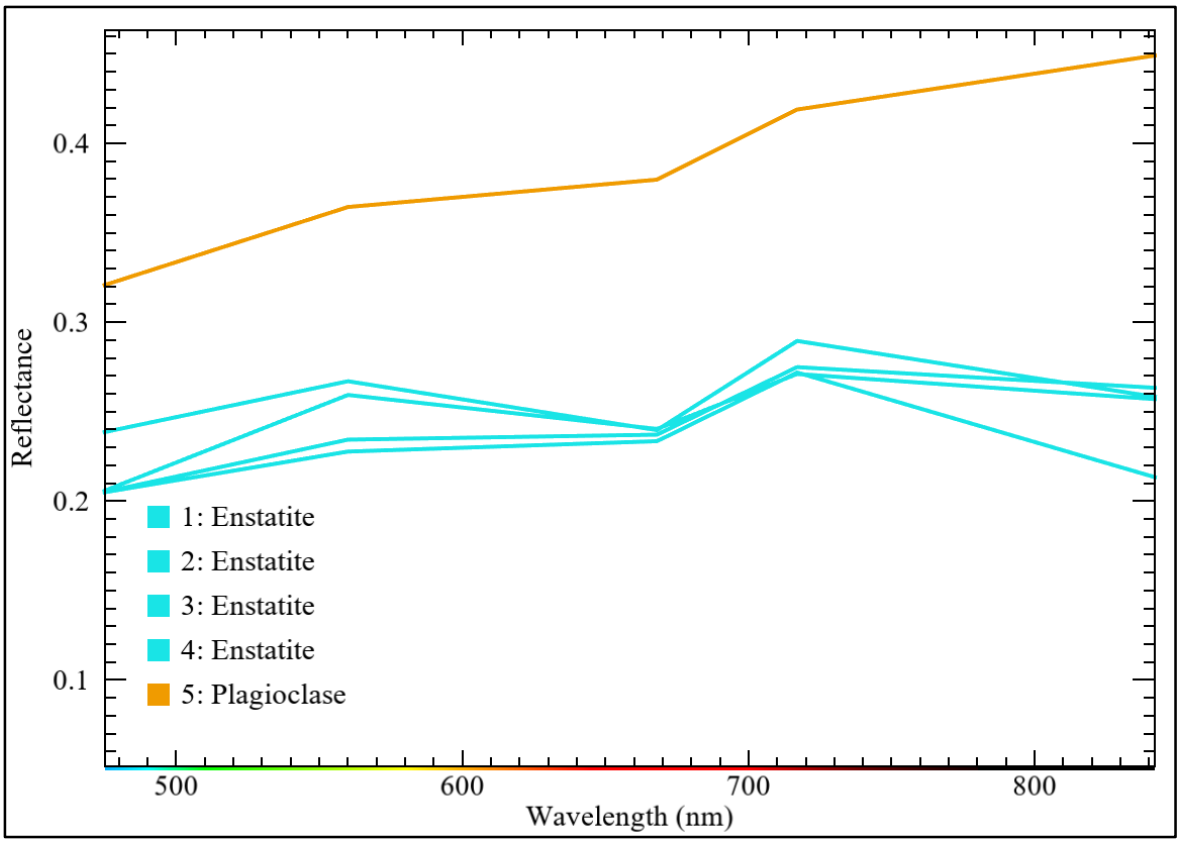

Figure 4.23: Extracted mineral spectra from Image 2 (919.88 m to 927.35 m).

Classes 1 to 4, associated with enstatite, and Class 5, representing plagioclase (Figure 4.23), were then used to classify Image 2 (Figure 4.24a) and produce a final classification output comprising two major minerals (Figure 4.24b). For improved visualization, the enstatite (Figure 4.24c) and plagioclase (Figure 4.24d) classes are displayed separately, overlaid on the RGB composite images.

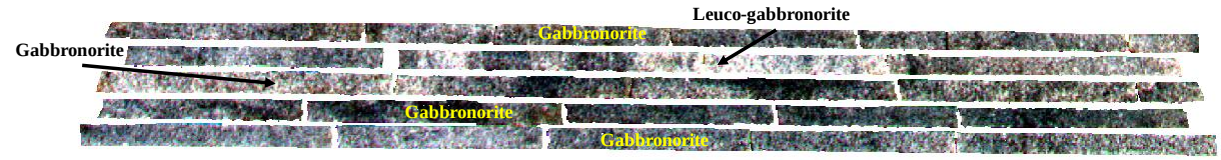

(a) Multispectral bands 3, 2, 1 (RGB) composite image

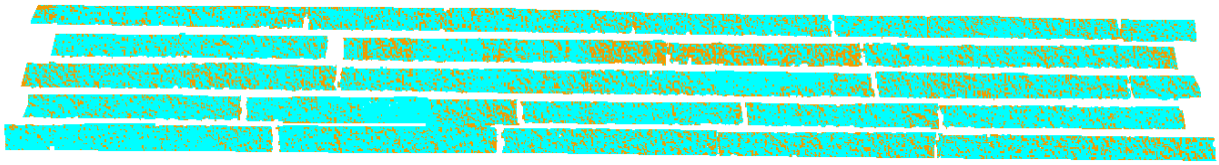

(b) Final spectral angle mapper classification.

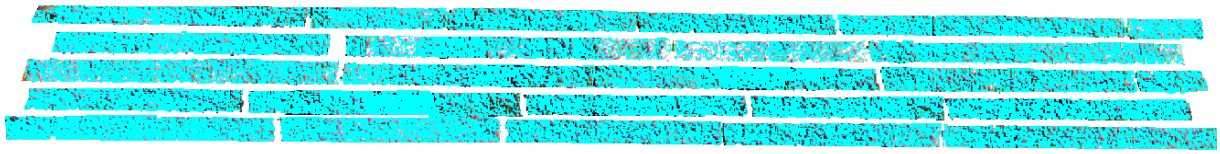

(c) Enstatite output above the RGB composite image

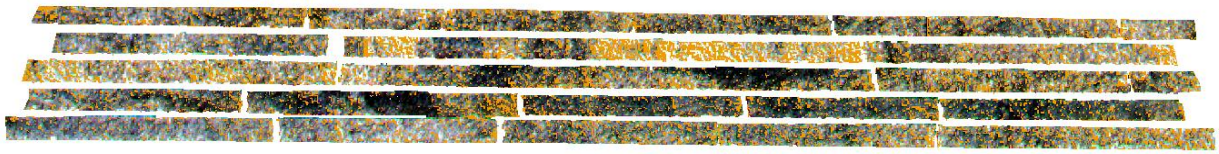

(d) Plagioclase output above the RGB composite image

Figure 4.24: RGB composite of Image 2 (919.88 m to 927.35 m) (a); spectral angle mapper classification output for Images 2 (b) enstatite (c), plagioclase output classes (d) displayed separately. Cyan (enstatite), and orange (plagioclase).

The same workflow was applied to Image 3 (1373.84 m to 1380.88 m). The resulting endmember spectra (Figures 4.25 and 4.26) were used to classify the image. Four endmembers were extracted from Image 3 (Figure 4.25), corresponding to Class 1 (enstatite), Class 2 (Fe-staining), Class 3 (alteration product), and Class 4 (plagioclase). Figure 4.26 illustrates three of the extracted mineral spectra, which exhibit similar spectral characteristics within the RE and NIR bands.

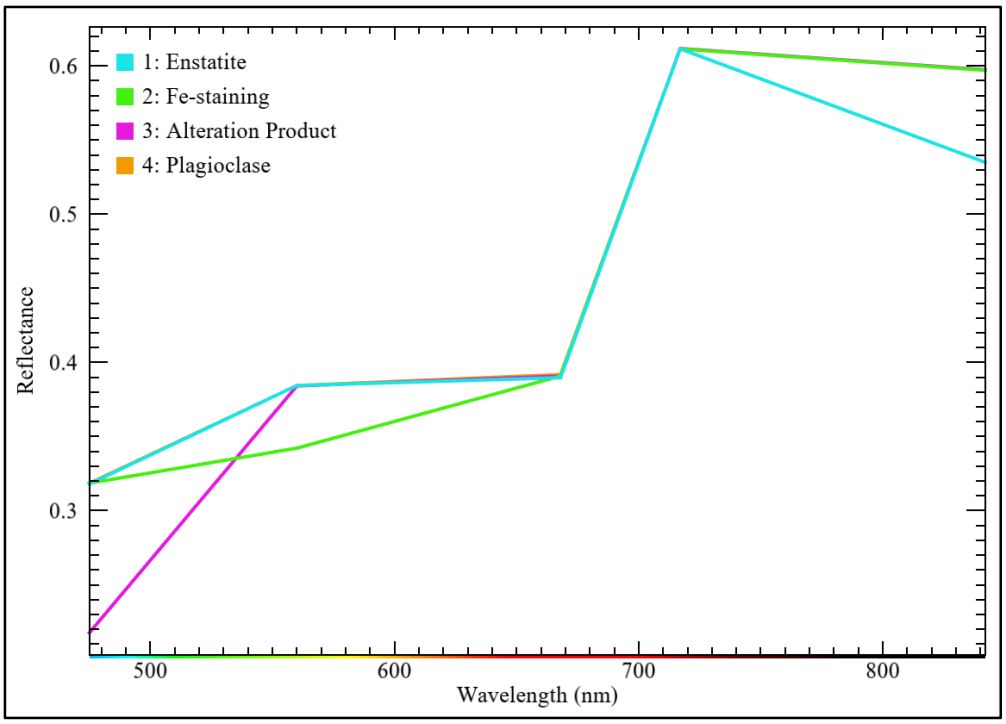

Figure 4.25: Four extracted mineral spectra from Image 3 (1373.84 m to 1380.88 m).

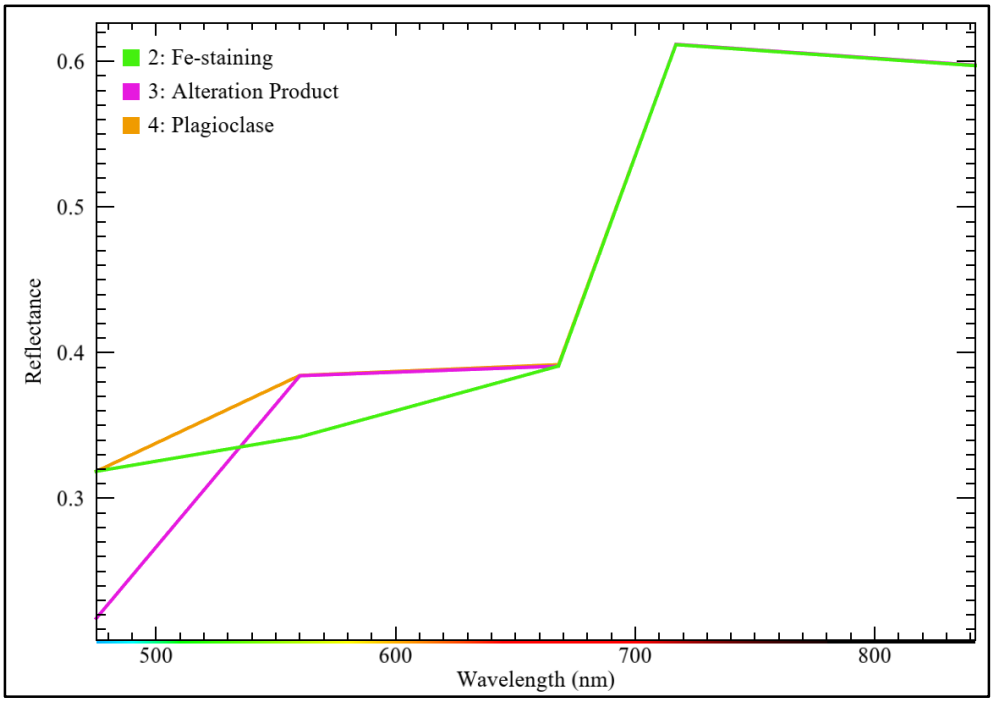

Figure 4.26: Three of four extracted mineral spectra from Image 3 (1373.84 m to 1380.88 m).

Classes 1 (enstatite) and 2 (Fe-staining) were combined under a single symbol to represent enstatite-bearing lithologies when classifying Image 3 (Figure 4.27a). This resulted in three

output classes: enstatite (with Fe-stain in cyan), plagioclase (orange), and alteration products (green) (Figure 4.27b). The final classification output shows the enstatite grouped with alteration products in a single class (Figure 4.27c), and plagioclase (orange) and alteration products (purple) are presented separately (Figure 4.27d) to enhance visualization.

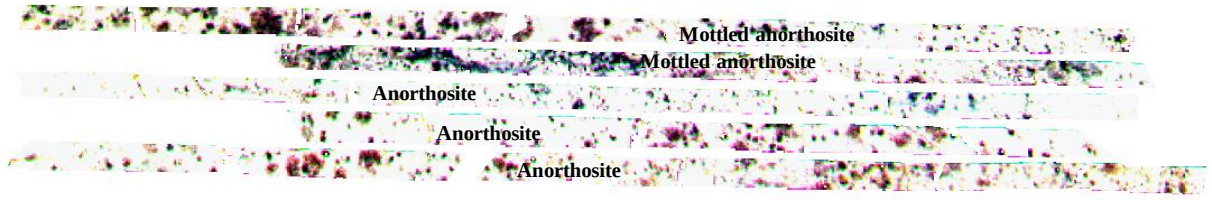

(a) Multispectral bands 3, 2, 1 (RGB) composite image

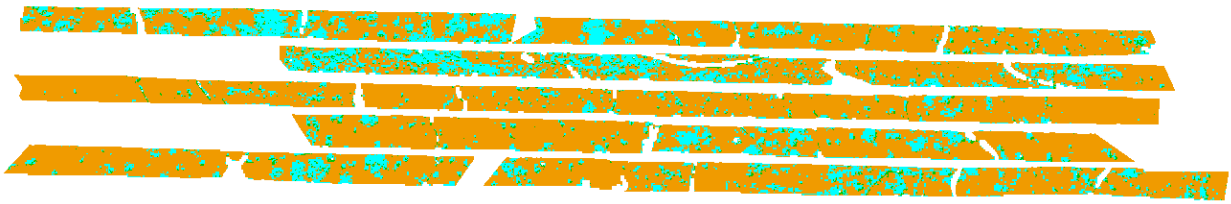

(b) SAM Classification showing three output mineral classes.

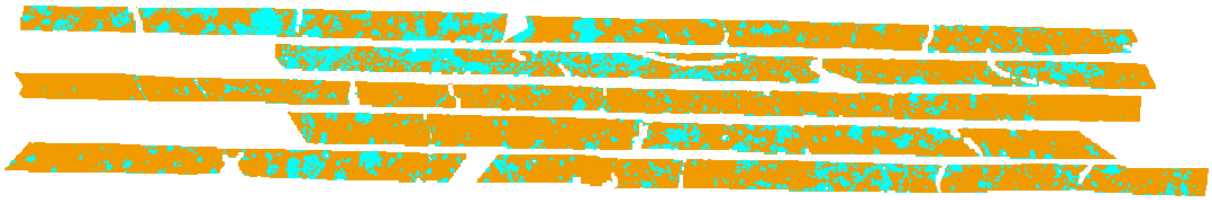

(c) Final SAM classification.

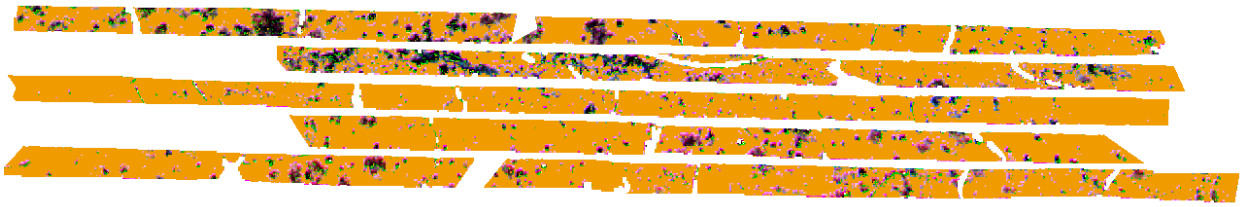

(d) Plagioclase and alteration product overlaid on the RGB composite image.

Figure 4.27: RGB composite of Image 3 (1373.84 m to 1380.88 m) (a); three output mineral classes, green (alteration product) (b) Final SAM classification output for Images 3 (c), alteration product (purple) and plagioclase output classes (d) overlaid on the composite RGB image. Cyan (enstatite) and orange (plagioclase).

4.6.4 Spectral classification of validation images

The additional Images 5-7 were classified using the spectra extracted from all the images, which were combined to form the RLS custom reference spectral library. Although initial attempts used all classes in the library, the final SAM classification was refined by selecting only the classes which spectral signatures were distinctly detected in each image to improve classification results. Beyond the selection of detected minerals, minerals with similar spectral features were separately evaluated and classified to enhance accuracy and minimize misclassification using the threshold selection tool in ENVI. This strategy was critical for Image 7, where chromite and plagioclase spectra overlap closely and the chromitite and mottled anorthosite sections were separated.

The SAM technique was used to classify Image 5 (Figure 4.28) using a spectral angle threshold of 0.3 radians, while Images 6 (Figure 4.29) and 7 (Figure 4.30) were classified with a threshold of 0.5 radians, reflecting adjustments aimed at balancing classification accuracy. The results are illustrated through the RGB composite alongside the corresponding lithologies for Image 5 (Figure 4.28a) and the final SAM classification output (Figure 4.28b). To assess the accuracy of the SAM classification, the enstatite (Figure 4.28c) and plagioclase (Figure 4.28d) classes are separately visualised.

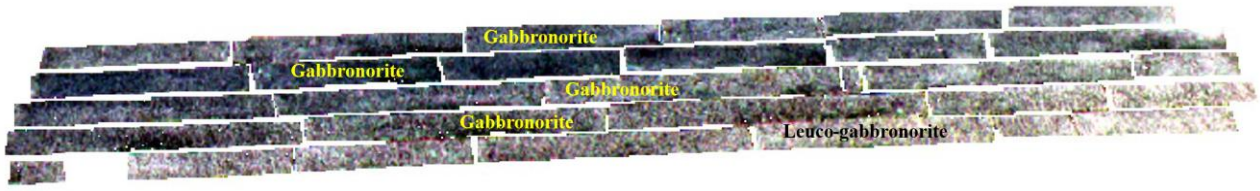

(a) Multispectral bands 3, 2, 1 (RGB) to display different lithologies.

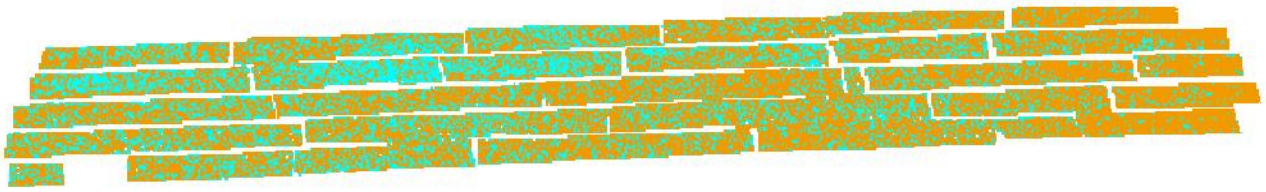

(b) Final SAM classification with classes extracted from Images 1-4.

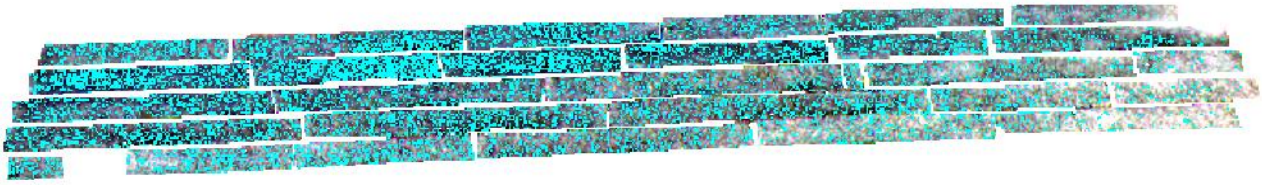

(c) Enstatite from SAM classification

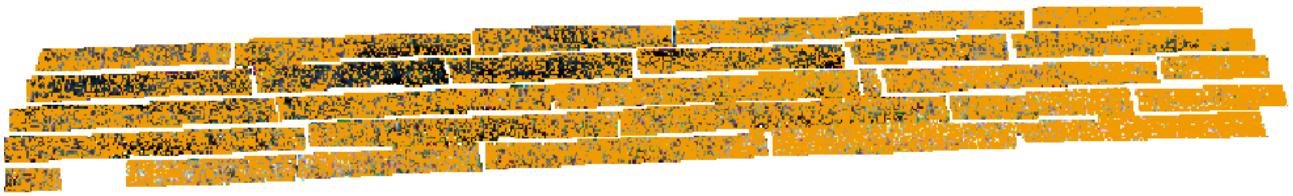

(d) Plagioclase from SAM classification.

Figure 4.28: Image 5 (576.09 m to 583.45 m) lithologies (a), SAM output (b), enstatite (c), and plagioclase (d), cyan (enstatite), and orange (plagioclase).

The results are illustrated through the RGB composite alongside the corresponding lithologies for Image 6 (Figure 4.29a), and the final SAM classification output (Figure 4.29b). To assess the accuracy of the SAM classification, enstatite (Figure 4.29c) and plagioclase (Figure 4.29d) classes are separately visualised.

(a) Multispectral bands 3, 2, 1 (RGB) to display different lithologies.

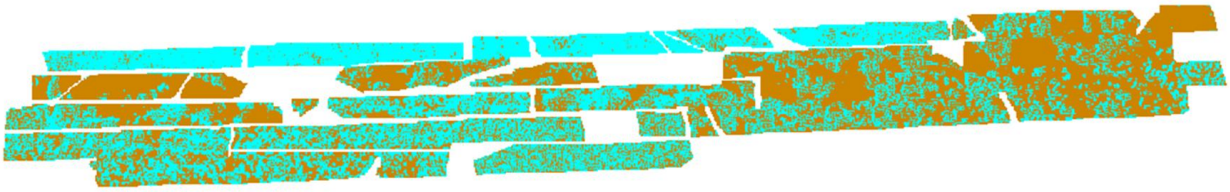

(b) Final SAM classification with spectra extracted from Images 1-4.

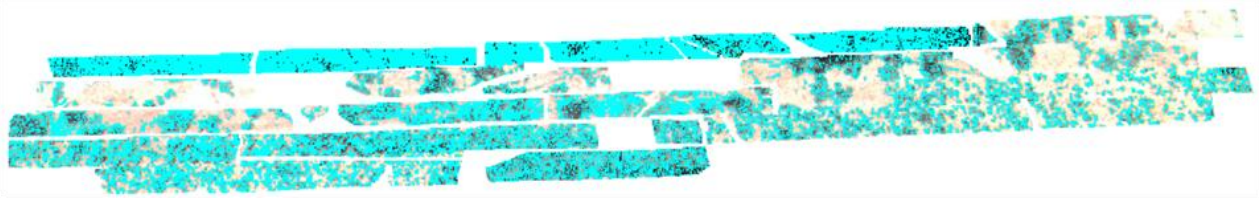

(c) SAM classification of enstatite-bearing lithologies.

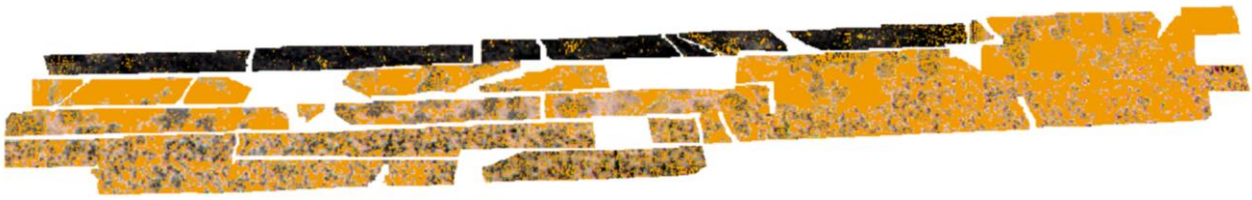

(d) SAM classification of plagioclase areas.

Figure 4.29: Image 6 (1402.83 m to 1409.62 m) lithologies (a), SAM output (b), enstatite class output (c), and plagioclase class output (d), cyan (enstatite), and orange (plagioclase).

The results are illustrated through the RGB composite alongside the corresponding lithologies for Image 7 (Figure 4.30a), and the final SAM classification output (Figure 4.30b). To assess the accuracy of the SAM classification, the chromitite layer (Figure 4.30c) and mottled anorthosite (Figure 4.30d) sections are separately visualised.

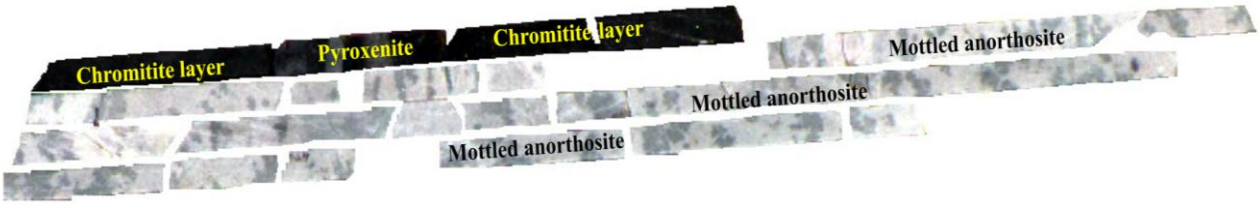

(a) Multispectral bands 3, 2, 1 (RGB) to display different lithologies.

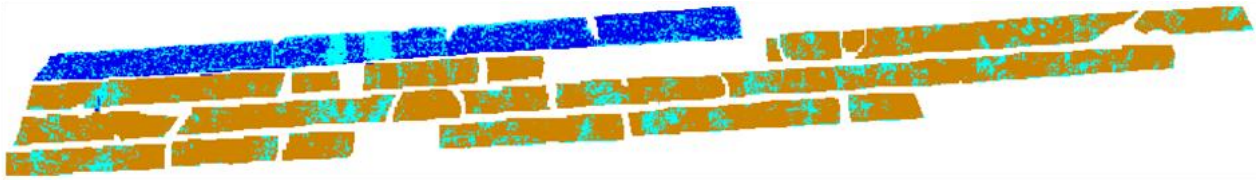

(b) SAM classification

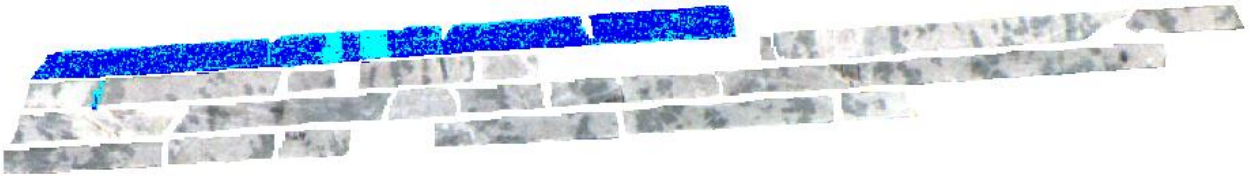

(c) SAM classification of the chromitite section.

(d) SAM classification of the mottled anorthosite.

Figure 4.30: Image 7 (1559.52 m to 1564.72 m) lithologies (a), SAM output of the entire core (b), enstatite and chromite classes of the chromitite section (c), and plagioclase and enstatite classes of the mottled anorthosite section (d), cyan (enstatite), orange (plagioclase), and blue (chromite).

4.7 Classification accuracy assessment

The spatial classification accuracy of individual images was visually assessed using Table I1 (Appendix I), comparing SAM classification output when using spectra from Image 4 to classify other images and using image-specific spectra, in reference to petrographic mineralogy. The classification categories for each image are summarised in Table 4.8. Note that Images 5-7 were classified only using extracted spectra, so no results are available under image-specific spectra.

Image 1 is classified with low accuracy due to significant spatial mismatches in the identification of major minerals (orthopyroxene and plagioclase) compared to petrographic data, along with notable under- and over-classification of both primary and alteration minerals. Alteration features are not reliably detected. However, using image-specific spectra improves classification, with major minerals moderately identified and alteration closely comparable to petrographic observations, though mineral boundaries remain poorly defined.

Image 2 is moderately classified using spectra extracted from Image 4, as major minerals are generally mapped but show imprecise spatial boundaries and some under- or over-classification compared to petrographic data. However, classification using image-specific spectra improves accuracy, resulting in a high classification where major minerals are well mapped with good spatial alignment, though minor misclassification and under- or over-classification still occur.

Images 3, 5, 6, and 7 are highly classified using spectra extracted from Image 4, as major minerals are accurately mapped with good spatial alignment to petrographic data. Minor under- or over-classification and occasional misclassification may occur, particularly where alteration features are grouped with primary minerals and the classifications remain interpretable and consistent with petrographic observations, where available. Image 3 is very highly classified when using image-specific spectra. Major minerals are accurately mapped, where alteration features are grouped with primary minerals, the classifications remain interpretable, and where alteration zones are displayed, they show a close spatial match to petrographic data. Classification errors are minimal, and mineral boundaries are clearly defined.

Image 4 demonstrates high classification accuracy using spectra acquired from the image itself, with major and alteration minerals accurately mapped, clear spatial boundaries, minimal misclassification, and strong agreement with petrographic observations.

Table 4.8: Image Classification Accuracy

Image	**Image classification with extracted spectra**	**Image-specific spectra**
Image 1	Low	Moderate
Image 2	Moderate	High
Image 3	High	Very High
Image 4	-	High
Image 5	High	-
Image 6	High	-
Image 7	High	-

Furthermore, the sampled sections (Figure 4.31) were analyzed to assess classification accuracy by comparing the relative proportions of mafic and felsic minerals identified in the classified images. In anorthositic rocks, a higher abundance of felsic minerals is expected relative to mafic minerals, whereas mafic rocks typically exhibit a predominance of mafic minerals. This distinction reflects their mineralogical composition: anorthosite comprises more than 90% plagioclase; gabbronorite consists of 10-90% plagioclase and pyroxenes; and pyroxenite is dominated by more than 90% pyroxenes.

Consistent with these mineralogical proportions, 40% of the pyroxenite samples in Image 4 exhibit more than 90% pyroxene content when classified using the spectral signatures derived from the same image. Approximately 12% of the anorthosite samples in both classifications contain more than 90% plagioclase. Among the gabbronorite samples, 71% (classified with the image-specific spectra) and 75% (classified with the extracted spectra) display plagioclase and pyroxene proportions within the 10-90% range. In addition, all chromitite samples (samples 19 and 25) contain more than 45% chromite. Although some samples fall outside the defined compositional ranges for their respective rock types, the general trend remains consistent: dark-coloured, mafic rocks exhibit higher proportions of mafic minerals, while lighter-coloured, anorthositic rocks display higher proportions of felsic minerals (Table 4.9).

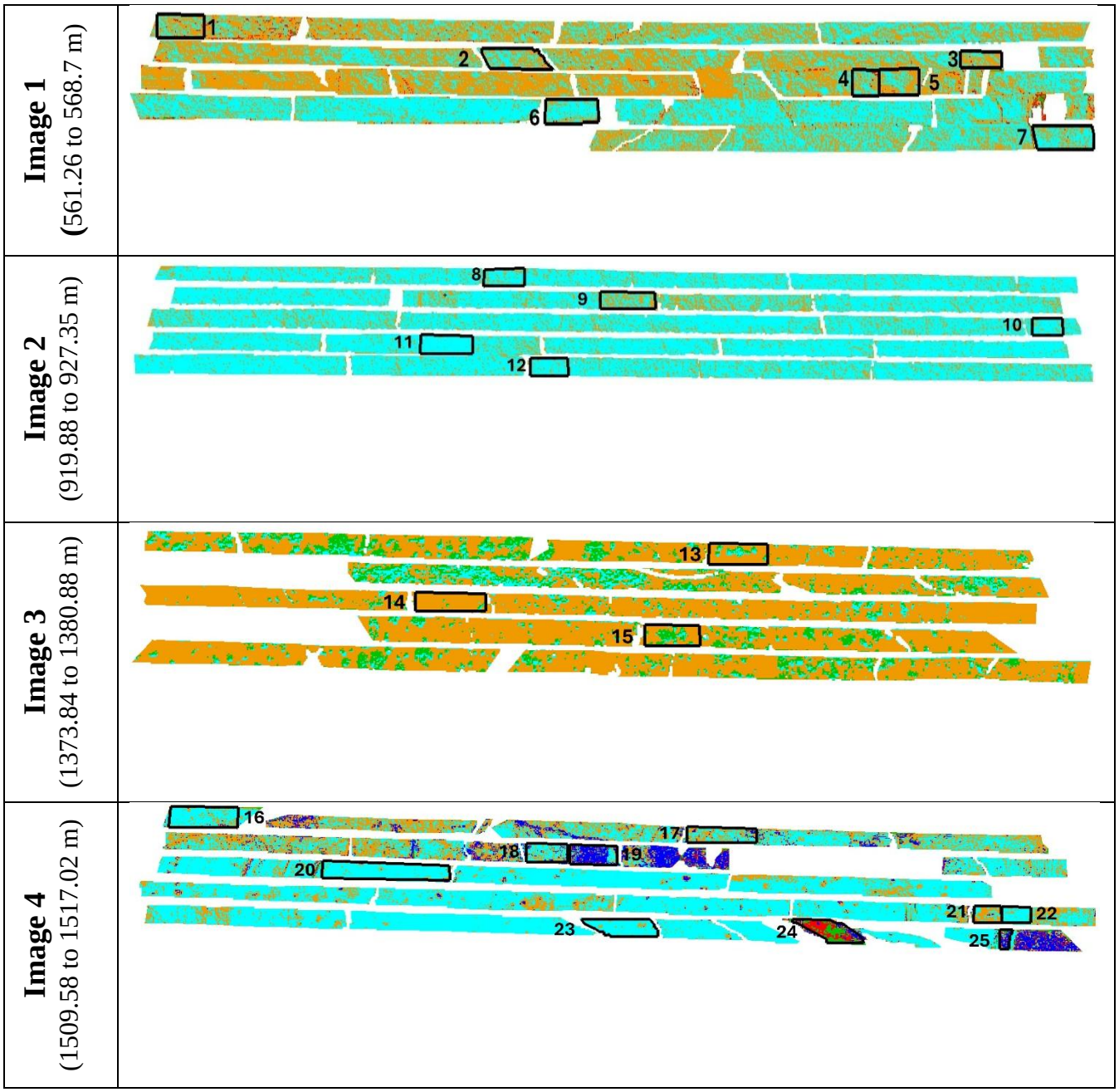

Figure 4.31: Samples 1-25 in the classified Images 1-4.

Table 4.9: Comparison of classified mafic and felsic mineral percentages with lithological description.

Image	Sample ID	Lithology	Image classification with extracted spectra (%)		Image mineral spectra (%)	
			Mafics	Felsics	Mafics	Felsics
Image 1	BH29-NM-01	Spotted anorthosite	35,87	64,13	24,84	74,93
	BH29-NM-02	Anorthosite	45,15	54,85	50,00	49,95
	BH29-NM-03	Anorthosite	32,23	67,77	36,02	62,65
	BH29-NM-04	Anorthosite	45,24	54,76	45,79	53,66
	BH29-NM-05	Highly altered anorthosite	38,39	61,61	37,89	61,55
	BH29-NM-06	Gabbronorite	68,50	31,50	65,95	34,00
	BH29-NM-07	Gabbronorite	64,78	35,22	76,02	22,16
Image 2	BH29-NM-08	Gabbronorite	81,91	18,09	73,52	16,86
	BH29-NM-09	Gabbronorite	55,60	44,40	44,28	55,72
	BH29-NM-10	Gabbronorite	88,73	11,27	78,69	21,31
	BH29-NM-11	Gabbronorite	98,17	1,83	96,57	3,43
	BH29-NM-12	Gabbronorite	90,56	9,44	80,71	19,29
Image 3	BH29-NM-13	Anorthosite	22,70	77,30	18,81	81,19
	BH29-NM-14	Anorthosite	4,68	95,32	3,88	96,12
	BH29-NM-15	Anorthosite	36,89	63,11	33,58	66,42
Image 4	BH29-NM-16	Orthopyroxenite	-	-	77,51	19,42
	BH29-NM-17	Pegmatitic pyroxenite	-	-	51,11	43,31
	BH29-NM-18	Orthopyroxenite	-	-	62,21	28,99
	BH29-NM-19	Chromitite	-	-	19,52 (62,76% Chromite)	17,72
	BH29-NM-20	Pyroxenite	-	-	93,69	5,79
	BH29-NM-21	leuco-norite	-	-	34,43	63,71
	BH29-NM-22	Mela-gabbronorite	-	-	88,59	11,07
	BH29-NM-23	Orthopyroxenite	-	-	94,32	5,63
	BH29-NM-24	Granitoid	-	-	38,45 (14,16% Chromite)	47,39
	BH29-NM-25	Chromitite	-	-	18,61 (48,64% Chromite)	32,75

5 Discussion

5.1 Grayscale histograms in lithological classification

The positively skewed histogram of pixel intensity distribution for chromitite indicates a dominance of darker pixels, characteristic of chromitite's low reflectance (Figure 4.10). This distribution reflects the visual and compositional contrast between the dark chromite crystals and the lighter pixels associated with minerals such as plagioclase and sulphides present in the sample. Hence, the training and validation chromitite samples differ in the proportion of dark and lighter crystals. Although the validation chromitite samples are positively skewed, they exhibit a broader range of values, which explains why 100% of the chromitite validation chromitite samples were unclassified rather than correctly classified as chromitite.

The contrast between dark pyroxene and light plagioclase minerals is important for visual interpretation but can influence classification accuracy, particularly when distinguishing between similar light-coloured lithologies with slight variations in mineral composition and texture. The broad pixel intensity range and prominent peak toward higher intensity values in the anorthosite pixel intensity distribution histogram reflect its high reflectance and light-toned appearance, primarily due to its modal composition of more than 90% plagioclase. 43% of the validation anorthosite samples were correctly classified as anorthosite, both training and validation anorthosite stands out with its consistently lighter pixel distribution, aiding in its visual differentiation (Figure 4.10).

Varying histogram distributions are expected for pyroxenite and gabbronorite, since according to Le Maitre (1984), occupy a wide compositional range defined by varying proportions of plagioclase and pyroxenes. The training pyroxenite and gabbronorite have a narrower intensity distributions indicating a relatively homogeneous composition, resulting in a more uniform appearance. In contrast, the validation pyroxenite and gabbronorite samples display broader intensity distributions, reflecting a wider compositional variability (Figure 4.11). This compositional variability is reflected in the classification results, where 0% of the validation gabbronorite samples were classified as gabbronorite and 19% fell within the overlapping gabbronorite-pyroxenite range. However, the pixel intensity distribution histogram shape and distribution for pyroxenite do not accurately represent its typical lithological characteristic of being dominated by dark crystals, due to the influence of the grayscale conversion algorithm. Hence, only 11.11% of the validation pyroxenite samples were correctly classified as pyroxenite, despite the dominance of dark pyroxene minerals that should yield a histogram

skewed toward lower intensity values. This inconsistency suggests that grayscale pixel intensity distribution histogram analysis alone is insufficient for distinguishing lithologies based on visual and compositional differences. The consistently lower standard deviation (SD) in the training data and higher SD in the validation data across all lithologies indicate that the training data are more uniform in pixel intensity, whereas the validation data are more heterogeneous, likely due to variability in texture, mineral composition, and illumination conditions (Figure 4.12).

The analysis of the individual red, green, and blue channels of the high-resolution RGB images reveals intensity peaks toward higher values within the pyroxenite R, G, and B channel histograms (Figure 5.1). Although pyroxenite appears dark in the original RGB image due to the abundance of dark green pyroxene minerals as well as gabbronorite dominated by mafic minerals, its elevated green reflectance becomes more pronounced in the grayscale image, and since the luminosity method applies a greater weighting to the green channel (0.587), the resulting grayscale image exhibits a shift toward lighter/higher pixel values. This accounts for the apparent discrepancy between the visual darkness of pyroxenite in the RGB image and its relative brightness in the grayscale histogram.

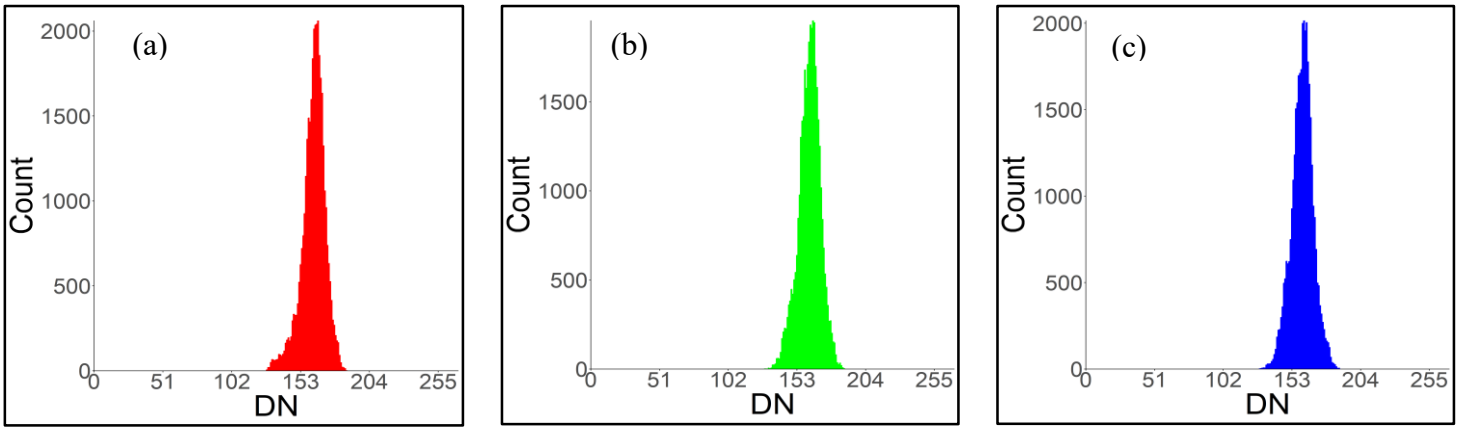

Figure 5.1: Pyroxenite individual Red (a), Green (b), Blue (c) channels of region 8 in training Image 4.

5.2 Mineral identification: spectral, geochemical, and petrographic analysis

Petrographic analysis identified orthopyroxene and plagioclase as the dominant minerals across all samples, with clinopyroxene occurring more in some gabbronorite and pyroxenites. The presence of orthopyroxene and plagioclase minerals in the mineral assemblage obtained from spectral analysis demonstrates a strong correlation between petrographic observations and spectral mineral identification, even with manual extraction of mineral spectra. This correlation is reinforced by the clearer identification of orthopyroxene and plagioclase in both methods and supported by a weak correlation between reference orthopyroxene (enstatite) and plagioclase. However, clinopyroxenes (augite), petrographically identified as oikocrysts hosting orthopyroxene chadacrysts in a porphyritic pyroxenite (image 4), were misclassified due to their strong spectral similarity with plagioclase, with a correlation coefficient of 0.85 between the two minerals in the reference USGS spectra (Table 4.5). This highlights the spectral correlation between these minerals and the challenges in distinguishing them using VNIR data alone. This may also explain why 40% of the pyroxenite samples in Image 4 contain over 90% pyroxene (mafic minerals) when mafic and felsic proportions were compared (Table 4.9), excluding the chromite-bearing pyroxenite, despite the overall high classification accuracy according to Appendix I.

The identification and classification of the major mineral classes such as enstatite, plagioclase, and chromite, in sampled rock types (Figure 5.2), are supported by petrographic analysis, which confirms the presence of orthopyroxene within gabbronorites and pegmatitic pyroxenite samples, plagioclase in all rock types, and chromite in chromitite layers. This reinforces the reliability of the extracted enstatite, plagioclase, and chromite spectral signatures. Furthermore, this supports the effectiveness of VNIR spectral data in detecting pyroxenes, as indicated in Table 2.1, particularly in relation to the distinct spectral absorption features associated with orthopyroxene.

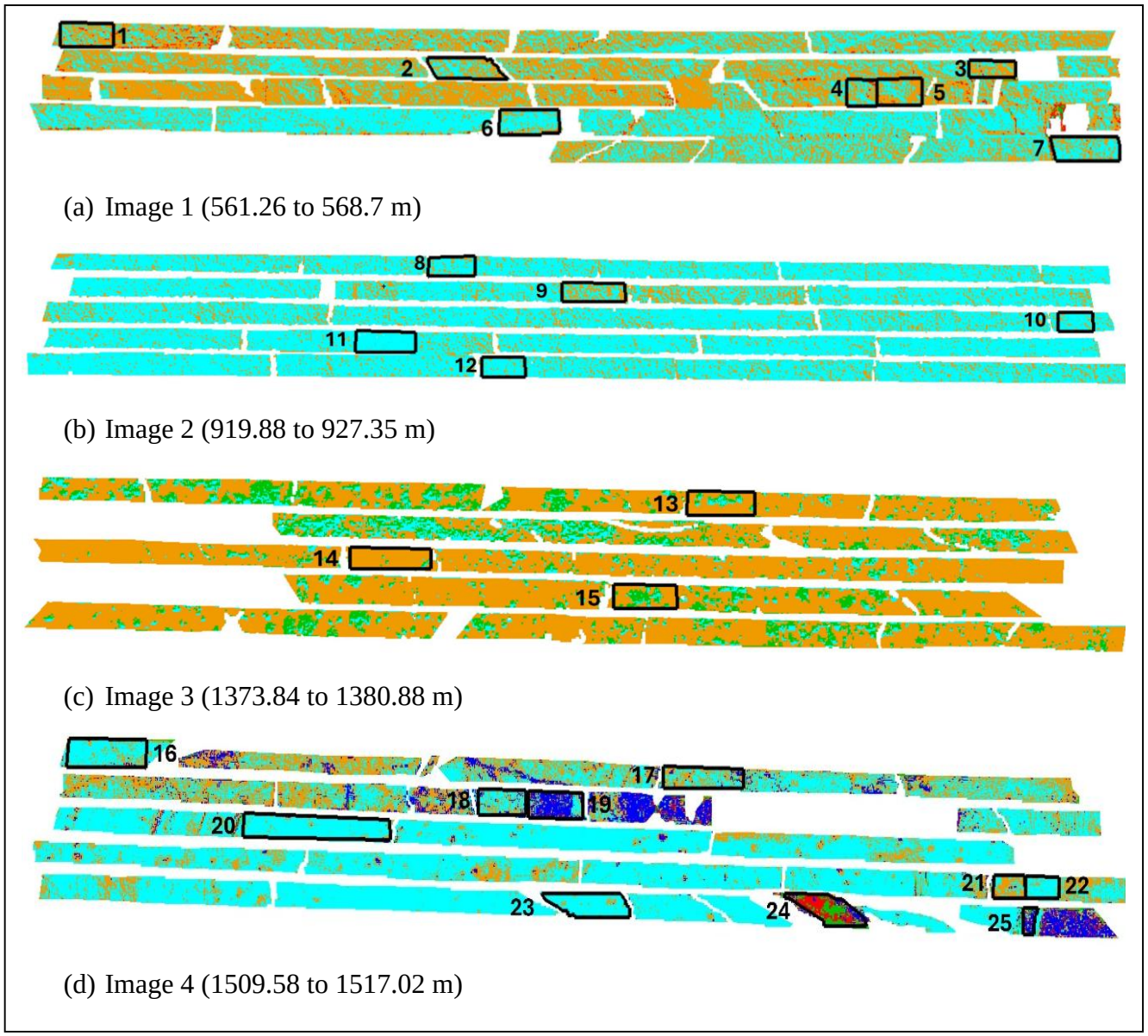

Figure 5.2: Comparison of the classification of sampled areas with the custom extracted spectral library from Images 4, Image 1 (561.26 to 568.7 m) classification results with sampled areas (a), Image 2 (919.88 to 927.35 m) classification results with sampled areas (b), Image 3 (1373.84 to 1380.88 m) classification results with sampled areas (c), and Image 4 (1509.58 to 1517.02 m) classification results with sampled areas (d). Orange (plagioclase), cyan (enstatite), green (alteration product), blue (chromite), and red (felsic mineral).

Loss of ignition (LOI) values greater than 2 wt.% in igneous rocks are commonly used as an indicator of alteration (Ghasempour *et al.*, 2020). In this study, four of the seven samples from Image 1 and one from Image 3 exceed this threshold, suggesting varying degrees of alteration. Petrographic analysis supports this, showing plagioclase alteration, primarily its replacement through saussuritization. Some samples, particularly from Image 1, exhibit extensive alteration, including complete mineral breakdown and micro-fracturing. This is consistent with the high

percentage of alteration captured when the image was classified using its spectra. The alteration likely reflects fluid-rock interaction, as evidenced by reduced Sr concentrations in altered anorthosite, indicative of Sr leaching because of its mobility (Hikov, 2004; Rollinson, 1993), and as part of the geochemical interpretation, strontium, Sr, a compatible trace element, was evaluated for its relationship with plagioclase content using the partitioning principle (Rollinson, 1993).

However, not all alteration minerals, such as albite and epidote, were represented in the extracted spectra, limiting classification accuracy. This is partly due to the spectral correlation between USGS reference albite, epidote, and calcium-rich plagioclase (labradorite) spectra that do not have clear, distinct absorption features, which are present alteration products in the RLS rocks from BH7929 (Figure 5.3). Although alteration minerals and plagioclase are generally distinguishable in the SWIR, including actinolite (Table 2.1) (Di Tommaso and Rubinstein, 2007; Mandende *et al.*, 2023), plagioclase and actinolite were successfully differentiated and classified in Image 1 in the VNIR from image-specific classification because of the clear difference between actinolite and plagioclase in the red band (668 nm) (Figure 4.20), which contributed to moderate accuracy (Appendix H).

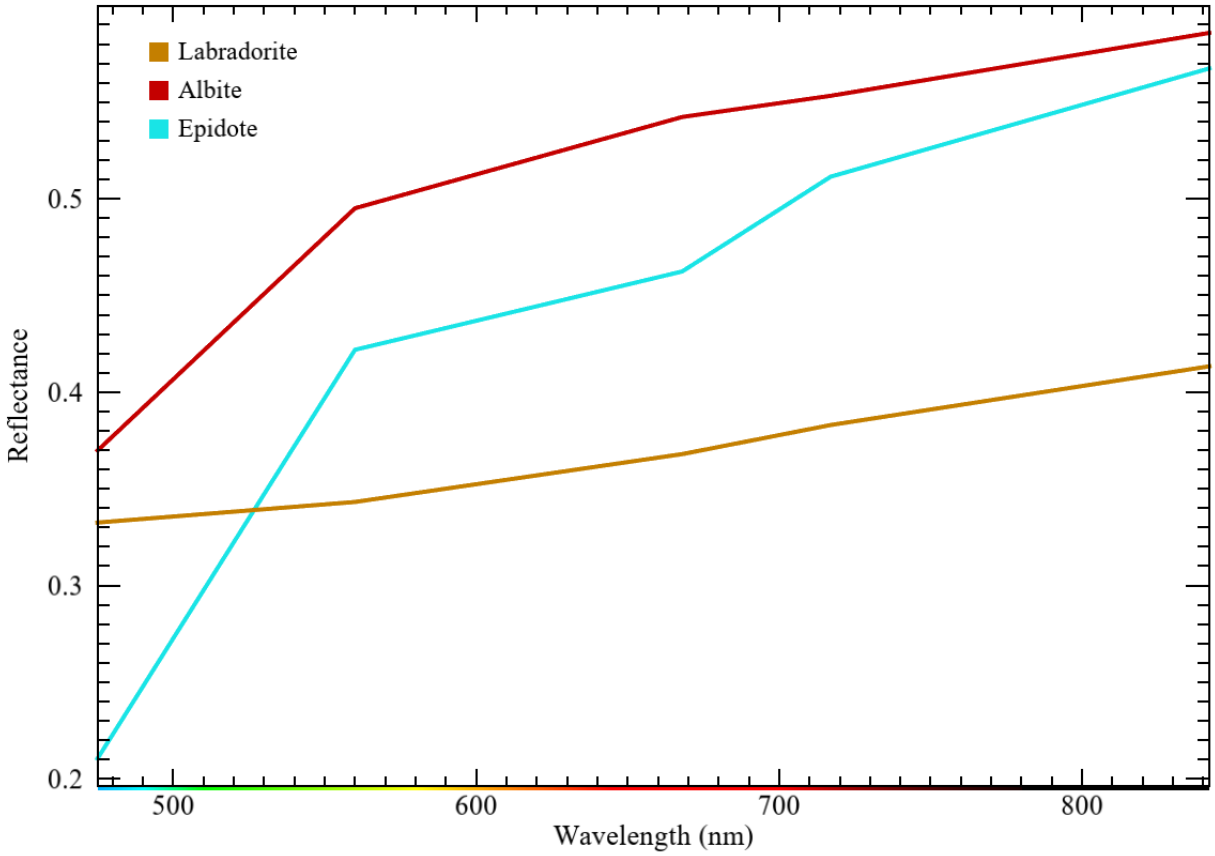

Figure 5.3: Spectra of USGS reference library, albite, epidote, and calcium-rich plagioclase (Labradorite).

5.3 Mineral classification using a custom spectral library

While the custom spectral library effectively classified the core image 4 from which the reference spectra were derived (Figure 4.15), its performance on other core sections remains comparable to manual logging and petrographic interpretation, showing similar patterns but also clear limitations. This prompted an assessment of the image-spectra classification approach, which subsequently improved the classification accuracies for Images 1-3 (Table 4.8).

These limitations stem from the inherent spectral variability in the limited bands studied, which the reference spectra may not fully capture. The VNIR custom spectral library can be used together with spectral correlations to identify potential overlapping mineral signatures. This includes assessing reflectance characteristics, such as the low reflectance of chromite and the higher reflectance of plagioclase, to apply reflectance thresholds thereby reducing misclassification of the drill-core. However, each of these minerals may still overlap with other minerals exhibiting similar high or low reflectance, which can introduce classification

challenges. Despite this, the approach reduces classification inaccuracy and enhances the library's applicability to new RLS core imagery, as demonstrated in Images 5-7 (Section 4.6.4).

Quantifying spectral similarity and integrating geochemistry and petrography is essential for evaluating the classification accuracy visually, where there is the presence of minerals with similar spectral features within a single core image such as plagioclase, felsic minerals, alteration product, and augite (Figure 4.13) (Appendix H). In addition, reference and extracted spectra do not represent discrete spectral classes but serve as comparative datasets, often leading to low classification accuracy when assessed with overall accuracy from the ENVI confusion matrix. This is supported by the absence of spectral pairs in the no-correlation range (Table 4.6) and no unclassified pixels from the classification, indicating that all compared spectra exhibit some degree of similarity.

The use of multiple classes for a single mineral in SAM classification captures spectral variability associated with mineral composition, chemistry, structure, grain size, and texture (Zhang and Li, 2014). This approach preserves important spectral detail that would otherwise be lost with a single mean spectrum, enhancing classification accuracy. Specifically, the use of multiple classes for plagioclase and enstatite improved the accuracy of SAM classifications. Understanding this spectral variability is essential for accurately interpreting and correlating spectral signatures of the mineral composition of RLS rocks.

6 Conclusions

In conclusion, high-resolution RGB-to-grayscale imagery demonstrates potential as a supplementary tool for classifying major lithologies rather than minerals of the RLS drill-core. The method effectively distinguishes chromitite from anorthosite through clear variability in the skewness of their grayscale pixel intensity distribution histograms. However, its ability to discriminate gabbronorite from pyroxenite is limited due to their broad compositional ranges and overlapping plagioclase-pyroxene mineralogy as reflected by the overlap between gabbronorite (19%) and pyroxenite (44%) validation sites within the gabbronorite-pyroxenite category. Furthermore, the weighting of the green band in grayscale conversion introduces artefacts by shifting darker pixels toward higher grayscale values, leading to the misinterpretation of dark minerals as light-coloured lithologies. These constraints limit the application of high-resolution RGB to grayscale imagery as a potential tool for classifying the lithologies and major minerals of the RLS drill-core.

The evaluation of multispectral imagery within the VNIR range (400-842 nm) for classifying the major minerals of the RLS in the BH7929 drill-core proved applicable, particularly where there are minerals with diagnostic features within the VNIR range and fewer minerals with non-diagnostic features within the VNIR region. This allows minerals with non-diagnostic features or similar spectral signatures, such as plagioclase and chromite, to be separately classified. Where this was not practical, overlapping minerals are identified and spectral correlations are quantified within the custom VNIR spectral library to enhance the interpretation of overlapping mineral signatures, thereby improving classification accuracy. The assessment of mafic and felsic minerals within the classified zones further supports this despite some samples falling outside the defined compositional ranges for their respective rock types. The results confirm a consistent trend where dark-coloured, mafic rocks are characterized by higher proportions of mafic minerals, whereas lighter-coloured, anorthositic rocks are dominated by felsic minerals.

Consequently, VNIR multispectral imaging emerges as a potential assistive tool to traditional core logging, particularly in large-scale mineral exploration projects involving thousands of metres of drill-core, where cost-effective and time-efficient solutions are essential. Additionally, machine learning models can be developed and trained using open-source platforms to enable the automated classification of RLS rocks from multispectral data, thereby

substantially accelerating data processing and enhancing the overall efficiency of exploration workflows.

Therefore, within mining operations, the implementation of these imaging techniques should be regarded as potentially advantageous for exploration and mining companies. Although RGB-to-grayscale imaging offers limited standalone applicability due to its restricted lithological classification, VNIR (400-842 nm) multispectral imaging provides meaningful insight when integrated into existing geological workflows. This approach is particularly beneficial for projects involving small-scale drill-core datasets, where rapid visualization and preliminary mineralogical classification can guide sampling by directing detailed examination toward zones of greater geological interest. In contrast, for larger-scale operations or deposits with well-characterized lithologies, the additional data processing demands and instrumentation requirements may outweigh the benefits. As a result, the value of these imaging methods depends on project scale, available resources, and the extent to which operational efficiency and data-driven decision-making are emphasized within exploration programs.

7 Recommendations

1. This work can be further enhanced through programming and machine learning to automate mineral classification of drill-core surfaces.
2. The identification of alteration minerals spectrally can be done using multispectral data in the SWIR range or with hyperspectral data covering broader regions of the electromagnetic spectrum.
3. Hyperspectral datasets can be integrated with quantitative XRD mineralogy to generate mineral abundance maps and estimate grades to support grade estimation through reflectance spectroscopy.

References

Acosta, I.C.C., Khodadadzadeh, M., Tusa, L., Ghamisi, P., Gloaguen, R., 2019. A Machine Learning Framework for Drill-Core Mineral mapping using hyperspectral and high-resolution mineralogical data fusion. IEEE J. Sel. Top. Appl. Earth Observations Remote Sensing 12, 4829–4842. https://doi.org/10.1109/JSTARS.2019.2924292

Adão, T., Hruška, J., Pádua, L., Bessa, J., Peres, E., Morais, R., Sousa, J., 2017. Hyperspectral Imaging: A review on UAV-based sensors, data processing, and applications for agriculture and forestry. Remote Sensing 9, 1110. https://doi.org/10.3390/rs9111110

Akoglu, H., 2018. User's guide to correlation coefficients. Turkish Journal of Emergency Medicine 18, 91–93. https://doi.org/10.1016/j.tjem.2018.08.001

Alzubaidi, F., Mostaghimi, P., Si, G., Swietojanski, P., Armstrong, R.T., 2022. Automated rock quality designation using convolutional neural networks. Rock Mech Rock Eng 55, 3719–3734. https://doi.org/10.1007/s00603-022-02805-y

Anthony, J.W., Bideaux, R.A., Bladh, K.W., Nichols, M.C., 2022. Handbook of Mineralogy. Mineralogical Society of America. http://www.handbookofmineralogy.org/

Asadzadeh, S., De Souza Filho, C.R., 2016. A review on spectral processing methods for geological remote sensing. International Journal of Applied Earth Observation and Geoinformation 47, 69–90. https://doi.org/10.1016/j.jag.2015.12.004

Baldridge, A.M., Hook, S.J., Grove, C.I., Rivera, G., 2009. The ASTER spectral library version 2.0. Remote Sensing of Environment 113, 711–715. https://doi.org/10.1016/j.rse.2008.11.007

Barjaktarovic, M., Santoni, M., Bruzzone, L., 2024. Design and verification of a low-cost multispectral camera for precision agriculture application. IEEE J. Sel. Top. Appl. Earth Observations Remote Sensing 17, 6945–6957. https://doi.org/10.1109/jstars.2024.3377104

Barnes, S.J. and Maier, W.D., 2002. Platinum-group element distributions in the Rustenburg layered suite of the Bushveld Complex, South Africa.

Biswas, D., Nag, A., Ghosh, S., Pal, Arindrajit, Biswas, S., Banerjee, S., Pal, Anjan, 2011. Novel gray scale conversion techniques based on pixel depth. Journal of Global Research in Computer Science, 2(6), 118-121. novel-gray-scale-conversion-techniques-based-on-pixel-depth-118-121-libre.pdf

Bobkowska, K., Burdziakowski, P., Tysiac, P., Pulas, M., 2024. An innovative new approach to light pollution measurement by drone. Drones 8, 504. https://doi.org/10.3390/drones8090504

Buckle, T., Williams, M., Nathwani, C.L., Hughes, H.S.R., 2023. WebNORM: a web application for calculating normative mineralogy. Front. Earth Sci. 11, 1232256. https://doi.org/10.3389/feart.2023.1232256

Canter, G., Sheairs, J., Kreckie, J., Menezes, S., Schreuder, E. and Roberts, M., 2023. Evaluation of unmanned aircraft systems for aircraft accident and incident scene documentation (No. DOT/FAA/TC-23/79). United States. Department of Transportation. Federal Aviation Administration. William J. Hughes Technical Center.

Cawthorn, R.G., 2006. Origin of the pegmatitic pyroxenite in the Merensky Unit, Bushveld Complex, South Africa. Journal of Petrology 47, 1509–1530. https://doi.org/10.1093/petrology/egl017

Chabrillat, S., Foerster, S., Segl, K., Beamish, A., Brell, M., Asadzadeh, S., Milewski, R., Ward, K.J., Brosinsky, A., Koch, K., Scheffler, D., Guillaso, S., Kokhanovsky, A., Roessner, S., Guanter, L., Kaufmann, H., Pinnel, N., Carmona, E., Storch, T., Hank, T., Berger, K., Wocher, M., Hostert, P., Van Der Linden, S., Okujeni, A., Janz, A., Jakimow, B., Bracher, A., Soppa, M.A., Alvarado, L.M.A., Buddenbaum, H., Heim, B., Heiden, U., Moreno, J., Ong, C., Bohn, N., Green, R.O., Bachmann, M., Kokaly, R., Schodlok, M., Painter, T.H., Gascon, F., Buongiorno, F., Mottus, M., Brando, V.E., Feilhauer, H., Betz, M., Baur, S., Feckl, R., Schickling, A., Krieger, V., Bock, M., La Porta, L., Fischer, S., 2024. The EnMAP spaceborne imaging spectroscopy mission: Initial scientific results two years after launch. Remote Sensing of Environment 315, 114379. https://doi.org/10.1016/j.rse.2024.114379

Charlier, B. and Zellmer, G., 2000. Some remarks on U–Th mineral ages from igneous rocks with prolonged crystallisation histories. Earth and Planetary Science Letters, 183(3-4), 457-469. https://doi.org/10.1016/S0012-821X(00)00298-3

Clark, R.N., Swayze, G.A., Livo, K.E., Kokaly, R.F., King, T.V., Dalton, J.B., Vance, J.S., Rockwell, B.W., Hoefen, T. and McDougal, R.R., 2002, March. Surface reflectance calibration of terrestrial imaging spectroscopy data: a tutorial using AVIRIS. In Proceedings of the 10th airborne earth science workshop (Vol. 2). Pasadena, CA, USA: Jet Propulsion Laboratory. https://aviris.jpl.nasa.gov/proceedings/workshops/02_docs/2002_Clark_web.pdf

Coertze, F.J., Burger, A.J., Walraven, F., Marlow, A.G., and MacCaskie, D., 1978. Field relations and age determinations in the Bushveld Complex. South African Journal of Geology, 81(1), 1-11. https://journals.co.za/doi/pdf/10.10520/AJA10120750_2831

Cross, W., Iddings, J.P., Pirsson, L.V. and Washington, H.S., 1902. A quantitative chemico-mineralogical classification and nomenclature of igneous rocks. The Journal of Geology, 10(6), 555-690. https://doi.org/10.1016/j.jag.2011.08.002

De La Rosa, R., Khodadadzadeh, M., Tusa, L., Kirsch, M., Gisbert, G., Tornos, F., Tolosana-Delgado, R., Gloaguen, R., 2021. Mineral quantification at deposit scale using drill-core hyperspectral data: A case study in the Iberian Pyrite Belt. Ore Geology Reviews 139, 104514. https://doi.org/10.1016/j.oregeorev.2021.104514

Di Tommaso, I., Rubinstein, N., 2007. Hydrothermal alteration mapping using ASTER data in the Infiernillo porphyry deposit, Argentina. Ore Geology Reviews 32, 275–290. https://doi.org/10.1016/j.oregeorev.2006.05.004

Dorador, J. and Rodríguez-Tovar, F.J., 2016. High-resolution digital image treatment to color analysis on cores from IODP Expedition 339: approaching lithologic features and bioturbational influence. Marine Geology, 377, 127-135. https://doi.org/10.1016/j.margeo.2016.02.005

EagleNXT, 2021. *EagleNXT* [online]. Available at: https://ageagle.com/resources/?filter_by=use-case&options=rededge-p (Accessed May 2024)

Eales, H.V. and Cawthorn, R.G., 1996. The Bushveld Complex. In: R.G. Cawthorn (ed.) Layered Intrusions. Amsterdam: Elsevier Science B.V., 181–229

Fu, D., Su, C., Li, X., 2024. Automatic Estimation Of Rock Quality Designation Based On An Improved YOLOv5. Rock Mech Rock Eng. https://doi.org/10.1007/s00603-023-03729-x

Fu, D., Su, C., Wang, W., Yuan, R., 2022. Deep learning based lithology classification of drill-core images. PLoS ONE 17, e0270826. https://doi.org/10.1371/journal.pone.0270826

Galdames, F.J., Perez, C.A., Estévez, P.A., Adams, M., 2019. Rock lithological classification by hyperspectral, range 3D and color images. Chemometrics and Intelligent Laboratory Systems 189, 138–148. https://doi.org/10.1016/j.chemolab.2019.04.006

Ghasempour, M.R., Davoudian, A.R., Shabanian, N., Moeinzadeh, H., Nakashima, K., 2020. Geochemistry and mineral chemistry of gabbroic rocks from Horjand of Kerman province, Southeast of Iran: Implications for rifting along the northeastern margin of Gondwana. Journal of Geodynamics 133, 101675. https://doi.org/10.1016/j.jog.2019.101675

Goetz, A.F. and Rowan, L.C., 1981. Geologic remote sensing. Science, 211(4484), 781-79. doi:10.1126/science.211.4484.781

Grobler, D.F., Brits, J.A.N., Maier, W.D., Crossingham, A., 2019. Litho- and chemostratigraphy of the Flatreef PGE deposit, northern Bushveld Complex. Miner Deposita 54, 3–28. https://doi.org/10.1007/s00126-018-0800-x

Grove, T.L. and Brown, S.M., 2018. Magmatic processes leading to compositional diversity in igneous rocks: Bowen (1928) revisited. American Journal of Science, 318(1), 1-28. doi 10.2475/01.2018.02

Hasan, E., Fagin, T., El Alfy, Z., Hong, Y., 2016. Spectral Angle Mapper and aeromagnetic data integration for gold-associated alteration zone mapping: a case study for the Central Eastern Desert Egypt. International Journal of Remote Sensing 37, 1762–1776. https://doi.org/10.1080/01431161.2016.1165887

Hikov, A., 2004. Geochemistry of strontium in advanced argillic alteration systems–possible guide to exploration. *Geology*, 16-17.

Irvine, T.N., 1982. Terminology for layered intrusions. Journal of Petrology 23, 127–162. https://doi.org/10.1093/petrology/23.2.127-a

Jakob, S., Zimmermann, R., Gloaguen, R., 2017. The need for accurate geometric and radiometric corrections of drone-borne hyperspectral data for mineral exploration: MEPHySTo, A Toolbox for Pre-Processing Drone-Borne Hyperspectral Data. Remote Sensing 9, 88. https://doi.org/10.3390/rs9010088

Jyothi, G., Sushma, C., Veeresh, D.S.S., 2015. Luminance based conversion of gray scale image to RGB Image 3. *International Journal of Computer Science and Information Technology Research*, 3(3), 279–283.

Keet, J.J., Roelofse, F., Gauert, C.D.K., Iaccheri, L.M., Grobler, D.F., Ueckermann, H., 2024. Neodymium isotope variations in the Flatreef on Macalacaskop, northern limb, Bushveld Complex. Miner Deposita 59, 275–290. https://doi.org/10.1007/s00126-023-01202-x

Kelsey, C.H., 1965. Calculation of the CIPW norm. *Mineralogical magazine and journal of the Mineralogical Society*, *34* (268), 276-282.

Khaleghi, M., Ranjbar, H., Shahabpour, J., Honarmand, M., 2014. Spectral angle mapping, spectral information divergence, and principal component analysis of the ASTER SWIR data for exploration of porphyry copper mineralization in the Sarduiyeh area, Kerman province, Iran. Appl Geomat 6, 49–58. https://doi.org/10.1007/s12518-014-0125-0

Kirsch, M., Mavroudi, M., Thiele, S., Lorenz, S., Tusa, L., Booysen, R., Herrmann, E., Fatihi, A., Möckel, R., Dittrich, T. and Gloaguen, R., 2023. Underground hyperspectral outcrop scanning for automated mine-face mapping: The lithium deposit of Zinnwald/Cínovec. The Photogrammetric Record, 38(183), 408-429.

Kokaly, R.F., Clark, R.N., Swayze, G.A., Livo, K.E., Hoefen, T.M., Pearson, N.C., Wise, R.A., Benzel, W., Lowers, H.A., Driscoll, R.L. and Klein, A.J., 2017. *USGS spectral library version 7* (No. 1035). US Geological Survey. https://pubs.usgs.gov/ds/1035/ds1035.pdf

Kruse, F.A., Bedell, R.L., Taranik, J.V., Peppin, W.A., Weatherbee, O., Calvin, W.M., 2012. Mapping alteration minerals at prospect, outcrop and drill-core scales using imaging spectrometry. International Journal of Remote Sensing 33, 1780–1798. https://doi.org/10.1080/01431161.2011.600350

Laliberte, A.S., Goforth, M.A., Steele, C.M., Rango, A., 2011. Multispectral remote sensing from unmanned aircraft: image processing workflows and applications for rangeland environments. Remote Sensing 3, 2529–2551. https://doi.org/10.3390/rs3112529

Le Bas, M.J. and Streckeisen, A.L., 1991. The IUGS systematics of igneous rocks. Journal of the Geological Society, 148(5), 825-833. https://doi.org/10.1144/gsjgs.148.5.0825

Le Maitre, R.W., 1984. A proposal by the IUGS Subcommission on the Systematics of Igneous Rocks for a chemical classification of volcanic rocks based on the total alkali silica (TAS) diagram: (on behalf of the IUGS Subcommission on the Systematics of Igneous Rocks). Australian Journal of Earth Sciences 31, 243–255. https://doi.org/10.1080/08120098408729295

Li, C., Ripley, E.M., Sarkar, A., Shin, D., Maier, W.D., 2005. Origin of phlogopite-orthopyroxene inclusions in chromites from the Merensky Reef of the Bushveld Complex, South Africa. Contrib Mineral Petrol 150, 119–130. https://doi.org/10.1007/s00410-005-0013-z

Liu, X., Yang, C., 2013. A kernel spectral angle mapper algorithm for remote sensing image classification, in: 2013 6th International Congress on Image and Signal Processing (CISP). Presented at the 2013 6th International Congress on Image and Signal Processing (CISP), IEEE, Hangzhou, China, 814–818. https://doi.org/10.1109/CISP.2013.6745277

Maier, W.D., Barnes, S.J., Godel, B.M., Grobler, D., Smith, W.D., 2023. Petrogenesis of thick, high-grade PGE mineralisation in the Flatreef, northern Bushveld Complex. Miner Deposita 58, 881–902. https://doi.org/10.1007/s00126-022-01156-6

Mandende, H., Ndou, C., Mothupi, T., 2023. Hyperspectral core scanner: An effective mineral mapping tool for apatite in the Upper Zone, northern limb, Bushveld Complex. J. S. Afr. Inst. Min. Metall. 123, 81–92. https://doi.org/10.17159/2411-9717/1890/2023

Markgraaff, J., 1976. Pyroxenes of the western Bushveld complex, South Africa. South African Journal of Geology, 79(2), 217-224. https://journals.co.za/doi/pdf/10.10520/AJA10120750_2861

Markogianni, V., Kalivas, D., Petropoulos, G.P., Dimitriou, E., 2020. Estimating chlorophyll-a of Inland Water Bodies in Greece Based on Landsat Data. Remote Sensing 12, 2087. https://doi.org/10.3390/rs12132087

McDonald, I., Holwell, D.A., Armitage, P.E.B., 2005. Geochemistry and mineralogy of the Platreef and "Critical Zone" of the northern lobe of the Bushveld Complex, South Africa: implications for Bushveld stratigraphy and the development of PGE mineralisation. Miner Deposita 40, 526–549. https://doi.org/10.1007/s00126-005-0018-6

Meima, J.A., Rammlmair, D., 2020. Investigation of compositional variations in chromitite ore with imaging Laser Induced Breakdown Spectroscopy and Spectral Angle Mapper classification algorithm. Chemical Geology 532, 119376. https://doi.org/10.1016/j.chemgeo.2019.119376

Merino, L., Caballero, F., Martínez-de-Dios, J.R., Maza, I., Ollero, A., 2012. An Unmanned Aircraft System for automatic forest fire monitoring and measurement. J Intell Robot Syst 65, 533–548. https://doi.org/10.1007/s10846-011-9560-x

MicaSense, 2017. *RedEdge-M user manual*. [pdf] MicaSense, Inc. Available at: https://support.micasense.com (Accessed February 2024)

MicaSense, 2023. *The importance of radiometric calibration*. [online] Available at: https://support.micasense.com/hc/en-us/articles/115002327753-The-Importance-of-Radiometric-Calibration (Accessed May 2024)

MicaSense, 2024. *How to use the Calibrated Reflectance Panel (CRP)*. [online] 04 April 2024. Available at: https://support.micasense.com/hc/en-us/articles/1500001975662-How-to-use-the-Calibrated-Reflectance-Panel-CRP (Accessed May 2024)

Minerals Council South Africa, 2023. *SA's mining companies are creating value and discovering the future world of work as their digital journeys mature.* Available at: https://www.mineralscouncil.org.za (Accessed July 2025)

Murphy, R.J., Monteiro, S.T., 2013. Mapping the distribution of ferric iron minerals on a vertical mine face using derivative analysis of hyperspectral imagery (430–970nm). ISPRS Journal of Photogrammetry and Remote Sensing 75, 29–39. https://doi.org/10.1016/j.isprsjprs.2012.09.014

Nederbragt, A.J., Dunbar, R.B., Osborn, A.T., Palmer, A., Thurow, J.W., Wagner, T., 2006. Sediment colour analysis from digital images and correlation with sediment composition. SP 267, 113–128. https://doi.org/10.1144/GSL.SP.2006.267.01.08

Nesse, W., D., 2009. *Introduction to optical mineralogy*. (2009 International ed.). Oxford University Press. 364

Ninomiya, Y., Fu, B., 2019. Thermal infrared multispectral remote sensing of lithology and mineralogy based on spectral properties of materials. Ore Geology Reviews 108, 54–72. https://doi.org/10.1016/j.oregeorev.2018.03.012

Ninomiya, Y., Fu, B., Cudahy, T.J., 2005. Detecting lithology with Advanced Spaceborne Thermal Emission and Reflection Radiometer (ASTER) multispectral thermal infrared "radiance-at-sensor" data. Remote Sensing of Environment 99, 127–139. https://doi.org/10.1016/j.rse.2005.06.009

Novais, J.J., Lacerda, M.P.C., Sano, E.E., Demattê, J.A.M., Oliveira, M.P., 2021. Digital Soil Mapping Using Multispectral Modeling with Landsat Time Series Cloud Computing Based. Remote Sensing 13, 1181. https://doi.org/10.3390/rs13061181

Ollila, J.T., 1986. Origin of colour zoning in cassiterites from tin deposits within the Bushveld Complex, South Africa. Bull Geol Soc Finland 58, 3–11. https://doi.org/10.17741/bgsf/58.2.001

Philpotts, A.R. and Ague, J.J., 2009. *Principles of igneous and metamorphic petrology*. Cambridge University Press.

Plaza, A., Martinez, P., Perez, R., Plaza, J., 2004. A quantitative and comparative analysis of endmember extraction algorithms from hyperspectral data. IEEE Trans. Geosci. Remote Sensing 42, 650–663. https://doi.org/10.1109/TGRS.2003.820314

Qasim, M., Khan, S.D., Haider, R., Rasheed, M.U., 2022. Integration of multispectral and hyperspectral remote sensing data for lithological mapping in Zhob Ophiolite, Western Pakistan. Arab J Geosci 15, 599. https://doi.org/10.1007/s12517-022-09788-8

Ragland, P.C., Conley, J.F., Parker, W.C., Von Orman, J.A., 1997. Use of principal components analysis in petrology: an example from the Martinsville igneous complex, Virginia, USA. *Mineralogy and Petrology*, *60*(3), 165-184.

Rahmat, F., Zulkafli, Z., Ishak, A.J., Abdul Rahman, R.Z., Stercke, S.D., Buytaert, W., Tahir, W., Ab Rahman, J., Ibrahim, S. and Ismail, M., 2023. Supervised feature selection using principal component analysis. *Knowledge and Information Systems*, *66*(3), 1955-1995. https://doi.org/10.1007/s10115-023-01993-5

Roelofse, F. and Ashwal, L.D., 2012. The Lower Main Zone in the Northern Limb of the Bushveld Complex — a > 1· 3 km thick sequence of intruded and variably contaminated crystal mushes. Journal of Petrology, 53(7), 1449-1476. https://doi.org/10.1093/petrology/egs022

Roelofse, F., Ashwal, L.D., Pineda-Vargas, C.A., Przybylowicz, W.J., 2009. Enigmatic textures developed along plagioclase-augite grain boundaries at the base of the Main Zone, Northern Limb, Bushveld Complex - evidence for late-stage melt infiltration into a nearly solidified crystal mush. South African Journal of Geology 112, 39-46. https://doi.org/10.2113/gssajg.112.1.39

Roelofse, F., Magson, J., Nicholson, M., Nyakane, T., 2024. A high-resolution geochemical and petrological investigation of bifurcating chromitite layers of the UG1 footwall at Impala Platinum Mine, Rustenburg. The Canadian Journal of Mineralogy and Petrology 62, 713-730. https://doi.org/10.3749/2300068

Rollinson, H.R., 1993. *Using geochemical data: evaluation, presentation, interpretation*. Harlow: Longman Scientific & Technical; New York: J. Wiley & Sons. 13–35.

Routh, D., Seegmiller, L., Bettigole, C., Kuhn, C., Oliver, C.D., Glick, H.B., 2018. Improving the reliability of mixture tuned matched filtering remote sensing classification results using supervised learning algorithms and cross-validation. Remote Sensing 10, 1675. https://doi.org/10.3390/rs10111675

Sadeghi, M., Morris, G.A., Carranza, E.J.M., Ladenberger, A. and Andersson, M., 2013. Rare earth element distribution and mineralization in Sweden: an application of principal component analysis to FOREGS soil geochemistry. *Journal of geochemical exploration*, *133*, 160-175. http://dx.doi.org/10.1016/j.gexplo.2012.10.015

Santos, D., Nogueira, A., Cardoso-Fernandes, J., Lima, A., Teodoro, A.C., 2024. Endmember extraction for lct pegmatite detection in brazil – A new approach for greenfield prospection using hyperspectral data, in: IGARSS 2024 - 2024 IEEE International Geoscience and Remote Sensing Symposium. Presented at the IGARSS 2024 - 2024 ieee international geoscience and remote sensing symposium, IEEE, Athens, Greece, 7724–7728. https://doi.org/10.1109/IGARSS53475.2024.10641084

Schaepman-Strub, G., Schaepman, M.E., Martonchik, J., Painter, T. and Dangel, S., 2009. Radiometry and reflectance: From terminology concepts to measured quantities. The SAGE Handbook of Remote Sensing, 215-228. https://doi.org/10.1016/j.rse.2006.03.002

Scoates, J.S., Wall, C.J., 2015. Geochronology of layered intrusions, in: Charlier, B., Namur, O., Latypov, R., Tegner, C. (Eds.), Layered Intrusions, Springer Geology. Springer Netherlands, Dordrecht, 3–74. https://doi.org/10.1007/978-94-017-9652-1_1

Scoates, J.S., Wall, C.J., Friedman, R.M., Weis, D., Mathez, E.A., VanTongeren, J.A., 2021. Dating the Bushveld Complex: Timing of crystallization, duration of magmatism, and cooling of the world's largest layered intrusion and related rocks. Journal of Petrology 62, egaa107. https://doi.org/10.1093/petrology/egaa107

Shukla, A., Kot, R., 2016. An overview of hyperspectral remote Sensing and its applications in various Disciplines. IRA-JAS 5, 85. https://doi.org/10.21013/jas.v5.n2.p4

Simpson, J., Davies, K.P., Barber, P., Bruce, E., 2024. Mapping fine-scale seagrass disturbance using bi-temporal UAV-acquired images and multivariate alteration detection. Sci Rep 14. https://doi.org/10.1038/s41598-024-69695-8

Smith, W.D., Maier, W.D., Muir, D.D., Andersen, J.C.Ø., Williams, B.J., Henry, H., 2023. New perspectives on the formation of the Boulder Bed of the western Bushveld Complex, South Africa. Miner Deposita 58, 617–638. https://doi.org/10.1007/s00126-022-01150-y

Staniszewski, R., Messyasz, B., Dąbrowski, P., Burdziakowski, P., Spychała, M., 2024. Recent issues and challenges in the study of inland waters. Water 16, 1216. https://doi.org/10.3390/w16091216

Stanley, C., 2017. Lithogeochemical classification of igneous rocks using Streckeisen ternary diagrams. GEEA 17, 63–91. https://doi.org/10.1144/geochem2016-463

Streckeisen, A., 1976. *To each plutonic rock its proper name*. *Earth-Science Reviews*, 12(1), 1–33.

Sui, Y., Jiang, R., Liu, Y., Zhang, X., Lin, N., Zheng, X., Li, B., Yu, H., 2025. Predicting the spatial distribution of soil salinity based on multi-temporal multispectral images and environmental covariates. Computers and Electronics in Agriculture 231, 109970. https://doi.org/10.1016/j.compag.2025.109970

Tappert, M., Rivard, B., Giles, D., Tappert, R., Mauger, A., 2011. Automated drill-core logging using visible and near-infrared reflectance spectroscopy: a case study from the Olympic Dam iocg deposit, South Australia. Economic Geology 106, 289–296. https://doi.org/10.2113/econgeo.106.2.289

Turner, D., Lucieer, A. and Watson, C., 2011, April. Development of an Unmanned Aerial Vehicle (UAV) for hyper-resolution vineyard mapping based on visible, multispectral, and thermal imagery. In Proceedings of 34th International symposium on remote sensing of environment (Vol. 4). 211104015Final00547.pdf

Tysiąc, P., Moskalewicz, D., Janowski, Ł., 2025. Development of UAV-based LiDAR and multispectral measurement techniques for monitoring sediment intrusion in coastal wetlands. Measurement 253, 117459. https://doi.org/10.1016/j.measurement.2025.117459

Van der Meer, F.D., Van der Werff, H.M., Van Ruitenbeek, F.J., Hecker, C.A., Bakker, W.H., Noomen, M.F., Van Der Meijde, M., Carranza, E.J.M., De Smeth, J.B. and Woldai, T., 2012. Multi-and hyperspectral geologic remote sensing: A review. International journal of applied Earth observation and geoinformation, 14(1), 112-128.

Vuletić, J., Car, M., Orsag, M., 2023. Close-range multispectral imaging with Multispectral-Depth (MS-D) system. Biosystems Engineering 231, 178–194. https://doi.org/10.1016/j.biosystemseng.2023.06.002

Wager, L.R. and Brown, G.M., 1953. Layered intrusions. Medd. Dansk. geol. Foren, 335-349. https://2dgf.dk/xpdf/bull-1953-12-3-335-349.pdf

Wager, L.R., Brown, G.M. and Wadsworth, W.J., 1960. Types of igneous cumulates. Journal of Petrology, 1(1), 73-85. https://doi.org/10.1093/petrology/1.1.73

Walraven, F., Armstrong, R.A. and Kruger, F.J., 1990. A chronostratigraphic framework for the north-central Kaapvaal craton, the Bushveld Complex and the Vredefort structure. Tectonophysics, 171(1-4), 23-48. https://doi.org/10.1016/0040-1951(90)90088-P

Wiącek, P., 2020. The database for multifactorial UAV accuracy assessments. Int. Arch. Photogramm. Remote Sens. Spatial Inf. Sci. XLIII-B5-2020, 163–172. https://doi.org/10.5194/isprs-archives-XLIII-B5-2020-163-2020

Yonezawa, C., 2007. Maximum likelihood classification combined with spectral angle mapper algorithm for high resolution satellite imagery. International Journal of Remote Sensing 28, 3729–3737. https://doi.org/10.1080/01431160701373713

Zhang, X., Li, P., 2014. Lithological mapping from hyperspectral data by improved use of spectral angle mapper. International Journal of Applied Earth Observation and Geoinformation 31, 95–109. https://doi.org/10.1016/j.jag.2014.03.007

Zumsprekel, H. and Prinz, T., 2000. Computer-enhanced multispectral remote sensing data: a useful tool for the geological mapping of Archean terrains in (semi) arid environments. Computers & Geosciences, 26(1), 87-100. https://doi.org/10.1016/S0098-3004(99)00042-4

Zwinkels, J., 2015. Light, electromagnetic spectrum, in: Luo, R. (Ed.), Encyclopedia of Color Science and Technology. Springer Berlin Heidelberg, Berlin, Heidelberg, 1–8. https://doi.org/10.1007/978-3-642-27851-8_204-1

Appendices

Appendix A

Table A1: Logging table for Images 1 and 2

Depth From (m)	Depth To (m)	Thickness (m)	Lithology
Image 1			
561,26	562,85	1,59	Medium-crystalline, dark gray to gray, moderately spotted, minor fractures, **spotted anorthosite**
562,85	563,21	0,37	Medium-crystalline, gray, bleaching of dark minerals, **mottled anorthosite**
563,21	563,43	0,22	Medium-crystalline, dark gray to gray, moderately spotted, spotted anorthosite
563,43	565,15	1,71	Medium-crystalline, gray, bleaching of dark minerals, some sections seem to be altered or serpentinised, **mottled anorthosite**
565,15	565,23	0,08	Medium-crystalline, gray, moderately spotted, **spotted anorthosite**
565,23	565,48	0,25	Fine-medium crystalline, gray, evidence of serpentinisation with a bladed greenish mineral, **Pyroxenite**
565,48	565,52	0,04	Medium-crystalline, gray, **anorthosite**
565,52	567,29	1,77	Medium-crystalline, dark-gray to brownish gray, fractured, **norite**
567,29	567,33	0,05	Fine-medium crystalline, dark-gray, **pyroxenite**
567,33	567,69	0,36	Fine- medium crystalline, dark-gray to brownish gray, **norite**
567,69	567,73	0,04	Fine-medium crystalline, dark-gray, **pyroxenite**
567,73	568,70	0,97	Fine- medium crystalline, dark-gray to brownish gray, **norite**
Image 2			
919,88	921,41	1,53	Fine-medium crystalline, dark brownish-gray, **gabbronorite**
921,41	922,86	1,45	Medium-coarse crystalline, gray-light gray, anorthositic patches, **gabbronorite**
922,86	924,36	1,50	Medium-coarse crystalline, brownish gray-light gray, **gabbronorite**
924,36	925,83	1,47	Fine-medium-crystalline, brownish gray- gray, **gabbronorite**
925,83	927,35	1,52	Fine-medium crystalline, gray-light gray, **gabbronorite**

Table A2: Logging table for images 3 and 4

Depth From (m)	Depth To (m)	Thickness (m)	Lithology
Image 3			
1373,84	1375,20	1,36	Medium-coarse crystalline, light gray, moderately spotted, bleaching of dark minerals, **mottled anorthosite**
1375,20	1376,69	1,49	Medium-coarse crystalline, light gray, moderately spotted, medium to large spots, **spotted anorthosite**
1376,69	1378,02	1,33	Medium-crystalline, whitish-gray, highly spotted with small spots, **spotted anorthosite**
1378,02	1379,52	1,49	Medium-crystalline, light gray, highly spotted with small spots, **spotted anorthosite**
1379,52	1380,88	1,36	Medium-crystalline, light gray to gray, moderately spotted, medium to large spots, **spotted anorthosite**
Image 4			
1509,58	1510,37	0,79	Medium-crystalline, gray to greenish brown stains of iron, **pyroxenite**
1510,37	1510,71	0,34	Coarse-crystalline, whitish plagioclase, **pegmatoid**
1510,71	1511,04	0,33	Medium-crystalline, brownish gray, **pyroxenite**
1511,04	1511,51	0,47	Medium-crystalline, red brown to yellow-brownish stains, **pyroxenite**
1511,51	1511,69	0,18	Coarse-crystalline, whitish plagioclase, **pegmatoid**
1511,69	1511,76	0,07	Fine crystalline, black, **chromitite layer**
1511,76	1511,84	0,08	Medium-crystalline, brownish-gray, whitish phenocrysts, disseminated chromite, **pyroxenite**
1511,84	1511,96	0,12	Fine crystalline, black with whitish phenocrysts, **chromitite layer**
1511,96	1512,15	0,19	Medium-crystalline, greenish brown stains of iron, pyroxenite
1512,15	1512,17	0,02	Very-fine crystalline, black, **chromitite layer**
1512,17	1512,41	0,24	Highly fractured [cut out]
1512,41	1512,87	0,46	Fine-crystalline, greenish brown, with thin chromitite layering, **Pyroxenite**
1512,87	1515,17	2,30	Fine-crystalline, greenish brown to brownish-gray, with greenish phenocrysts, **Pyroxenite**
1515,17	1515,35	0,18	Medium-crystalline, white-brownish, **Anorthosite**
1515,35	1515,40	0,05	Medium-crystalline, brown, with phenocrysts, **Pyroxenite**
1515,40	1515,76	0,36	Medium-crystalline, white-brownish, **Anorthosite**
1515,76	1516,54	0,78	Medium-crystalline, brownish gray, with greenish phenocrysts, **Pyroxenite**
1516,54	1516,91	0,37	Fine-crystalline, greenish-brown, Pyroxenite with a reddish brown pegmatoid at 50°
1516,91	1517,07	0,16	Very-fine crystalline, black, with ~5 mm pyroxenite layer, **Chromitite layer**

Table A3: Logging table for images 5 to 7.

Depth From (m)	**Depth To (m)**	**Thickness (m)**	**Lithology**
Image 5			
576,09	577,51	1,42	Coarse-crystalline, gray, **gabbronorite**
577,51	578,98	1,48	Coarse-crystalline, light gray to gray, **gabbronorite**
578,98	580,00	1,02	Coarse-crystalline, gray, **gabbronorite**
580,00	580,49	0,49	Coarse-crystalline, gray, **gabbronorite**
580,49	582,03	1,54	Coarse-crystalline, gray, **gabbronorite**
582,03	583,45	1,42	Coarse-crystalline, light gray to gray, **gabbronorite**
Image 6			
1402,83	1403,98	1,15	Medium-crystalline, green- dark green, **pyroxenite**
1403,98	1404,00	0,02	Black, fine crystalline, **chromitite layer**
1403,98	1404,60	0,62	White to light gray, medium-crystalline, small to large mottles, serpentinised, **mottled anorthosite**
1404,73	1405,07	0,34	White to light gray, medium-crystalline, small to large mottles, fractured, **mottled anorthosite**
1405,25	1405,84	0,59	Light gray, medium-crystalline, small to large mottles, **mottled anorthosite**
1405,84	1406,92	1,08	White to light gray, medium-crystalline, small to large mottles, serpentinised, **mottled anorthosite**
1406,92	1407,37	0,45	Gray to light gray, medium crystalline, densely populated spots, **spotted anorthosite**
1407,37	1408,79	1,42	Gray to light gray, medium-crystalline, densely populated spots, **spotted anorthosite**
1408,89	1409,62	0,72	Gray to light gray, medium-crystalline, densely populated spots, fractured, **spotted anorthosite**
Image 7			
1559,52	1559,86	0,34	Black, fine crystalline, **chromitite layer**
1559,86	1559,89	0,03	Green, fine-crystalline, **pyroxenite**

1559,89	1559,92	0,03	Black, fine crystalline, **chromitite layer**
1559,92	1559,95	0,03	Green, fine-crystalline, **pyroxenite**
1559,95	1560,35	0,40	Black, fine crystalline, **chromitite layer**
1560,98	1561,58	0,60	Gray to light gray, medium-crystalline, with ~ 2mm chromitite stringers, small to large mottles, **mottled anorthosite**
1561,78	1562,35	0,57	Light gray, medium-crystalline, small to large mottles, **mottled anorthosite**
1562,35	1563,68	1,33	Light-gray, greenish in some part, medium-crystalline, small to large mottles, **mottled anorthosite**
1563,68	1564,09	0,41	Gray to light-gray, medium-crystalline, small to large mottles, **mottled anorthosite.**
1564,17	1564,72	0,55	Gray to light-gray, medium-crystalline, small to large mottles, **mottled anorthosite.**

Appendix B: The calibration reflectance panel from MicaSense.

Appendix C

Table C1: Major element results from XRF. Results reported in wt. %.

Major oxides (wt.%)	SiO_2	TiO_2	Al_2O_3	Fe_2O_3	MgO	MnO	CaO	Na_2O	K_2O	P_2O_5	LOI	Cr2O3	Total
BH29NM-01	50,99	0,18	23,40	3,93	3,66	0,11	12,97	1,78	0,47	0,04	2,15	-	99,68
BH29NM-02	48,14	0,13	28,50	3,90	3,49	0,07	11,31	1,84	0,43	0,03	2,15	-	99,99
BH29NM-03	49,85	0,14	27,13	2,66	1,58	0,06	13,71	2,15	0,49	0,04	2,43	-	100,24
BH29NM-04	50,70	0,20	5,60	11,68	23,54	0,20	3,85	1,75	0,15	0,05	2,10	-	99,82
BH29NM-05	45,85	0,05	23,95	1,93	1,24	0,09	21,45	0,30	0,18	0,01	4,40	-	99,45
BH29NM-06	52,11	0,24	16,58	6,89	9,24	0,13	11,87	1,28	0,38	0,03	0,82	-	99,58
BH29NM-07	51,94	0,22	14,59	7,11	10,15	0,15	13,79	0,95	0,25	0,02	0,77	-	99,95
BH29NM-08	51,80	0,20	16,81	7,36	10,84	0,14	11,63	1,39	0,27	0,02	0,01	-	100,47
BH29NM-09	51,61	0,15	22,81	4,17	5,31	0,08	12,03	1,86	0,40	0,02	0,04	-	98,47
BH29NM-10	52,96	0,20	15,45	7,58	11,14	0,15	10,36	1,29	0,41	0,03	0,00	-	99,57
BH29NM-11	52,76	0,23	11,37	10,08	14,51	0,19	9,13	0,94	0,31	0,02	0,03	-	99,57
BH29NM-12	51,90	0,18	22,75	4,18	5,35	0,14	11,97	1,51	0,40	0,02	0,05	-	98,46
BH29NM-13	47,50	0,05	29,31	1,98	1,67	0,05	14,13	1,23	0,33	0,01	1,98	-	98,24
BH29NM-14	51,71	0,23	16,61	6,84	9,17	0,13	11,77	1,71	0,38	0,03	2,29	-	100,86
BH29NM-15	48,88	0,07	29,36	1,99	2,36	0,03	13,92	1,69	0,18	0,01	1,52	-	100,00
BH29NM-16	51,71	0,22	5,07	11,88	24,09	0,21	3,77	0,22	0,16	0,05	0,93	-	98,30
BH29NM-17	52,20	0,20	4,70	11,37	23,42	0,20	4,00	0,25	0,29	0,04	1,69	-	98,37
BH29NM-18	46,41	0,19	9,78	10,35	24,08	0,16	5,03	0,40	0,11	0,01	1,52	-	98,03
BH29NM-19	11,82	0,85	7,21	30,65	8,44	0,21	1,33	0,05	0,04	0,00	-	38,61	99,21
BH29NM-20	44,74	0,25	15,99	12,27	23,38	0,22	3,71	0,33	0,07	0,01	-0,04	-	100,93
BH29NM-21	50,49	0,07	27,57	2,49	1,67	0,07	14,62	0,90	0,36	0,01	0,03	-	98,27
BH29NM-22	52,71	0,15	7,50	11,17	23,18	0,20	4,81	0,60	0,06	0,01	-0,14	-	100,26
BH29NM-23	53,11	0,19	3,33	12,57	26,30	0,23	3,13	0,38	0,05	0,02	0,10	-	99,39
BH29NM-24	67,81	0,69	12,54	3,97	4,28	0,06	2,17	0,61	5,06	0,11	1,63	-	98,93
BH29NM-25	9,34	0,79	12,94	28,38	7,23	0,21	1,64	0,34	0,08	0,01	-	38,97	99,93
Min	9,34	0,05	3,33	1,93	1,24	0,03	1,33	0,05	0,04	0,00	-0,14	38,61	
Max	67,81	0,85	29,36	30,65	26,30	0,23	21,45	2,15	5,06	0,11	4,40	38,97	

Table C2: Trace element results from XRF. Results reported in ppm.

Trace elements (ppm)	V	Cr	Co	Ni	Cu	Zn	Ba	Rb	Sr	Y	Zr	Nb	Pb	Th	U	Sc
BH29NM-01	61	49	14	83	13	48	133	15	278	6	38	2	4	5	<3	13
BH29NM-02	61	34	15	68	19	44	130	12	310	6	31	2	4	<3	<3	16
BH29NM-03	49	33	2	31	8	42	120	17	309	6	38	2	15	<3	<3	11
BH29NM-04	41	41	3	46	9	34	88	9	298	2	17	2	8	<3	<3	15
BH29NM-05	38	160	<2	42	8	37	30	6	73	2	18	<1	8	4	<3	9
BH29NM-06	131	149	36	192	27	65	104	11	205	8	40	2	15	<3	2	26
BH29NM-07	160	230	36	212	20	67	76	9	173	9	36	1	6	<3	<3	33
BH29NM-08	147	440	37	219	21	66	103	9	199	8	33	2	8	3	3	26
BH29NM-09	76	172	16	102	13	44	120	9	286	5	32	2	4	4	<3	12
BH29NM-10	139	380	44	225	22	99	111	15	190	7	36	1	4	<3	<3	23
BH29NM-11	174	522	66	292	56	74	84	14	140	7	38	3	11	<3	3	29
BH29NM-12	151	471	33	216	21	81	73	6	210	8	27	2	13	<3	<3	28
BH29NM-13	48	109	3	35	7	56	64	7	350	3	13	2	2	<3	<3	14
BH29NM-14	58	137	2	41	6	65	95	29	366	2	15	2	2	<3	<3	12
BH29NM-15	49	118	3	55	18	47	77	3	365	2	14	1	<3	3	<3	13
BH29NM-16	166	4158	107	579	34	90	79	7	59	6	35	2	10	<3	<3	27
BH29NM-17	144	2386	101	542	24	88	76	14	56	5	43	2	13	<3	<3	28
BH29NM-18	233	14360	83	614	36	79	74	5	128	3	32	1	12	<3	<3	24
BH29NM-19	1674	386100	102	992	8	611	20	1	<1	<1	23	<1	68	<3	<3	12
BH29NM-20	294	19438	100	541	17	143	62	3	54	4	28	1	21	<3	<3	25
BH29NM-21	100	1321	54	365	<2	68	43	2	221	1	20	1	17	<3	<3	19
BH29NM-22	162	1900	103	500	24	109	43	1	102	3	18	<1	18	<3	<3	27
BH29NM-23	186	2190	124	595	36	103	59	3	38	4	23	1	13	<3	<3	30
BH29NM-24	77	296	19	86	65	64	1242	136	170	18	283	16	31	14	4	7
BH29NM-25	2061	389700	111	1132	670	615	22	2	30	<1	25	1	68	<3	<3	9
NIM-N	218	30	53	116	15	66	100	4	258	6	21	2	9	<3	<3	39
Certified values	220	32	58	120	14	68	101	6	260	7	23	2	7	<3	<3	38

Appendix D: Scanning Electron Microscopy: Elemental Composition from sample BH29-NM-04 (a), BH29-NM-11 (b), and BH29-NM-15(c).

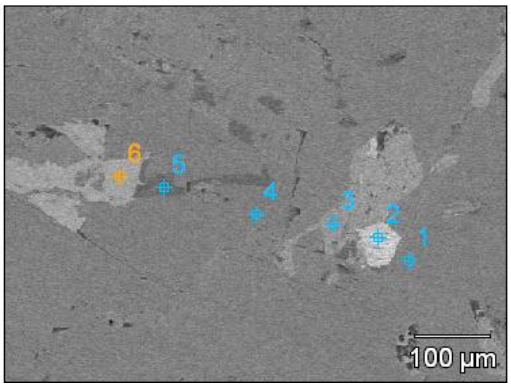

(a)

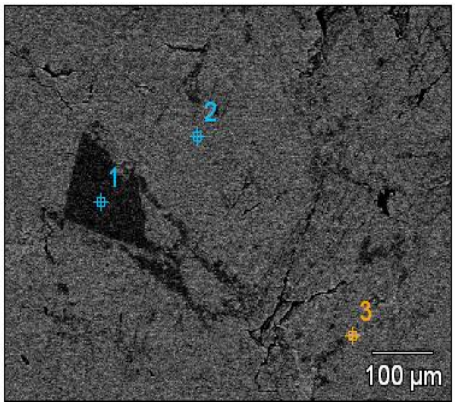

(b)

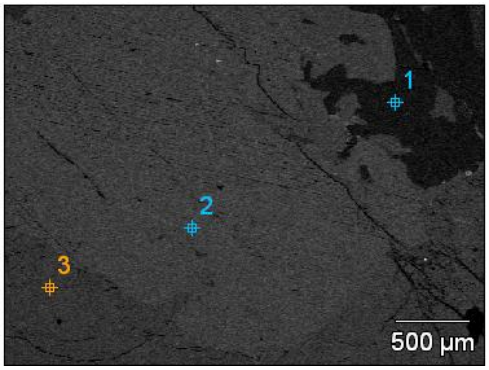

(c)

Points	Na_2O	MgO	Al_2O_3	SiO_2	CaO	TiO_2	Fe_2O_3	Mineral	Idealised Chemical Formula
(a) 1	4.33		28.45	50.71	16.51			Plagioclase	$(Ca,Na)(Si,Al)_4O_8$
2		2.59	3.18	19.96	17.53	56.73		Titanite	$CaTiSiO_5$
3		12.98	2.62	54.43	15.67		14.31	Actinolite	$Ca_2(Mg; Fe^{2+})_5Si_8O_{22}(OH)_2$
4	4.09		30.01	50.08	15.82			Plagioclase	$(Ca,Na)(Si,Al)_4O_8$
5				100.00				Quartz	SiO_2
6			22.24	36.70	27.94		13.12	Epidote	$Ca_2Al_2(Fe^{3+};Al)(SiO_4)(Si_2O_7)O(OH)$
(b)	Na_2O	Al_2O_3	SiO_2	CaO	Fe_2O_3				
1			100.00					Quartz	SiO_2
2	3.19	30.07	48.19	18.56				Plagioclase	$CaAl_2Si_2O_8$
3		27.87	37.00	29.37	5.76			Epidote	Ca2Al2(Fe^{3+};Al)(SiO4)(Si2O7)O(OH)
(c)	MgO	Al_2O_3	SiO_2	CaO	Fe_2O_3				
1			100.00					Quartz	SiO_2
2	13.70	1.87	52.13	23.96	8.34			Clinopyroxene	$(Ca;Na)(Mg;Fe; Al;Ti)(Si; Al)_2O_6$
3	24.72	1.79	54.14	2.24	17.11			Orthopyroxene	$(Mg,Fe)_2Si_2O_6$

Appendix E: Training data statistics of pixel intensity distribution in DN.

Table E1: Gabbronorite and anorthosite.

Training data			
Image 2			
Gabbronorite (1-15)	**Median**	**SD**	**Variance**
1	158,55	17,18	295,07
2	147,27	14,92	222,69
3	**147,35**	**15,36**	**235,97**
4	155,43	16,69	278,66
5	157,46	15,46	239,09
6	161,23	19,77	390,69
7	149,93	16,07	258,25
8	153,26	14,87	221,04
9	144,38	14,22	202,22
10	155,48	13,70	187,60
11	146,98	15,00	224,96
12	144,01	14,03	196,97
13	153,88	13,39	179,31
14	154,42	12,05	145,30
15	145,51	14,88	221,28
Image 3			
Anorthosite (1-20)	**Median**	**SD**	**Variance**
1	188,23	13,88	192,78
2	**206,98**	**13,91**	**193,59**
3	197,47	14,78	218,49
4	196,80	12,21	149,05
5	202,71	11,69	136,76
6	196,11	15,11	228,28
7	203,65	14,84	220,30
8	200,47	16,07	258,15
9	204,38	15,00	224,92
10	204,99	13,44	180,67
11	209,06	9,84	96,91
12	196,00	13,44	180,50
13	200,06	11,73	137,53
14	193,51	17,20	296,00
15	198,47	16,07	258,15
16	196,35	14,39	207,10
17	194,35	15,55	241,88
18	197,96	15,19	230,82
19	202,15	9,28	86,09
20	193,53	9,71	94,27

Table E2: Chromitite and pyroxenite.

Training data			
Image 4			
Chromitite (1-2)	**Median**	**SD**	**Variance**
1	**108,49**	**25,85**	**668,38**
2	81,94	12,75	162,68
Pyroxenite (1-10)			
1	156,98	14,38	206,92
2	150,07	14,60	213,19
3	160,16	20,91	437,25
4	152,58	17,16	294,52
5	162,94	17,93	321,33
6	164,87	12,76	162,88
7	173,12	19,78	391,36
8	**158,21**	**16,88**	**284,87**
9	172,47	15,56	242,13
10	172,71	13,68	187,26

Appendix F: Validating data statistics of pixel intensity distribution in DN.

Table F1: Gabbronorite

Validating data			
Image 5			
Gabbronorite (16-41))	**Median**	**SD**	**Variance**
16	182,41	40,77	1662,43
17	169,85	49,05	2406,22
18	177,78	41,60	1730,65
19	169,01	43,04	1852,34
20	160,11	55,09	3035,22
21	162,67	53,34	2845,16
22	165,89	44,58	1987,78
23	167,40	50,86	2586,68
24	165,27	51,76	2678,63
25	151,79	59,75	3570,01
26	174,03	46,33	2146,07
27	**170,31**	**49,00**	**2400,57**
28	167,41	49,65	2465,00
29	172,79	46,40	2152,67
30	176,38	45,30	2052,12
31	165,66	42,92	1842,04
32	165,65	47,35	2241,87
33	155,10	43,70	1909,49
34	160,12	52,84	2792,52
35	163,80	52,78	2785,34
36	164,57	51,92	2696,01
37	160,92	52,99	2808,31
38	163,58	51,52	2654,04
39	169,94	49,38	2438,60
40	162,51	53,18	2828,48
41	175,56	46,12	2127,25

Table F2: Chromitite and pyroxenite

Validating data			
Image 7			
Chromitite (3-13)	**Median**	**SD**	**Variance**
3	143,59	51,29	2630,82
4	131,03	42,01	1765,07
5	154,83	58,16	3382,27
6	**153,83**	**58,57**	**3430,16**
7	148,41	61,75	3813,53
8	144,26	64,12	4111,82
9	148,35	61,79	3817,78
10	146,16	62,85	3950,32
11	148,03	61,60	3794,82
12	147,19	62,25	3875,49
13	144,27	63,95	4089,99
Image 5			
Pyroxenite (11-19)	**Median**	**SD**	**Variance**
11	151,54	59,38	3526,57
12	150,06	60,35	3641,84
13	155,36	49,05	2406,14
14	157,64	54,47	2967,28
15	165,08	50,63	2563,61
16	146,29	62,43	3897,97
17	137,25	66,99	4487,33
18	147,53	60,04	3604,57
19	**153,83**	**56,90**	**3238,15**

Table F3: Anorthosite

Validating data			
Image 7			
Anorthosite (21-60)	**Median**	**SD**	**Variance**
21	199,43	25,40	645,09
22	195,87	21,51	462,59
23	196,87	23,78	565,25
24	185,90	30,79	947,88
25	204,53	28,82	830,78
26	212,28	22,87	523,10
27	198,36	24,71	610,48
28	197,29	28,82	830,67
29	190,99	32,43	1052,02
30	177,04	37,96	1440,78
31	177,28	30,74	944,69
32	176,57	34,05	1159,45
33	185,01	28,36	804,50
34	217,61	21,18	448,70
35	194,93	34,87	1215,91
36	178,96	37,60	1413,57
37	185,79	36,08	1301,77
38	**187,48**	**30,04**	**902,30**
39	199,54	22,44	503,50
40	195,40	24,68	609,15
41	187,82	39,00	1521,07
42	193,08	35,95	1292,23
43	187,45	35,10	1232,12
44	195,25	34,51	1190,83
45	182,97	41,23	1700,22
46	192,34	28,16	792,84
Image 6	**Median**	**SD**	**Variance**
47	175,69	40,90	1672,99
48	176,84	35,46	1257,54
49	177,66	35,69	1274,02
50	200,31	31,00	960,84
51	192,52	35,93	1290,75
52	184,78	40,63	1650,89
53	182,78	39,74	1578,98
54	182,78	39,74	1578,98
55	177,79	38,09	1451,18
56	178,89	41,67	1736,29
57	167,73	35,75	1278,08
58	182,64	40,40	1632,22
59	177,32	44,41	1971,96

Appendix G

Table G1: Algorithm for converting RGB image to grayscale in R Studio.

```
# Install required packages if not already installed
if (!require(terra)) install.packages("terra", dependencies = TRUE)
if (!require(imager)) install.packages("imager", dependencies = TRUE)

# Load necessary libraries
library(terra)
library(imager)

# Define the folder path containing the TIFF images
folder_path <- "D:/MSc/Processing/Sony_Images/clipped/clipped"

# List all .tif files in the folder
tif_files <- list.files(folder_path, pattern = "\\.tif$", full.names = TRUE)

# Loop through each .tif file and convert it to grayscale
for (file in tif_files) {
  # Load the image as a raster
  img <- rast(file)

  # Check if the image has 3 bands (RGB)
  if (nlyr(img) == 3) {
    # Extract Red, Green, and Blue bands
    R <- img[[1]]
    G <- img[[2]]
    B <- img[[3]]

    # Apply the Luminosity method: 0.2989*R + 0.5870*G + 0.1140*B
    gray_img <- 0.2989 * R + 0.5870 * G + 0.1140 * B

    # Define output filename
    output_file <- file.path(
      folder_path,
      paste0(tools::file_path_sans_ext(basename(file)), "_gray.tif")
    )

    # Save the grayscale image
    writeRaster(gray_img, output_file, overwrite = TRUE)

    # Print confirmation
    cat("Converted:", basename(file), "to grayscale ->", output_file, "\n")
  } else {
    cat("Skipping:", basename(file), "- Not an RGB image\n")
  }
}

cat("Batch grayscale conversion complete.\n")
```

Appendix H: Extracted endmember spectral curves

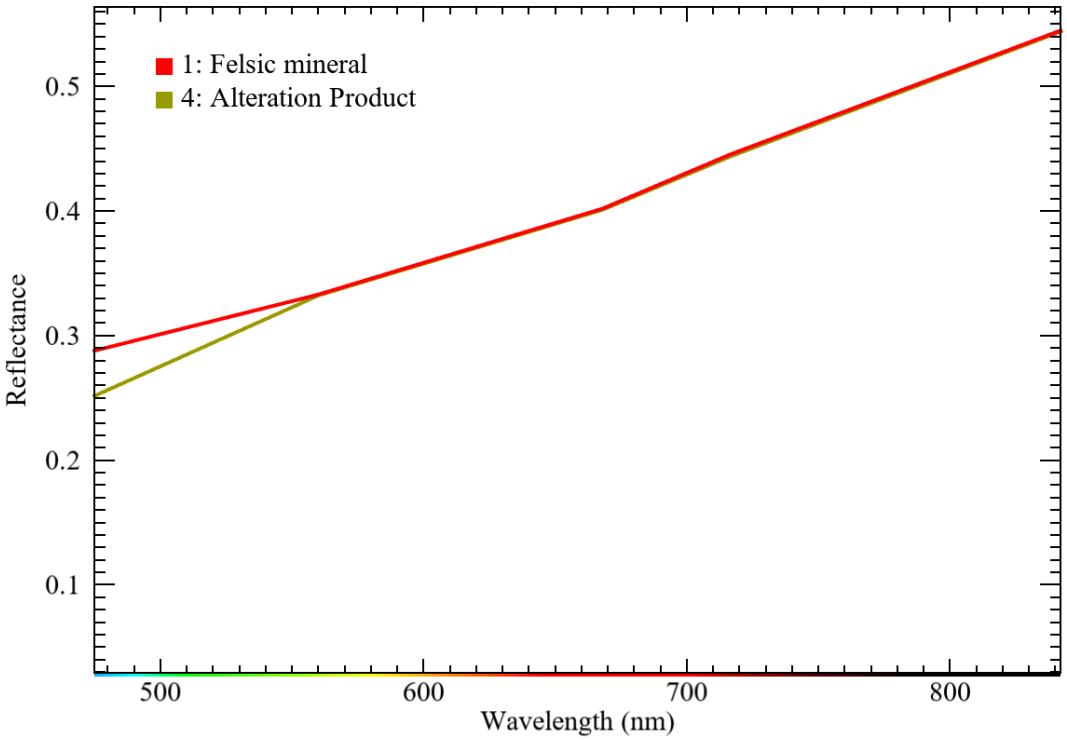

(a) Spectral curves of class 1 and 4, felsic mineral and alteration product.

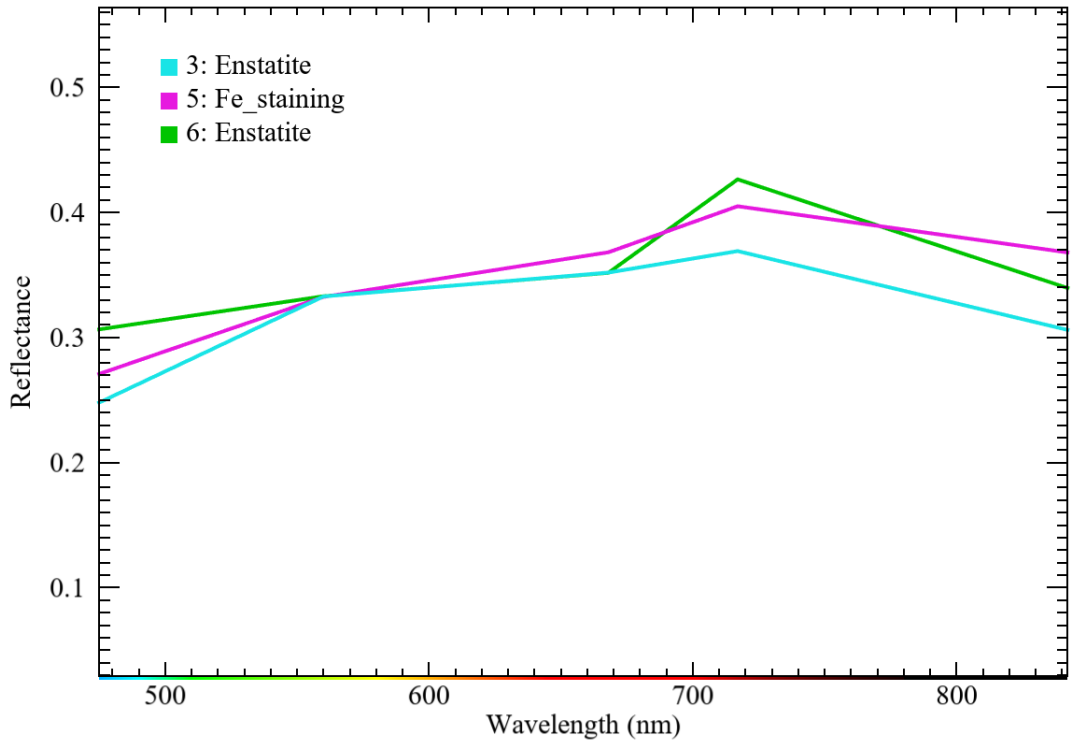

(b) Spectral curves of class 3, 5, and 6, 3 and 6 enstatite, and 5 Fe stains.

Appendix I

Table I1: Image Classification Accuracy Assessment

Classification Accuracy	**Description**
Low	Major minerals (orthopyroxene, plagioclase, and chromite) are spatially partially matched in the classification; unreliable detection of alteration; significant under- and over-classification; not comparable to petrographic observations.
Moderate	Major minerals are partially mapped with spatial mismatches; boundaries are unclear; alteration mapping is somewhat comparable to petrographic data.
High	Major minerals are well mapped with good spatial alignment; minor under- and over-classification or misclassification may occur; alteration is interpretable.
Very High	Major and alteration minerals are accurately mapped with clear spatial boundaries, minimal classification errors, and strong agreement with petrographic observations.